#### **OPEN ACCESS**



# The *R*-Process Alliance: Chemodynamically Tagged Groups. II. An Extended Sample of Halo *r*-process-enhanced Stars

Derek Shank<sup>1,2</sup>, Timothy C. Beers<sup>1,2</sup>, Vinicius M. Placco<sup>3</sup>, Dmitrii Gudin<sup>4</sup>, Thomas Catapano<sup>1</sup>, Erika M. Holmbeck<sup>2,5,11</sup>, Rana Ezzeddine<sup>2,6</sup>, Ian U. Roederer<sup>2,7</sup>, Charli M. Sakari<sup>8</sup>, Anna Frebel<sup>2,9</sup>, and Terese T. Hansen<sup>10</sup>.

1 Department of Physics and Astronomy, University of Notre Dame, Notre Dame, IN 46556, USA; dshankl@nd.edu

2 Joint Institute for Nuclear Astrophysics—Center for the Evolution of the Elements (JINA-CEE), East Lansing, MI, USA

3 NSF's NOIRLab, 950 N. Cherry Avenue, Tucson, AZ 85719, USA

4 Department of Mathematics, University of Maryland, College Park, MD 20742, USA

5 Observatories of the Carnegie Institution for Science, 813 Santa Barbara Street, Pasadena, CA 91101, USA

6 Department of Astronomy, University of Florida, Bryant Space Science Center, Gainesville, FL 32611, USA

7 Department of Astronomy, University of Michigan, 1085 S. University Avenue, Ann Arbor, MI 48109, USA

8 Department of Physics and Astronomy, San Francisco State University, San Francisco, CA 94132, USA

9 Department of Physics and Kavli Institute for Astrophysics and Space Research, Massachusetts Institute of Technology, Cambridge, MA 02139, USA

10 Department of Astronomy, Stockholm University, Albanova University Centre, SE-106 91 Stockholm, Sweden

#### **Abstract**

Received 2022 August 20; revised 2022 October 6; accepted 2022 October 17; published 2023 January 20

Orbital characteristics based on Gaia Early Data Release 3 astrometric parameters are analyzed for  $\sim 1700~r$ -process-enhanced (RPE; [Eu/Fe] > +0.3) metal-poor stars ([Fe/H]  $\leq -0.8$ ) compiled from the R-Process Alliance, the GALactic Archaeology with HERMES (GALAH) DR3 survey, and additional literature sources. We find dynamical clusters of these stars based on their orbital energies and cylindrical actions using the HDBSCAN unsupervised learning algorithm. We identify 36 chemodynamically tagged groups (CDTGs) containing between five and 22 members; 17 CDTGs have at least 10 member stars. Previously known Milky Way (MW) substructures such as Gaia-Sausage-Enceladus, the splashed disk, the metal-weak thick disk, the Helmi stream, LMS-1 (Wukong), and Thamnos are reidentified. Associations with MW globular clusters are determined for seven CDTGs; no recognized MW dwarf galaxy satellites were associated with any of our CDTGs. Previously identified dynamical groups are also associated with our CDTGs, adding structural determination information and possible new identifications. Carbon-enhanced metal-poor RPE (CEMP-r) stars are identified among the targets; we assign these to morphological groups in a Yoon-Beers  $A(C)_c$  versus [Fe/H] diagram. Our results confirm previous dynamical analyses that showed RPE stars in CDTGs share common chemical histories, influenced by their birth environments.

*Unified Astronomy Thesaurus concepts:* Milky Way dynamics (1051); Galaxy dynamics (591); Galactic archaeology (2178); Milky Way evolution (1052); Milky Way formation (1053); Milky Way stellar halo (1060); R-process (1324)

Supporting material: machine-readable tables

# 1. Introduction

The rapid neutron-capture process (r-process) governs the formation of the heaviest elements in the universe, and accounts for the production of roughly half of the elements beyond iron. A large source of neutrons is required in order to allow neutron-rich isotopes to form far from stability, where they subsequently decay to stable, or long-lived, isotopes all the way up to uranium (U; Z=92). The r-process was first formalized by the revolutionary work of Burbidge et al. (1957) and Cameron (1957), and later Truran and colleagues (e.g., Truran & Cameron 1971; for historical reviews; see Truran et al. 2002 and Cowan et al. 2021), who suggested that corecollapse supernovae were the source of r-process elements. Candidate sites that produce a sufficient neutron fluence to

Original content from this work may be used under the terms of the Creative Commons Attribution 4.0 licence. Any further distribution of this work must maintain attribution to the author(s) and the title of the work, journal citation and DOI.

result in an *r*-process are limited, and have been speculated to be either magnetorotationally jet-driven supernovae (see Mosta et al. 2018 for a debate on this source), or mergers of either binary neutron stars or a binary neutron star and black hole system, in addition to the already suggested core-collapse supernovae (Lattimer & Schramm 1974; Woosley et al. 1994; Winteler et al. 2012; Wanajo et al. 2014; Nishimura et al. 2015; Thielemann et al. 2017). Observations of the kilonova associated with the gravitational wave event GW170817 have shown a definitive astrophysical source of heavy elements created by the *r*-process in binary neutron star mergers (Abbott et al. 2017a, 2017b; Drout et al. 2017; Shappee et al. 2017; Tanaka et al. 2017; Watson et al. 2019).

The nature of the *r*-process can also be studied through efforts to classify halo stars into chemical groups (see Table 1 for definitions), furthering the statistics of *r*-process abundance patterns. Large-scale efforts to identify *r*-process-enhanced (RPE) stars have been underway since these stars were first recognized by Sneden et al. (1994) (see, e.g., Christlieb et al. 2004; Barklem et al. 2005; Roederer et al. 2014). With the rarity of these stars limiting the total number of known

<sup>11</sup> Hubble Fellow.

Table 1
Signatures of Metal-poor Stars

Signature	Definition	Abbreviation	Source
Main r-process	$+0.3 < [Eu/Fe] \le +0.7, [Ba/Eu] < 0.0$	r-I	Holmbeck et al. (2020)
Main r-process	$+0.7 < [Eu/Fe] \le +2.0, [Ba/Eu] < 0.0$	r-II	Holmbeck et al. (2020)
Main r-process	[Eu/Fe] > +2.0, [Ba/Eu] < -0.5	r-III	Cain et al. (2020)
Carbon enhanced	[C/Fe] > +0.7	CEMP	Aoki et al. (2007)
CEMP and RPE	[C/Fe] > +0.7, [Eu/Fe] > +0.3, [Ba/Eu] < 0.0	CEMP-r	Aoki et al. (2007)

moderately *r*-process-enhanced (*r*-I) and highly *r*-process-enhanced (*r*-II stars), the *R*-Process Alliance (RPA) was initiated in 2017 with the goal of dramatically increasing the total number of identified RPE stars. Through dedicated spectroscopic analysis efforts (Hansen et al. 2018; Sakari et al. 2018; Ezzeddine et al. 2020; Holmbeck et al. 2020), the RPA has already doubled the number of known *r*-II stars (from 65 to 137) across the first four data releases (Holmbeck et al. 2020). Additional RPE stars are expected to be identified in the near future, based on ongoing analysis of over a thousand moderately high-resolution, moderate signal-to-noise ratio (S/N) *snapshot* spectra obtained by the RPA over the past few years.

The advent of the Gaia satellite mission (Gaia Collaboration et al. 2016) has allowed for precision astrometric parameters (including parallaxes and proper motions) to be collected for over a billion stars, with millions having measured radial velocities (only available for bright sources with  $V \lesssim 14$ ) in Gaia Early Data Release 3 (EDR3; Gaia Collaboration et al. 2021). Since *r*-process elements require high-resolution spectra to measure their abundances, accurate radial velocities are often known for RPE stars from such data, even if Gaia does not have this information. These data can be used to reconstruct the orbits of stars once a suitable Galactic potential is chosen. Stars with similar energies and actions, describing the extent of the stellar orbits, can be attributed to the same progenitor satellite or globular cluster that was subsequently accreted into the Milky Way (MW), dispersing the observed RPE stars to their current positions (Helmi & White 1999).

Roederer et al. (2018) employed unsupervised clustering algorithms to group stellar orbital dynamics for RPE stars, an approach that has proven crucial to determining structures in the MW that are not revealed through large-scale statistical sampling methods. These authors were able to determine the orbits for 35 *r*-II stars. Multiple clustering tools were applied to the orbital energies and actions to identify stars with similar orbital characteristics. This study revealed eight dynamical groupings comprising between two and four stars each. The small dispersion of each group's metallicity was noted, and accounted for by reasoning that each group was associated with a unique accretion event whose stars shared a common chemical history.

Gudin et al. (2021) extended the work by Roederer et al. (2018), using a much larger sample of RPE stars, including both *r*-I and *r*-II stars. Utilizing the HDBSCAN algorithm (Campello et al. 2013), 30 chemodynamically tagged groups (CDTGs)<sup>12</sup> were discovered. Their analysis revealed statistically significant similarities in stellar metallicity, carbon abundance, and *r*-process-element ([Sr/Fe], <sup>13</sup> [Ba/Fe], and [Eu/Fe]) abundances

within individual CDTGs, strongly suggesting that these stars experienced similar chemical-evolution histories in their progenitor galaxies.

This work aims to expand on the efforts of Roederer et al. (2018) and Gudin et al. (2021), analyzing the CDTGs present among stars in an updated RPE stellar sample, which includes stars from the literature and the published GALactic Archaeology with HERMES Data Release 3 (GALAH DR3; Buder et al. 2021) catalog of metal-poor ([Fe/H]  $\leq -0.8$ ) stars. The procedures employed closely follow the work of Shank et al. (2022b), which considered DTGs found in the sample of the best and brightest selection of Schlaufman & Casey (2014) (see Placco et al. 2019 and Limberg et al. 2021a for follow-up studies). The association of our identified CDTGs with recognized Galactic substructures, previously known DTGs/ CDTGs, globular clusters, and dwarf galaxies is explored, with the most interesting stellar populations being noted for future high-resolution follow-up studies. Statistical analysis of the elemental abundances present in the CDTGs is investigated.

This paper is outlined as follows. Section 2 describes the RPE literature and GALAH sample, along with their associated astrometric parameters and the dynamical parameters. The clustering procedure is outlined in Section 3. Section 4 explores the clusters and their association with known MW structures. A statistical analysis of the CDTG abundances is presented in Section 5. Finally, Section 6 presents a short summary and perspectives on future directions.

# 2. Data

# 2.1. Construction of the RPE Initial Sample

A literature compilation of RPE stars and known RPE stars in GALAH DR3 form the basis for our data set, as described below.

#### 2.1.1. The RPE Literature Sample

A literature search for RPE stars, including the published material from the RPA, is constructed from the most recent version of JINAbase <sup>14</sup> (Abohalima & Frebel 2018). This version crucially includes both the abundances relative to the Sun, as well as the absolute abundances. Unlike the work presented in Gudin et al. (2021), the literature sample is chosen based on the absolute abundances, and scaled to the solar atmospheric abundances presented in Asplund et al. (2009). A restriction on the stellar parameters is applied with [Fe/H]  $\leq$  -0.8 and  $4250 \leq T_{\rm eff}({\rm K}) \leq 7000$  being the target range for RPE stars. The RPE sources are all spectroscopic surveys, and while there is not a uniform methodology in common between the analyses for determining stellar parameters, the methodologies do not differ much in their results (see Figure 5

 $<sup>\</sup>overline{^{12}}$  The distinction between CDTGS and DTGs is that the original stellar candidates of CDTGs are selected to be chemically peculiar in some fashion, while DTGs are selected from stars without detailed knowledge of their chemistry, other than [Fe/H].

<sup>&</sup>lt;sup>13</sup> The standard definition for an abundance ratio of an element in a star  $(\star)$  compared to the Sun  $(\odot)$  is given by  $[A/B] = (\log N_A/N_B)_{\star} - (\log N_A/N_B)_{\odot}$ , where  $N_A$  and  $N_B$  are the number densities of atoms for elements A and B.

<sup>14</sup> https://jinabase.pythonanywhere.com/

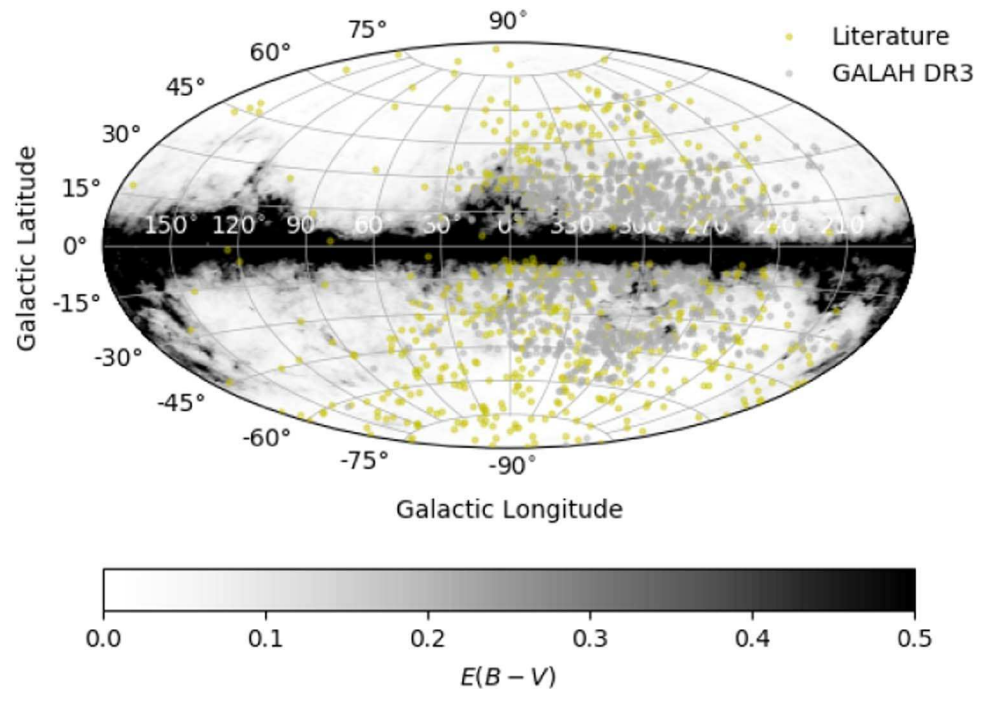


Figure 1. Galactic positions of the RPE initial sample of stars, with the literature subset shown as yellow points and the GALAH DR3 subset as gray points. The Galactic reddening map, taken from Schlegel et al. (1998), and recalibrated by Schlafly & Finkbeiner (2011), is shown in the background on a grayscale with darker regions corresponding to larger reddening.

of Sakari et al. 2018). There are a total of 582 RPE stars from the literature with  $[Fe/H] \leq -0.8$  and  $4250 \leq T_{eff}(K) \leq 7000$ that satisfy the requirements for classification as r-I (426 stars), r-II (155 stars), or r-III (one star) (McWilliam et al. 1995a, 1995b; Ryan et al. 1996; Burris et al. 2000; Fulbright 2000; Johnson 2002; Cohen et al. 2004; Honda et al. 2004; Aoki et al. 2005; Barklem et al. 2005; Ivans et al. 2006; Preston et al. 2006; François et al. 2007; Lai et al. 2008; Hayek et al. 2009; Behara et al. 2010; For & Sneden 2010; Roederer et al. 2010; Hollek et al. 2011; Hansen et al. 2012; Masseron et al. 2012; Roederer & Lawler 2012; Roederer et al. 2012; Aoki et al. 2013; Ishigaki et al. 2013; Placco et al. 2014a; Casey et al. 2014; Roederer et al. 2014; Siqueira Mello et al. 2014; Hansen et al. 2015; Howes et al. 2015; Jacobson et al. 2015; Howes et al. 2016; Aoki et al. 2017; Hill et al. 2017; Placco et al. 2017; Cain et al. 2018; Hansen et al. 2018; Hawkins & Wyse 2018; Holmbeck et al. 2018; Sakari et al. 2018; Mardini et al. 2019; Sakari et al. 2019; Valentini et al. 2019; Xing et al. 2019; Bandyopadhyay et al. 2020; Cain et al. 2020; Ezzeddine et al. 2020; Hanke et al. 2020; Holmbeck et al. 2020; Mardini et al. 2020; Placco et al. 2020; Rasmussen et al. 2020; Yong et al. 2021a, 2021b; Naidu et al. 2022; Roederer et al. 2022; Zepeda et al. 2022). Limited-r stars are not discussed in this work and are left to future studies.

#### 2.1.2. The GALAH DR3 Sample

The remainder of our sample is taken from GALAH DR3. The abundances in GALAH DR3 are subject to known quality checks, which are crucial to take into consideration; we only kept stars where there were no concerns regarding their abundance determinations satisfying flag\_X\_fe=0 and snr\_c3\_iraf >30 (Buder et al. 2021). We have employed the same procedure as the literature sample to put the GALAH DR3 stars on the same solar scale as presented in Asplund et al. (2009). We restrict stellar

values to [Fe/H]  $\leqslant -0.8$  and 4250  $\leqslant$   $T_{\rm eff}({\rm K})$   $\leqslant$  7000, the same as the RPE literature subset. We perform this stellar parameter cut to stay consistent with the RPE literature sample, and dynamical studies require a metallicity cut to allow MW substructure formed from accreted dwarf galaxies to be more easily detected (Yuan et al. 2020b). The sample was then cleaned for stars that already were in the RPE initial sample literature subset, though this was only a handful of stars. While the GALAH DR3 sample has spectroscopically derived stellar parameters, there is insufficient overlap between the stars in the RPE literature sample and the GALAH DR3 sample to comment on the validity for RPE stars. However, Figure 6 of Buder et al. (2021) shows that the stellar parameters obtained by GALAH DR3 do not differ much from Gaia FGK benchmark stars. The stellar parameter cut yields 1194 metal-poor stars from GALAH DR3 that satisfy the requirements for classification as r-I (967 stars), r-II (226 stars), or r-III (one star).

We henceforth refer to the union of the two above samples as the RPE initial sample and list them in Table 12 in the Appendix. In the print edition, only the table description is provided; the full table is available only in electronic form.

The stars from the RPE initial sample were then crossmatched with Gaia Early Data Release 3 (EDR3; Gaia Collaboration et al. 2021), using the same methods outlined in Shank et al. (2022b). Figure 1 shows the spatial distribution of these subsets of RPE stars in Galactic coordinates. A comparison of the magnitudes and colors for the RPE literature and GALAH DR3 subsets can be seen in Figure 2. From inspection of the figure, it is clear the GALAH DR3 subset of the RPE initial sample peaks at fainter magnitudes and redder colors compared to the literature RPE literature subset. RPE stars from the literature are relatively bright, due to the need for high-resolution spectra to detect the *r*-process elements. Bright stars can be studied with smaller aperture telescopes, and require less observation time on larger aperture telescopes.

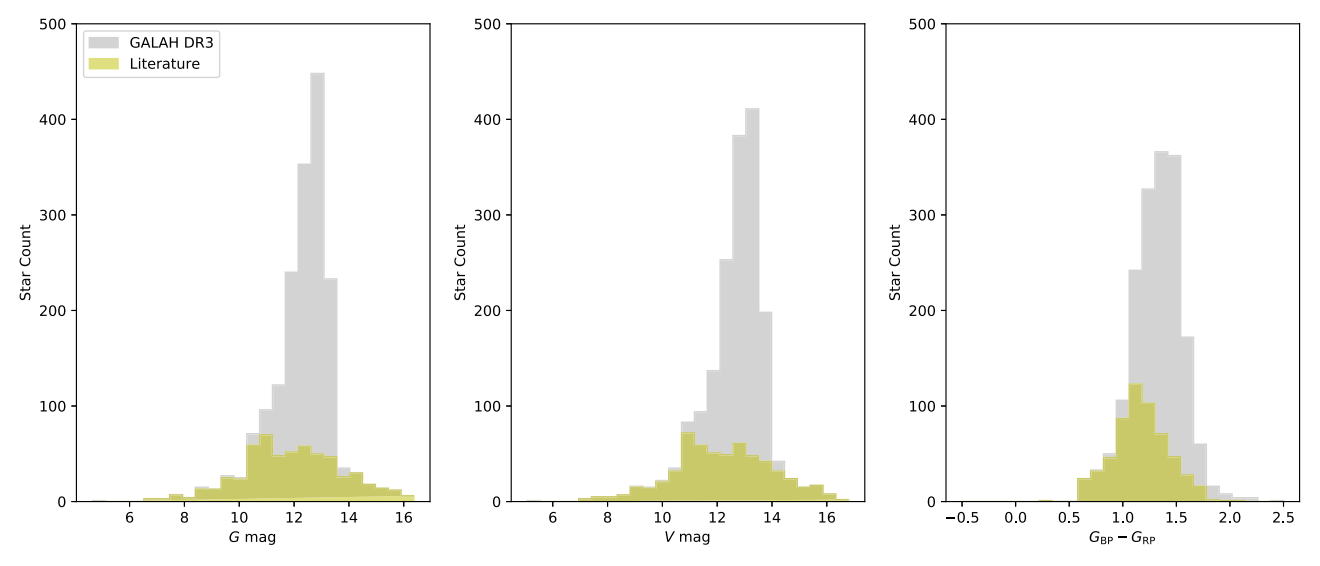


Figure 2. All panels: the literature subset of the RPE initial sample is represented as a yellow histogram; the GALAH DR3 subset is represented as a gray histogram. Left panel: histogram of the Gaia  $G_{\rm mag}$  for the RPE initial sample. Middle panel: histogram of the V<sub>mag</sub> for the RPE initial sample. Right panel: histogram of the Gaia  $G_{\rm BP}-G_{\rm RP}$  color for the RPE initial sample.

GALAH DR3 (all spectra obtained with the AAT 3.9 m telescope) includes spectra taken for somewhat fainter stars.

The available elemental-abundance ratio estimates for stars in the RPE initial sample are plotted in Figure 3, as a function of [Fe/H]. The RPE stars in GALAH DR3 do not offer much in terms of both Mg and Sr, and are included here for the sake of completeness. In the case of Sr, which is a first-peak r-process element, Y can be used as a first-peak substitute with more elemental abundances readily available from GALAH DR3; there is no comparable element for Mg. While results using these elements are postulated, future studies will allow further revisions, where necessary, as the information on abundances is updated and expanded. Figure 4 provides histograms of the elemental-abundance ratios considered in the present work. As can be seen from an inspection of these figures, stars in the RPE initial sample cover a wide range of abundances. This allows the abundance space to be accurately subsampled in the later stages of our analysis. A Yoon–Beers diagram of  $A(C)_c$ versus [Fe/H] for these stars is shown in Figure 5;  $A(C)_c$  is the absolute carbon abundance<sup>15</sup> corrected from the observed value to account for the depletion of carbon on the giant branch, following Placco et al. (2014b). For the convenience of later research, the CEMP-r stars are also provided in Table 14 of the Appendix. These stars are included in the analysis, with 28 GALAH DR3 and 82 Literature CEMP-r stars. CEMP-r stars are expected to be enriched in their birth clouds by external sources, and as such, do not conflict with the carbon-normal stars that dominate the RPE initial sample (Hansen et al. 2015). The RPE initial sample has 1393 r-I stars, 381 r-II stars, and two r-III stars, for a total of 1776 RPE stars.

#### 2.2. Construction of the Final Sample

### 2.2.1. Radial Velocities, Distances, and Proper Motions

Radial velocities, parallaxes, and proper motions for each star are taken from Gaia EDR3, when available. Radial velocities are available for about 90% of the RPE initial sample from Gaia

EDR3, with typical errors of  $\sim 1~\rm km~s^{-1}$ . The top panel of Figure 6 shows a histogram of the residual differences between the high-resolution radial velocities from the RPE initial sample and the Gaia EDR3 values. The biweight location and scale of these differences are  $\mu = -0.4~\rm km~s^{-1}$  and  $\sigma = 1.5~\rm km~s^{-1}$ , respectively. The bottom panel of this figure shows the residuals between the high-resolution sources and Gaia EDR3 radial velocities, as a function of the Gaia radial velocities. The blue-dashed line denotes the biweight location, while the shaded regions represent the first  $(1\sigma)$  and second  $(2\sigma)$  biweight scale ranges. Gaia EDR3 radial velocities are used, when available, with literature values supplementing when not.

The distances to the stars are determined either through the StarHorse distance estimate (Anders et al. 2022) or the Bailer-Jones distance estimate (BJ21; Bailer-Jones et al. 2021). Parallax values in our RPE initial sample from EDR3 have an average error of ~0.02 mas. The BJ21 and StarHorse distances are determined by a Bayesian approach utilizing the EDR3 parallax, magnitude, and color (Bailer-Jones et al. 2021; Anders et al. 2022). The errors are presented for each star in the tables provided in the Appendix. Our adopted distances are chosen following the same procedure outlined in Shank et al. (2022a), though it is noted here that we prioritize Starhorse distances; the full procedure can be found in Table 12 in the Appendix. Note that in Figure 7 the StarHorse and BJ21 approaches produce similar distances, especially when the distance is smaller than 5 kpc. The proper motions in our RPE initial sample from Gaia EDR3 have an average error of  $\sim 17 \ \mu as \ yr^{-1}$ .

# 2.2.2. Dynamical Parameters

The orbital characteristics of the stars are determined using the Action-based GAlaxy Modeling Architecture<sup>16</sup> (AGAMA) package (Vasiliev 2019), using the same solar positions and peculiar motions described in Shank et al. (2022b), <sup>17</sup> along with the same

 $<sup>\</sup>overline{^{15}}$  The standard definition of the absolute abundance of an element X in a star  $(\star)$  compared to the Sun  $(\odot)$  is  $A(X) = [X/Fe]_{\star} + [Fe/H]_{\star} + \log \epsilon(X)_{\odot}$ .

<sup>16</sup> http://github.com/GalacticDynamics-Oxford/Agama

 $<sup>^{17}</sup>$  We adopt a solar position of (-8.249, 0.0, 0.0) kpc (GRAVITY Collaboration et al. 2020) and solar peculiar motion in (U, W) as (11.1, 7.25) km s $^{-1}$  (Schönrich et al. 2010), with Galoctocentric solar azimuthal velocity  $V=250.70~{\rm km~s}^{-1}$  determined from Reid & Brunthaler (2020).

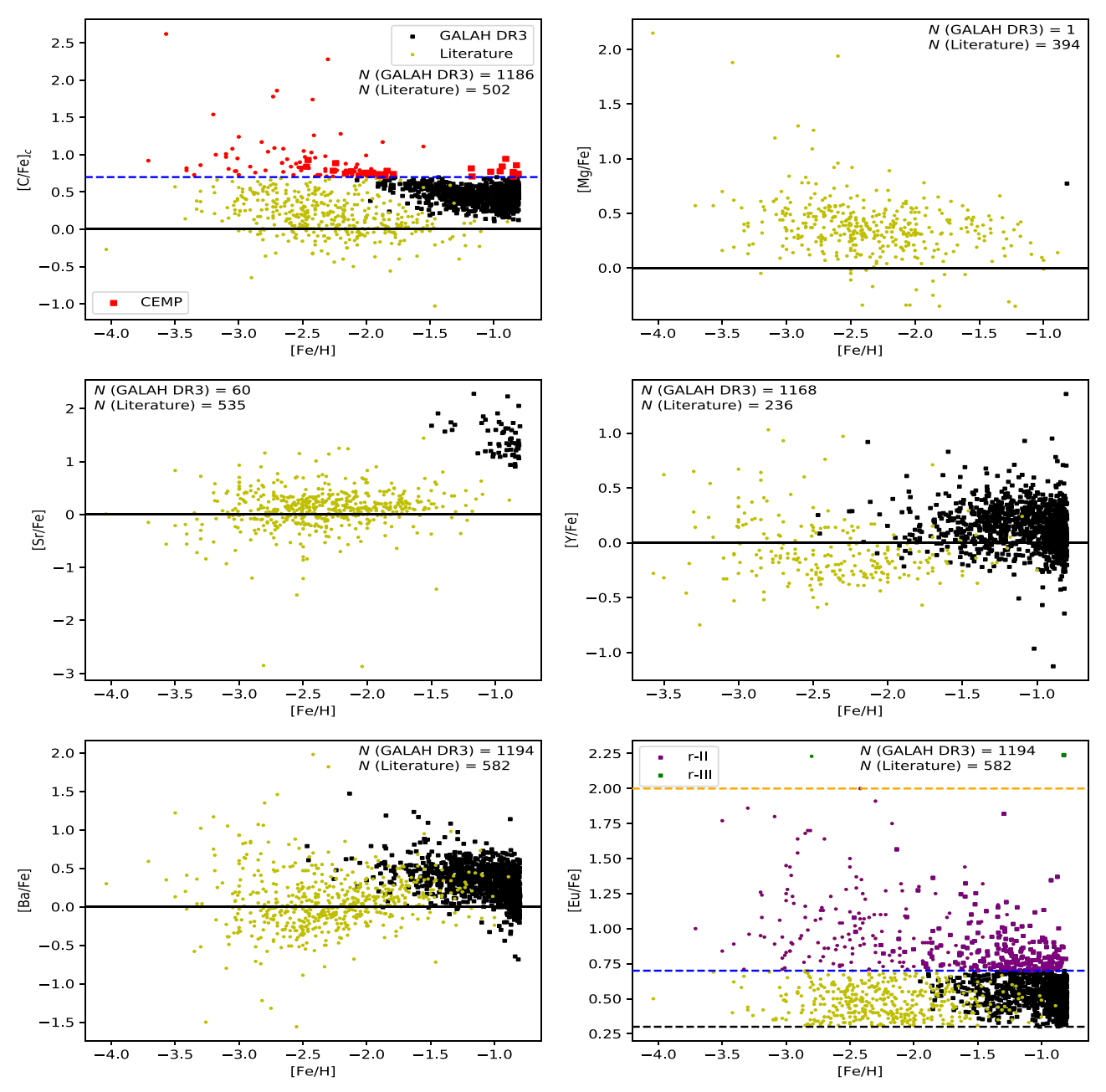


Figure 3. All panels: the literature subset of the RPE initial sample is represented as yellow points; the GALAH DR3 subset is represented as black squares. When there is a classification, such as CEMP, r-II, or r-III, the points and squares differentiate between the literature and GALAH DR3 subsets, respectively. The number of stars with detected abundances in each subset is listed in each panel. Top left panel: the corrected carbon abundance ( $[C/Fe]_c$ ) of the RPE initial sample, corrected from the observed value to account for the depletion of carbon on the giant branch following Placco et al. (2014b), as a function of metallicity ([Fe/H]). The CEMP cutoff ( $[C/Fe]_c = +0.7$ ) is noted as the blue-dashed line; CEMP-r stars are indicated with red points for the RPE initial sample. The solar value is indicated as the solid black line. Top right panel: the magnesium abundance ([Mg/Fe]) of the RPE initial sample, as a function of metallicity ([Fe/H]). The solar value is indicated with a solid black line. Middle left panel: the strontium abundance ratio ([Sr/Fe]) of the RPE initial sample, as a function of metallicity ([Fe/H]). The solar value is indicated with a solid black line. Bottom left panel: the barium abundance ratio ([Ba/Fe]) of the RPE initial sample, as a function of metallicity ([Fe/H]). The solar value is indicated with a solid black line. Bottom right panel: the europium abundance ratio ([Ba/Fe]) of the RPE initial sample, as a function of metallicity ([Fe/H]). The r-I cutoff ([Eu/Fe] = +0.3) is noted as the black-dashed line; the r-II cutoff ([Eu/Fe] = +0.7) is noted as the blue-dashed line, and the r-III stars are indicated as purple points, and r-III stars are indicated as green points.

gravitational potential, MW2017 (McMillan 2017). The 6D astrometric parameters, determined in Section 2, are run through the orbital integration process in AGAMA, in the same manner as Shank et al. (2022b), in order to calculate the orbital energy, cylindrical positions and velocities, angular momentum, cylindrical actions, and eccentricity. See Shank et al. (2022b) for definitions of these orbital parameters, and details of the Monte Carlo error calculation.

The RPE initial sample of 1776 stars was cut to exclude stars that are unbound from the MW (E>0) (J124753.30-390802.0, J135735.40-303249.0, and J175159.80-475131.0). Finally, in order to obtain accurate orbital dynamics, we conservatively remove 53 stars with radial velocity (RV) differences >15 km s<sup>-1</sup> between the Gaia EDR3 values and the high-resolution source values. Most of these stars are expected to be binaries.

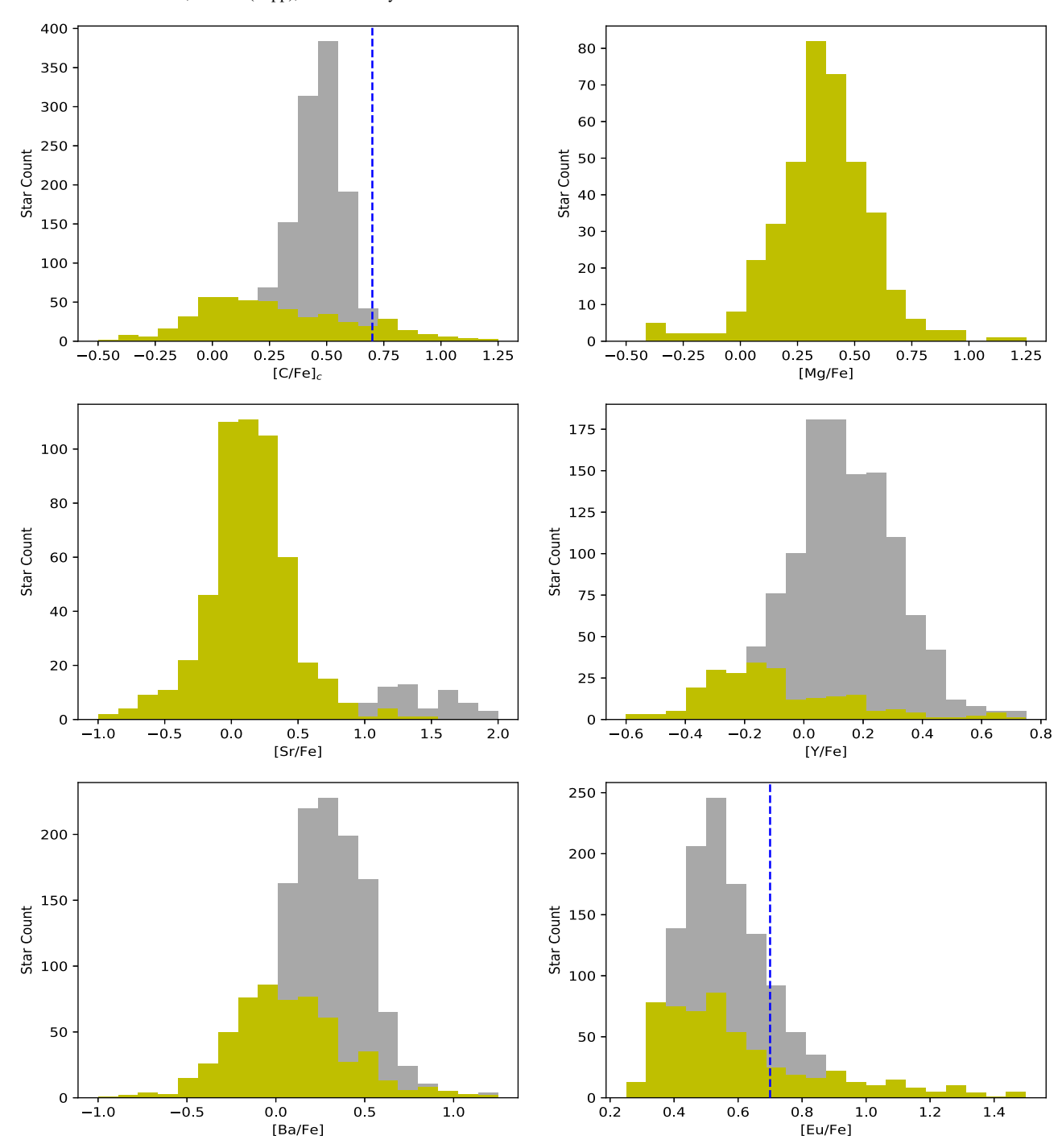
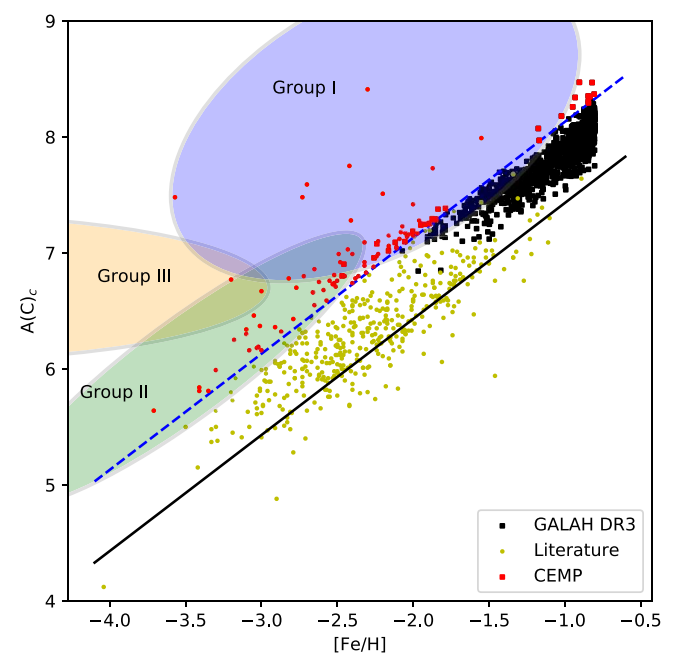


Figure 4. All panels: the literature subset of the RPE initial sample is represented as a yellow histogram; the GALAH DR3 subset is represented as a gray histogram. Note that a few stars have abundances outside the ranges shown. This is to better show the distributions, with outliers being easily identified in Figure 3. Top left panel: histogram of the corrected carbon abundance ( $[C/Fe]_c$ ) of the RPE initial sample, corrected from the observed value to account for the depletion of carbon on the giant branch following Placco et al. (2014b). The CEMP cutoff ( $[C/Fe]_c = +0.7$ ) is noted as the blue-dashed line. Top right panel: histogram of the magnesium abundance ([Mg/Fe]) of the RPE initial sample. Middle left panel: histogram of the strontium abundance ratio ([Sr/Fe]) of the RPE initial sample. Bottom left panel: histogram of the barium abundance ratio ([Ba/Fe]) of the RPE initial sample; the *r*-II cutoff ([Eu/Fe] = +0.7) is noted as the blue-dashed line.

We also considered a cut to remove stars with [Ba/Eu] < -0.3 (rather than [Ba/Eu] < 0), in order to more confidently select stars with r-process enhancement. We decided not to proceed with this cut, as ultimately including more stars with a wider range of [Ba/Eu] will only serve to increase the abundance dispersion when randomly sampled. Hence, this is a conservative choice; any stars that are included that are in fact

not clearly RPE stars (i.e., they have contributions from, e.g., the *s*-process) will only decrease the significance of our dispersion analysis described below. <sup>18</sup>

 $<sup>\</sup>overline{\ }^{18}$  An explicit test of this cut indeed resulted in a small increase in the statistical significance of both Ba and Eu (with the exception of Eu for the *r*-I sample), following the procedure described in Section 5.



**Figure 5.** Yoon–Beers diagram of  $A(C)_c$ , as a function of [Fe/H], for stars in the RPE initial sample, corrected from the observed value to account for the depletion of carbon on the giant branch following Placco et al. (2014b). The literature subset of the RPE initial sample is represented as yellow points; the GALAH DR3 subset is represented as a black squares. For the CEMP classification in red, the points and squares differentiate between literature and GALAH DR3 subsets, respectively. The CEMP cutoff ( $[C/Fe]_c = +0.7$ ) is indicated with a blue-dashed line. The CEMP-r stars for the RPE initial sample are shown as red points. [C/Fe] = 0 is indicated with a solid black line. The ellipses represent the three different morphological groups of CEMP stars (see Figure 1 in Yoon et al. (2016) for a comparison and more information).

Application of the above cuts leaves a total sample of 1720 stars to perform the following analysis. The dynamical parameters of the stars with orbits determined are listed in Table 13 in the Appendix; we refer to this as the RPE final sample. In the print edition, only the table description is provided; the full table is available only in electronic form.

Figure 8 provides histograms of  $r_{\rm apo}$  (top),  $r_{\rm peri}$  (middle), and  $Z_{\text{max}}$  (bottom) for stars in the RPE final sample. The full sample is shown in the left column, r-I stars are shown in the middle column, and r-II and r-III stars are shown in the right column. From inspection of this figure, it is clear that the majority of the stars in this sample occupy orbits that take them within the inner-halo region (up to around 15-20 kpc from the Galactic center), but they also explore regions well into the outer-halo region, up to  $\sim$ 50 kpc away from the Galactic plane. Although they appear rather similar, according to a Kolmogorov-Smirnov two-sample test between the r-I (middle column) and r-II plus r-III (right column) distributions, the hypothesis that these two samples are drawn from the same parent population is rejected ( $p \ll 0.001$ ) for each of  $r_{\rm apo}$  (top),  $r_{\rm peri}$ (middle), and  $Z_{\text{max}}$  (bottom). It may be the case that this is due to the different masses of the dwarf satellites in which the r-I and r-II stars were formed (the majority of RPE stars are likely formed in dwarf satellites, but not all are required to be), but we choose not to speculate further on this point at present.

Figure 9 shows a Toomre diagram for the RPE final sample. The red solid semicircle indicates whether a stellar orbit is disk-like (inside) or halo-like (outside). There are 234 (17% of) r-I stars and 30 (8% of) r-II stars that have disk-like kinematics. Of the disk-like r-II stars, there are 22 that are part of the GALAH

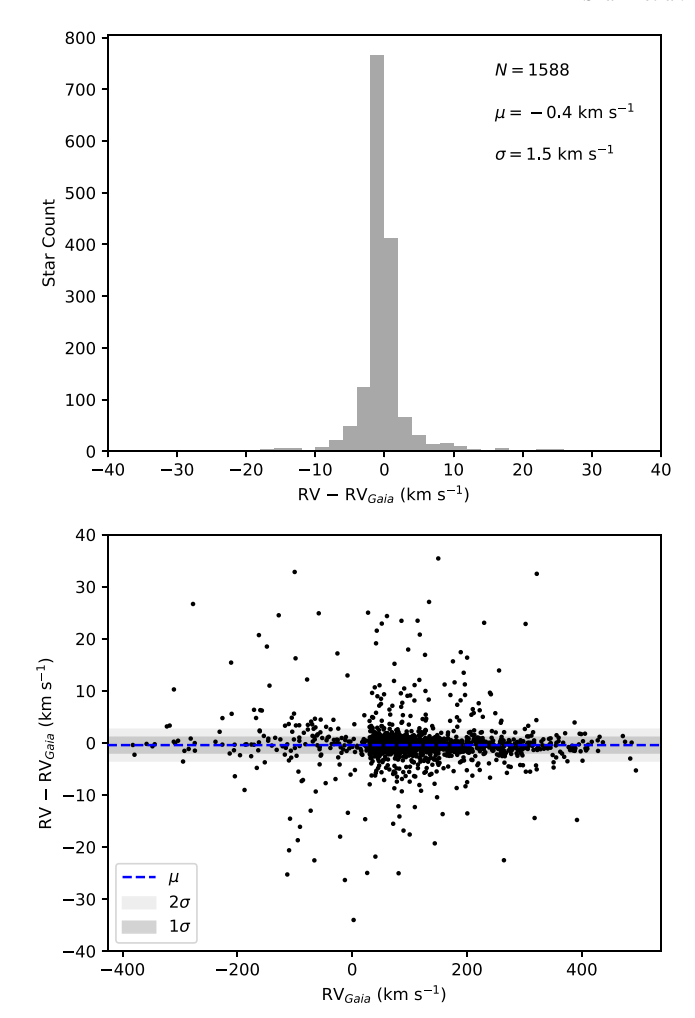


**Figure 6.** Top panel: histogram of the residuals of the difference between the source radial velocities and the Gaia EDR3 values in the RPE initial sample. The biweight location and scale are noted. Bottom panel: the residuals between the source and Gaia EDR3 radial velocities in the RPE initial sample, as a function of the Gaia radial velocities. The blue-dashed line is the biweight location of the residual difference ( $\mu = -0.4 \text{ km s}^{-1}$ ), while the shaded regions represent the first ( $1\sigma = 1.6 \text{ km s}^{-1}$ ), and second ( $2\sigma = 3.2 \text{ km s}^{-1}$ ) biweight scale ranges.

DR3 subset of the RPE final sample, while the remaining eight are from the literature subset. This difference can be attributed to RPE stars being targeted more in the halo where they have a higher likelihood of detection; most known RPE stars reside in the halo (85%). The blue vertical-dashed line indicates whether a stellar orbit is prograde ( $v_v > 0 \text{ km s}^{-1}$ ) or retrograde ( $v_v < 0$ km s<sup>-1</sup>). There are 1026 (76%) r-I stars and 215 (64% of) r-II stars with prograde orbits. The Gudin et al. (2021) literature sample found an almost 50-50 split between RPE stars that have prograde orbits compared to retrograde orbits, while the expanded RPE final sample presented here has slightly more prograde stars (1241 or 0.70%) compared to retrograde stars. Note that simulations performed by Hirai et al. (2022) show that r-II stars are slightly favored to be prograde as well. The RPE final sample has 1346 r-I stars, 372 r-II stars, and 2 r-III stars, for a total of 1720 RPE stars.

#### 3. Clustering Procedure

Helmi & de Zeeuw (2000) were among the first to suggest the use of integrals of motion, in their case orbital energies and

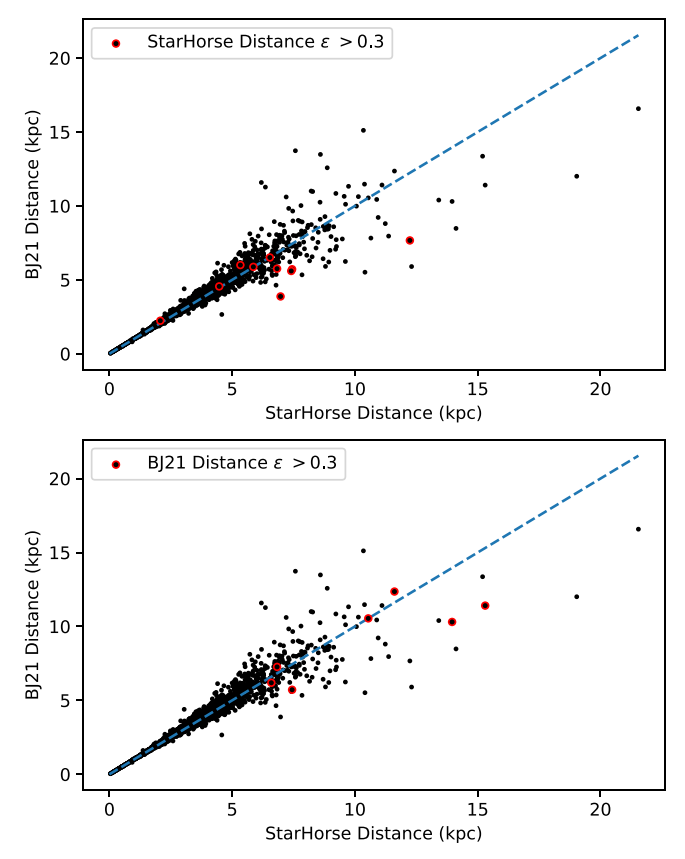


**Figure 7.** Top panel: comparison between the StarHorse distances and BJ21 distances in the RPE initial sample. Stars with red outlined points indicate that the relative distance error in StarHorse is  $\epsilon > 0.3$ . Bottom panel: the same comparison as the top panel, but with the red outlined points indicating the relative distance error in BJ21 is  $\epsilon > 0.3$ . In both plots, the dashed line indicates a one-to-one comparison between the two samples.

angular momenta, to find substructure in the MW using the precision measurements of next-generation surveys that were planned at the time. McMillan & Binney (2008) considered the use of actions as a complement to the previously suggested orbital energy and angular momenta, with only the vertical angular momentum being invariant in an axisymmetric potential. Most recently, many authors have employed the orbital energies and cylindrical actions (E,  $J_r$ ,  $J_\phi$ ,  $J_z$ ) to determine the substructure of the MW using Gaia measurements (Helmi et al. 2017; Myeong et al. 2018a, 2018b; Roederer et al. 2018; Yuan et al. 2020a, 2020b; Naidu et al. 2020; Limberg et al. 2021b; Gudin et al. 2021; Shank et al. 2022b).

As described in Shank et al. (2022b), we employ HDBSCAN in order to perform a cluster analysis over the orbital energies and cylindrical actions from the RPE sample obtained through the procedure outlined in Section 2. The HDBSCAN algorithm<sup>19</sup> operates through a series of calculations that are able to separate the background noise from denser clumps of data in the dynamical parameters. We utilize the following parameters described in Shank et al. (2022b): min\_cluster\_size = 5, min\_samples = 5, cluster\_selection\_method = "leaf", prediction\_data = True, Monte Carlo samples at 1000, and minimum confidence set to 20%.

Table 2 provides a listing of the 36 CDTGs<sup>20</sup> identified by this procedure, along with their number of member stars, confidence values (calculated as described in Shank et al. 2022b), and associations described below. Note that, although a minimum confidence value of 20% was employed, the actual minimum value found for these CDTGs is 43.0% (CDTG-15); only two other CDTGs have an assigned confidence value of less than 50.0% (CDTG-18 and CDTG-35). The average confidence level of the 36 CDTGs is quite high, at 81.9%. In total, there were 375 stars (22% of the final sample) assigned to the 36 CDTGs.

The previously known groups are identified using the nomenclature introduced by Yuan et al. (2020a). For example, IR18:E refers to the first initial and last initial of the lead author (IR) (Roederer et al. 2018), the year the paper was published (18), and after the colon is the group name provided by the authors of the paper (E). We use the following references for associations: AH17: Helmi et al. (2017), GM17: Myeong et al. (2017), HK18: Koppelman et al. (2018), GM18a: Myeong et al. (2018a), GM18b: Myeong et al. (2018b), IR18: Roederer et al. (2018), HL19: Li et al. (2019), SF19: Sestito et al. (2019), ZY19: Yuan et al. (2019), NB20: Borsato et al. (2020), HL20: Li et al. (2020), SM20: Monty et al. (2020), ZY20a: Yuan et al. (2020a), ZY20b: Yuan et al. (2020b), GC21: Cordoni et al. (2021), DG21: Gudin et al. (2021), CK21: Kielty et al. (2021), GL21: Limberg et al. (2021b), KH22: Hattori et al. (2022), KM22: Malhan et al. (2022), DS22a: Shank et al. (2022a), DS22b: Shank et al. (2022b), and SL22: Lövdal et al. (2022).

Table 3 lists the stellar members of the identified CDTGs, along with their values of [Fe/H], [C/Fe]<sub>c</sub>, [Mg/Fe], [Sr/Fe], [Y/Fe], [Ba/Fe], and [Eu/Fe], where available. The last line (in bold font) in the listing for each CDTG provides the mean and dispersion (both using biweight estimates) for each quantity. Note that for dynamical groups in which only fewer than three measurements of a given element are provided, we list the mean, and code the dispersion as a missing value.

Table 4 lists the derived dynamical parameters (and their errors) derived by AGAMA used in our analysis of the identified CDTGs.

# 4. Structure Associations

Associations between the newly identified CDTGs are now sought between known MW structures, including large-scale substructures, <sup>21</sup> previously identified dynamical groups, stellar associations, globular clusters, and dwarf galaxies.

#### 4.1. MW Substructures

Analyzing the orbital energies and actions is insufficient to determine separate large-scale substructures. Information on the elemental abundances is crucial due to the differing star formation histories of the structures, which can vary in both mass and formation redshift (Naidu et al. 2020). The outline for the prescription used to determine the structural associations with our CDTGs is described in Naidu et al. (2020), and explained in detail in Shank et al. (2022b). Simple selections

<sup>&</sup>lt;sup>19</sup> For a detailed description of the HDBSCAN algorithm visit: https://hdbscan.readthedocs.io/en/latest/how\_hdbscan\_works.html.

 $<sup>^{20}</sup>$  CDTGs are derived from purely dynamical parameters. The chemical information comes from the RPE selection criteria, thus distinguishing them from dynamically tagged groups (DTGs).

<sup>&</sup>lt;sup>21</sup> Here, the term *large-scale substructure* is used to distinguish large overdensities of stars determined in the integral of motion space in the Galaxy, e.g., the substructures presented in Naidu et al. (2020).

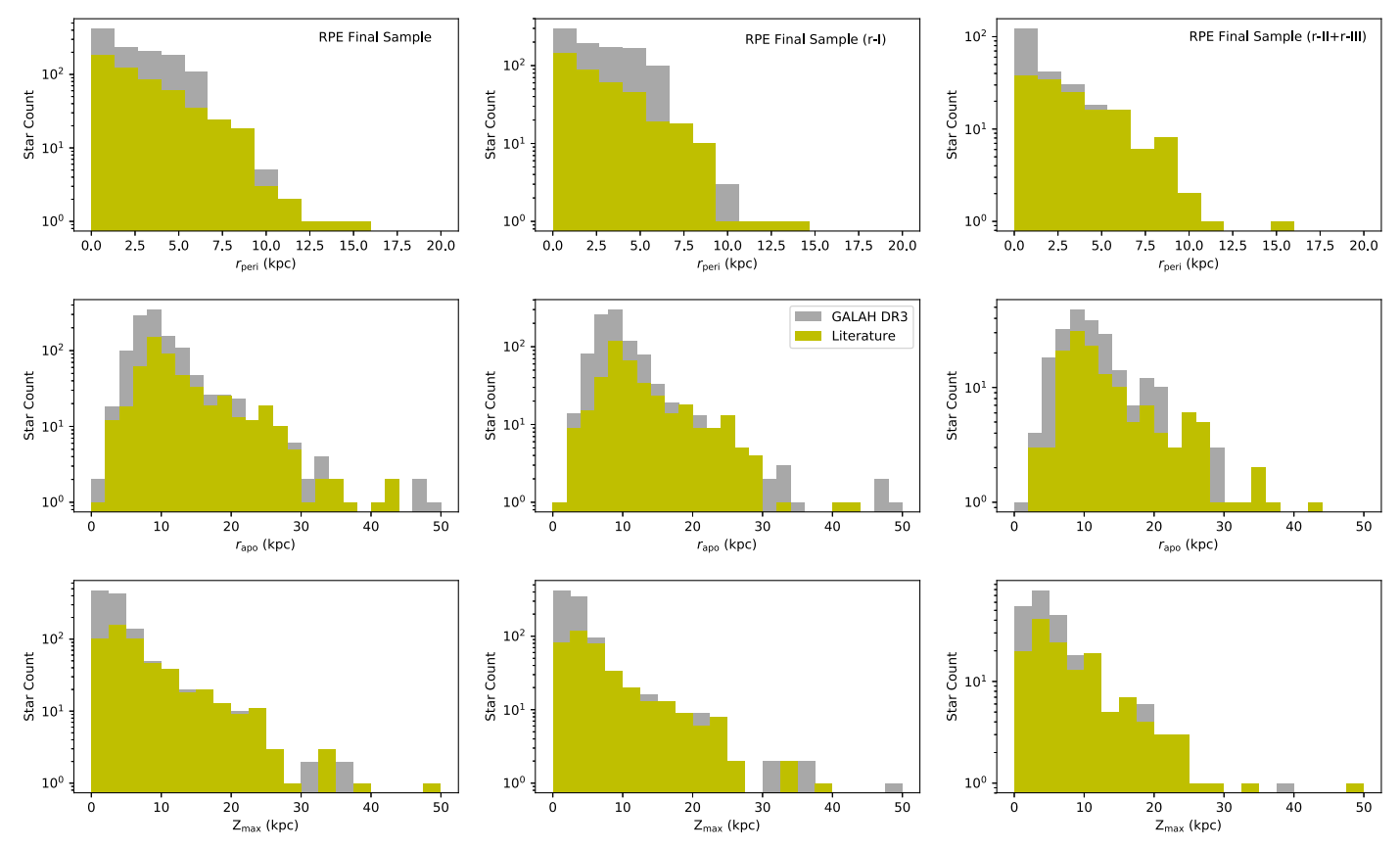


**Figure 8.** All panels: the literature subset of the RPE final sample is represented as a yellow histogram; the GALAH DR3 subset is represented as a gray histogram. Left column: logarithmic histograms of the orbital parameters  $r_{\text{peri}}$  (top),  $r_{\text{apo}}$  (middle), and  $Z_{\text{max}}$  (bottom) for the RPE final sample. Note that a few stars have  $r_{\text{apo}}$  and  $Z_{\text{max}}$  outside the range shown in the panels. Middle column: logarithmic histograms of the orbital parameters  $r_{\text{peri}}$  (top),  $r_{\text{apo}}$  (middle), and  $Z_{\text{max}}$  (bottom) for the RPE final sample with only r-I stars. Right column: logarithmic histograms of the orbital parameters  $r_{\text{peri}}$  (top),  $r_{\text{apo}}$  (middle), and  $Z_{\text{max}}$  (bottom) for the RPE final sample with only r-III stars.

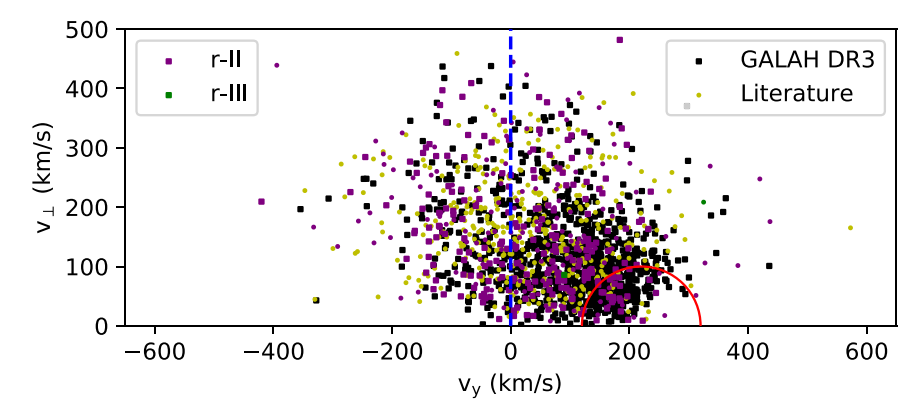


Figure 9. Toomre diagram of the RPE final sample. The literature subset of the RPE initial sample is represented as yellow points for *r*-I stars; the GALAH DR3 subset is represented as black squares for *r*-I stars. The *r*-II stars for the RPE final sample are indicated in purple, and *r*-III stars are indicated in green. The axes are  $v_{\perp} = \sqrt{v_x^2 + v_z^2}$  vs.  $v_y$ . The red circle represents stars within a 100 km s<sup>-1</sup> radius from the local standard of rest (232 km s<sup>-1</sup>), while the vertical-blue-dashed line represents the division between prograde ( $v_y > 0$  km s<sup>-1</sup>) and retrograde ( $v_y < 0$  km s<sup>-1</sup>) stellar orbits.

are performed based on physically motivated choices for each substructure, excluding previously defined substructures, as the process iterates to decrease contamination between substructures. Following their procedures, we find six predominant MW substructures associated with our CDTGs, listed in Table 5. This table provides the number of stars, the mean and dispersion of their chemical abundances, and the mean and dispersion of their dynamical parameters for each substructure. A Lindblad diagram and projected-action plot for these substructures are shown in Figure 10.

# 4.1.1. Gaia-Sausage-Enceladus

The most populated substructure identified here is Gaia-Sausage-Enceladus (GSE), which contains 155 member stars across the associated CDTGs. The selection criteria for GSE is  $\langle ecc \rangle > 0.7$  (Naidu et al. 2020). These CDTGs are distinct chemodynamical groups within GSE, as detected by previous authors as well, showing that, as a massive merger, GSE has distinct dynamical groupings within the progenitor satellite (Yuan et al. 2020a; Limberg et al. 2021b; Gudin et al. 2021;

Table 2
Identified CDTGs

CDTG	N Stars	Confidence	Associations with Previously Identified MW Substructure and Dynamical Groups
1	22	93.1%	DS22a:DTG-15, DS22a:DTG-16
2	21	100.0%	GSE, IR18:E, DG21:CDTG-1, KH22:DTC-15, DS22b:DTG-7, SL22:3, DS22a:DTG-22, EV21:NGC4833, DS22b:DTG-27, GL21:DTG-37
3	18	98.9%	DS22b:DTG-1, DS22b:DTG-43
4	18	68.7%	GSE, DS22b:DTG-30, DG21:CDTG-13, DG21:CDTG-28, DS22a:DTG-18, GC21:Sausage, KH22:DTC-2
5	17	87.5%	GSE, AH17:VelHel-6, DG21:CDTG-9, DS22a:DTG-3, SL22:3
6	16	96.1%	Splashed disk, DS22b:DTG-62, DG21:CDTG-5, DS22a:DTG-19
7	16	73.8%	MWTD, KH22:DTC-4, DS22b:DTG-14, DG21:CDTG-7, DS22b:DTG-99, DG21:CDTG-6, KM22:C-3, DS22b:DTG-97
8	14	91.4%	GSE, KH22:DTC-15, DS22b:DTG-57, DS22b:DTG-58, DG21:CDTG-18
			GL21:DTG-18, GC21:Sausage, DS22a:DTG-11, EV21:Ryu 879 (RLGC 2)
9	12	95.7%	Splashed disk, KH22:DTC-24, DG21:CDTG-25
10	12	99.8%	DS22b:DTG-5, DS22b:DTG-16
11	11	62.3%	GSE, EV21:NGC 5986, DG21:CDTG-29, KH22:DTC-19, EV21:NGC 6293, EV21:NGC 6402 (M 14)
12	11	88.4%	GSE, DG21:CDTG-14, DS22b:DTG-78, KH22:DTC-10, KH22:DTC-13, GM17:Comoving, KH22:DTC-16, KM22:C-3
13	11	97.0%	DS22b:DTG-158
14	11	74.8%	KM22:C-3
15	10	43.0%	GSE, SM20:Sausage, GC21:Sausage, GL21:DTG-11, EV21:IC 1257
16	10	94.7%	New
17	10	95.6%	Helmi stream, DG21:CDTG-15, HK18:Green, NB20:H99, DS22b:DTG-42, SL22:60, GL21:DTG-3, GM18a:S2, GM18b:S2
18	9	43.5%	KH22:DTC-13, DS22b:DTG-4, KM22:C-3
19	9	61.6%	GSE, DG21:CDTG-10, KH22:DTC-2, SL22:6, DS22b:DTG-115, GC21:Sausage, GL21:DTG-24
20	9	86.4%	GSE, GL21:DTG-14, DS22b:DTG-12, DG21:CDTG-13, GM17:Comoving, GC21:Sausage, EV21:Ryu 879 (RLGC 2)
21	9	97.0%	GSE, DS22b:DTG-18, DG21:CDTG-12
22	8	57.4%	Thamnos, DG21:CDTG-27, KH22:DTC-16, GC21:Sequoia, KM22:C-3
23	8	90.8%	Splashed disk, AH17:VelHel-6, DG21:CDTG-11, DS22b:DTG-29
24	8	99.9%	GSE, DS22b:DTG-114
25	8	93.5%	LMS-1, DG21:CDTG-4, DS22b:DTG-67, GM18b:Cand10, GM18b:Cand11, GL21:DTG-2
26	7	91.8%	DS22b:DTG-121
27	7	99.5%	DG21:CDTG-18, KH22:DTC-13, KH22:DTC-17, DS22b:DTG-4, GM17:Comoving, KM22:Ophiuchus, KM22:C-3
28	7	63.5%	EV21:NGC 362, KH22:DTC-17, KH22:DTC-9, GM17:Comoving, KM22:C-3
29	6	56.0%	DS22a:DTG-32
30	6	73.6%	DG21:CDTG-23, KH22:DTC-24, DS22b:DTG-11
31	6	93.3%	New
32	6	63.7%	GSE, DS22b:DTG-95, DS22b:DTG-8, SL22:3, GC21:Sausage, GL21:DTG-34
33	6	77.0%	GSE, GL21:DTG-23, DG21:CDTG-13, KH22:DTC-5, GM17:Comoving, GC21:Sausage, KH22:DTC-2, DS22a:DTG-10
34	6	89.9%	GSE, DG21:CDTG-21, KH22:DTC-3
35	5	48.9%	New
36	5	99.1%	EV21:NGC 6397, DS22b:DTG-55, KH22:DTC-4, DS22a:DTG-9

Note. We adopt the nomenclature for previously identified DTGs and CDTGs from Yuan et al. (2020a). For example, IR18:E is the first initial and last initial of the first author (IR) (Roederer et al. 2018), the year the paper was published (18), and after the colon is the group obtained by the authors of the paper (E). We use the following references for associations: AH17: Helmi et al. (2017), GM17: Myeong et al. (2017), HK18: Koppelman et al. (2018), GM18a: Myeong et al. (2018a), GM18b: Myeong et al. (2018b), IR18: Roederer et al. (2018), HL19: Li et al. (2019), SF19: Sestito et al. (2019), ZY19: Yuan et al. (2019), NB20: Borsato et al. (2020), HL20: Li et al. (2020), SM20: Monty et al. (2020), ZY20a: Yuan et al. (2020a), ZY20b: Yuan et al. (2020b), GC21: Cordoni et al. (2021), DG21: Gudin et al. (2021), CK21: Kielty et al. (2021), GL21: Limberg et al. (2021b), KH22: Hattori et al. (2022), KM22: Malhan et al. (2022), DS22a: Shank et al. (2022a), DS22b: Shank et al. (2022b), and SL22: Lövdal et al. (2022).

(This table is available in machine-readable form.)

Lövdal et al. 2022). GSE is thought to be the remnant of an early merger that distributed a significant number of stars throughout the inner halo of the MW (Belokurov et al. 2018; Helmi et al. 2018). The action space determined for the member stars exhibits an extended radial component, a null azimuthal component within errors, and a null vertical component within errors. These orbital properties are the product of the high-eccentricity selection of the CDTGs, and agree with previous findings of GSE orbital characteristics when using other selection criteria (Myeong et al. 2018a; Koppelman et al. 2018; Limberg et al. 2021b, 2022).

The  $\langle [Fe/H] \rangle$  of GSE found in our work ( $\sim -1.5$ ) is rather metal-poor, consistent with studies of its metallicity in other

dynamical groupings, even though our sample contains more metal-rich stars that could have been associated with GSE (Limberg et al. 2021b; Gudin et al. 2021; Shank et al. 2022b). The stars that form CDTGs in GSE tend to favor the more metalpoor tail of the substructure, which is also seen in previous dynamical analyses. The  $\langle [Mg/Fe] \rangle$  ( $\sim$ +0.3) of GSE exhibits a relatively low level, consistent with the low-Mg structure detected by Hayes et al. (2018) and with Mg levels consistent with accreted structures simulated by Mackereth et al. (2019), and explained through an accretion origin of GSE. We also obtain a  $\langle [C/Fe]_c \rangle$  ( $\sim$ +0.4) for GSE; this elevated C level is indicative of being produced in Type II supernovae, in agreement with the scenario put forth by Hasselquist et al. (2021) for GSE.

Table 3
CDTGs Identified by HDBSCAN

NAME	(Fe/H)	$(C/Fe)_c$	(Mg/Fe)	(Sr/Fe)	(Y/Fe)	(Ba/Fe)	(Eu/Fe)
			CDTC	5-1			
		Str	ucture: unassi	gned structure			
		Group assoc	iation: DTG-1	5: Shank et al. (202	2b)		
		Group assoc	iation: DTG-1	6: Shank et al. (202	2b)		
		Stellar a	ssociation: no	stellar associations	•		
		Globular a	ssociation: no	globular association	ıs		
		Dwarf galaxy a	ssociation: no	dwarf galaxy associ	iations		
140609001101322	-1.15	+0.47			+0.21	+0.63	+0.75
170417004501188	-0.86	+0.56			+0.10	+0.29	+0.46
170510003301241	-1.06	+0.50			+0.29	+0.49	+0.53
160519003601012	-1.33	+0.37			+0.43	+0.51	+0.74
160419003601272	-0.84	+0.57			+0.21	+0.32	+0.51
140414004101079	-0.96	+0.53			-0.27	-0.01	+0.56
160401004401264	-0.89	+0.56			+0.23	+0.17	+0.48
160327005601145	-1.01	+0.63		+1.14	+0.11	+0.30	+0.62
170312001601291	-0.91	+0.51			+0.43	+0.42	+0.49
150603002301086	-0.96	+0.51		•••	+0.37	+0.43	+0.58
140412002201386	-1.35	+0.62		•••	+0.40	+0.41	+0.51
140611001601101	-1.35	+0.52			+0.27	-0.10	+0.54
150703002602272	-1.44	+0.59		•••	+0.12	+0.28	+0.46
170712002601049	-0.84	+0.52		•••	+0.18	+0.38	+0.62
140711001301278	-0.89	+0.54		•••	+0.30	+0.31	+0.39
150413004601222	-0.85	+0.57		•••	+0.11	+0.16	+0.63
160421005101363	-1.06	+0.48		•••	+0.43	+0.41	+0.47
180625004301097	-1.00	+0.46		•••	+0.46	+0.50	+0.50
150607005101057	-0.86	+0.52		•••	+0.74	+0.53	+0.56
J204534.54-143115.1	-2.81	+0.51	•••	+0.13	•••	-0.12	+0.31
180604006201048	-1.19	+0.41	•••	•••	-0.11	+0.20	+0.37
160817003101018	-0.81	+0.44		•••	+0.09	+0.12	+0.45
$\mu \pm \sigma([{ m X/Y}])$	$-1.00\pm0.20$	$\mathbf{+0.52} \pm 0.06$		$+$ 0.64 $\pm$	$\mathbf{+0.24} \pm 0.20$	$\mathbf{+0.32} \pm 0.20$	$+0.51 \pm 0.10$

**Note.**  $\mu$  and  $\sigma$ , bolded for clarity, represent the biweight estimates of the location and scale for the abundances in the CDTG. (This table is available in its entirety in machine-readable form.)

The RPE stars associated with GSE exhibit Eu enhancement on par with other detected MW substructures ( $\langle \text{[Eu/Fe]} \rangle \sim +0.6$ ). Recently, Matsuno et al. (2021) and Naidu et al. (2021) tracked the formation of RPE stars in GSE, finding high levels of Eu present within identified GSE stars, consistent with the work presented here. Finally, we can associate the globular clusters Ryu 879 (RLGC2), IC 1257, NGC 4833, NGC 5986, NGC 6293, and NGC 6402 (M14) with GSE, based on CDTGs with similar orbital characteristics and stellar associations of these globular clusters (see Section 4.3 for details). Note in Figure 10 how GSE occupies a large region of the Lindblad diagram, concentrated in the planar and radial portions of the projected-action plot.

# 4.1.2. The Splashed Disk

The second-most populated substructure identified here is the splashed disk (SD), which contains 36 member stars. The SD is thought to be a component of the primordial MW disk that was kinematically heated during the GSE merger event (Helmi et al. 2018; Di Matteo et al. 2019; Belokurov et al. 2020). The selection criteria for the SD is  $\langle [\alpha/Fe] \rangle > 0.25 - 0.5 \times (\langle [Fe/H] \rangle + 0.7)$  (Naidu et al. 2020). The mean velocity components of the SD are consistent with a null radial and vertical velocity, while showing a large positive azimuthal velocity consistent with disk-like stars. The mean eccentricity of these stars is most consistent with disk-like orbits. The SD is the most metal-rich substructure identified

here ( $\langle [Fe/H] \rangle \sim -1.1$ ). The high  $\langle [Mg/Fe] \rangle$  ( $\sim +0.5$ ) abundances for the SD shows that these stars are old, and they could be the result of a possible merger event, such as the merger between the MW and GSE progenitor, or heated from a primordial system present within the MW at the time of the GSE merger. The  $\langle [C/Fe]_c \rangle$  ( $\sim +0.5$ ) abundance for the SD is high, which is consistent with the expectation from the high mean magnesium abundances as a tracer of Type II supernovae in this substructure (Woosley & Weaver 1995; Kobayashi et al. 2006).

Note that the SD overlaps with the metal-weak thick disk (MWTD) in the Lindblad diagram (Figure 10). This is due to the selection criteria only using metallicity and Mg abundances to determine the SD stars (Naidu et al. 2020). Considering the SD is thought to be composed of stars that have been heated due to the GSE merger event, the positions of the SD stars in the Lindblad diagram show a relatively large deviation from disk-like orbits, though some seem to have certainly been less kinematically displaced.

#### 4.1.3. The MWTD

The third-most populated substructure identified here is the MWTD, which contains 16 member stars. The MWTD is thought to have formed from either a merger scenario, possibly related to GSE, or the result of old stars born within the solar radius migrating out to the solar position due to tidal instabilities within the MW (Carollo et al. 2019). The selection

Table 4
CDTG Dynamical Parameters Determined by AGAMA

Cluster	N Stars	$(\langle v_r \rangle,  \langle v_\phi \rangle,  \langle v_z \rangle)$	$(\langle J_r  angle,  \langle J_\phi  angle,  \langle J_z  angle)$	$\langle E  angle$	⟨ecc⟩
		$(\sigma_{\langle v_r \rangle}, \sigma_{\langle v_\phi \rangle}, \sigma_{\langle v_z \rangle}) \ (\mathrm{km \ s}^{-1})$	$(\sigma_{\langle J_r \rangle}, \sigma_{\langle J_\phi \rangle}, \sigma_{\langle J_z \rangle}) \ (\mathrm{kpc} \ \mathrm{km} \ \mathrm{s}^{-1})$	$(10^5 \text{ km}^2 \text{ s}^{-2})$	$\sigma_{ m \langle ecc  angle}$
CDTG-1	22	(-48.4,86.3, -0.9) (67.6,16.6,46.0)	(278.9,535.9,66.5) (57.6,106.8,24.4)	-1.858 $0.028$	0.639 0.076
CDTG-2	21	(29.7,23.3, -5.5) (79.1,12.7,53.6)	(567.6,174.9,54.2) (34.4,94.6,26.0)	-1.819 $0.023$	0.886 0.047
CDTG-3	18	(-34.6,120.4, -3.6) (52.6,22.3,38.8)	(173.5,823.0,34.3) (52.7,80.1,9.9)	-1.831 0.018	0.473 0.076
CDTG-4	18	(-39.4, -8.4, -11.2) (150.4,17.5,55.8)	(794.4, -79.5,91.0) (47.8,144.9,27.3)	-1.677 0.019	0.937 0.037
CDTG-5	17	(130.4,17.3,53.8) (-32.8,24.3, -3.9) (112.8,7.0,28.9)	(\$7.6,144.9,27.3) (836.6,249.5,50.9) (50.9,84.2,25.3)	-1.632 0.043	0.900 0.037
CDTG-6	16	(112.8,7.0,28.9) (-33.7,183.1,0.2) (50.7,19.5,21.8)	(76.3,1396.5,14.1) (23.4,50.8,8.0)	-1.679 0.011	0.262 0.041
CDTG-7	16	(16.8,73.1, -58.3)	(285.9,487.8,283.1)	-1.752	0.636
CDTG-8	14	(107.5,23.7,95.5) (-59.7, -4.8,5.5)	(80.5,152.3,32.7) (543.4, -28.3,339.6)	0.041 -1.708	0.096
CDTG-9	12	(140.7,20.2,117.2) (-3.5,168.5,6.2)	(51.5,117.8,37.7) (117.7,1337.4,54.8)	0.028 -1.651	0.042
CDTG-10	12	(72.5,13.9,54.9) (-18.3,200.0, -40.1)	(29.2,26.6,7.6) (23.0,1390.5,117.9)	0.017 -1.652	0.038 0.147
CDTG-11	11	(35.9,19.9,73.9) (-37.2,2.1, -10.6)	(15.0,34.8,14.6) (128.6, -3.6,148.2)	0.012 $-2.152$	0.048 0.746
CDTG-12	11	(87.5,82.1,63.8) (17.1, -7.6,33.8)	(44.2,197.1,29.5) (516.9, -91.8,620.2)	$0.035 \\ -1.614$	0.140 0.770
CDTG-13	11	(144.3,30.9,156.0) (5.8,191.7, -2.5)	(87.3,241.3,56.2) (56.9,1626.4,29.6)	$0.058 \\ -1.603$	0.036 0.211
CDTG-14	11	(50.1,12.3,29.9) (-21.3,80.4, -39.5)	(38.9,61.6,8.2) (260.8,540.7,164.2)	$0.008 \\ -1.808$	0.070 0.616
CDTG-15	10	(62.8,11.9,62.1) (-309.4, -13.6, -20.2)	(52.6,75.7,10.2) (1505.8, -103.2,88.0)	0.028 - 1.393	0.056 0.972
CDTG-16	10	(214.0,24.6,110.4) (2.5,174.8,14.5)	(71.0,163.3,32.9) (123.6,1493.6,117.4)	0.026 -1.579	0.016 0.316
CDTG-17	10	(75.1,26.8,57.2) (-27.4,172.2, -161.4)	(42.7,44.0,12.0) (288.1,1316.5,1039.7)	0.014 $-1.347$	0.055 0.398
CDTG-18	9	(113.5,42.5,119.1) (-15.7, -49.2, -60.5)	(131.7,164.5,79.1) (331.2, -339.9,865.5)	0.057 $-1.592$	0.086 0.588
CDTG-19	9	(60.9,69.7,188.3) (-30.0,5.0, -20.6)	(84.8,299.9,55.8) (1105.1,36.6,40.5)	0.054 $-1.578$	0.104 0.971
CDTG-20	9	(212.6,6.4,36.1) (30.2,11.2, -88.3)	(53.6,52.9,22.0) (674.8,89.5,187.1)	0.027 $-1.692$	0.030 0.922
CDTG-21	9	(124.4,13.9,70.4) (6.9, -41.7, -8.4)	(44.8,111.3,15.4) (433.7, -279.8,71.4)	0.017 $-1.853$	0.036 0.788
CDTG-22	8	(64.8,15.7,65.2) (12.9, -101.8, -40.4)	(72.0,86.1,7.8) (238.3, -676.5,330.7)	$0.027 \\ -1.678$	0.078 0.537
CDTG-23	8	(99.2,27.3,108.7) (-26.8,92.8,14.7)	(51.9,111.7,22.5) (343.3,767.1,68.0)	$0.025 \\ -1.726$	0.059 0.605
CDTG-24	8	(95.2,11.0,47.9) (5.4,37.9,63.8)	(17.0,47.3,19.7) (230.5,168.6,263.1)	0.011 -1.944	0.016 0.787
CDTG-25	8	(39.3,12.9,103.1) (-58.7,56.3, -93.9)	(27.3,66.0,21.0) (639.6,520.7,2011.1)	0.025 -1.248	0.079 0.525
CDTG-26	7	(66.8,51.6,267.1) (-15.7,184.3,9.7)	(238.6,426.3,62.5)	0.063 -1.650	0.084 0.223
		(45.8,4.9,23.0)	(56.0,1464.9,34.2) (13.8,23.5,9.3)	0.006	0.024
CDTG-27	7	(80.8, -2.5, -80.6) (62.4,36.6,212.0)	(389.0, -15.1,1113.5) (119.5,142.0,37.4)	-1.543 0.058	0.613
CDTG-28	7	(-6.7,15.8, -76.1) (150.1,46.3,183.3)	(375.8,138.0,1486.5) (187.7,369.1,97.5)	-1.415 0.081	0.493
CDTG-29	6	(-13.7,158.0, -6.9) (51.2,5.3,19.2)	(103.6,1216.9,9.9) (14.0,18.0,3.5)	-1.730 0.009	0.321 0.021
CDTG-30	6	(-32.1,159.4, -0.6) (69.5,11.1,21.6)	(117.7,1123.3,28.3) (9.4,32.4,8.0)	-1.745 $0.004$	0.354 0.009
CDTG-31	6	(-20.1,144.1, -8.3) (46.7,7.9,63.5)	(112.0,1041.3,55.5) (21.9,29.0,11.2)	-1.765 $0.010$	0.356 0.036

Table 4 (Continued)

Cluster	N Stars	$(\langle v_r \rangle,  \langle v_\phi \rangle,  \langle v_z \rangle)$	$(\langle J_r  angle,  \langle J_\phi  angle,  \langle J_z  angle)$	$\langle E \rangle$	⟨ecc⟩
		$(\sigma_{\langle v_r \rangle}, \sigma_{\langle v_\phi \rangle}, \sigma_{\langle v_z \rangle}) \ (\mathrm{km \ s}^{-1})$	$(\sigma_{\langle J_r \rangle}, \sigma_{\langle J_\phi \rangle}, \sigma_{\langle J_z \rangle})$ (kpc km s <sup>-1</sup> )	$(10^5 \text{ km}^2 \text{ s}^{-2})$	$\sigma_{ m \langle ecc  angle}$
CDTG-32	6	(107.8,1.0,1.8)	(738.0,12.3,40.6)	-1.748	0.921
		(169.4,12.8,42.5)	(42.3,91.5,8.1)	0.019	0.043
CDTG-33	6	(136.3,6.2, -21.6)	(990.0,31.1,110.5)	-1.583	0.967
		(272.5,10.5,70.6)	(7.9,69.8,9.5)	0.010	0.022
CDTG-34	6	(-217.9,54.2, -35.5)	(875.2,398.2,190.0)	-1.521	0.865
		(70.4,12.5,104.1)	(39.5,49.7,12.3)	0.007	0.027
CDTG-35	5	(-75.7,162.5, -8.7)	(73.8,841.5,35.5)	-1.891	0.333
		(11.4,5.7,18.6)	(9.3,48.1,6.5)	0.015	0.028
CDTG-36	5	(-9.9,124.2, -27.9)	(114.4,763.0,152.8)	-1.816	0.406
		(53.4,11.1,87.1)	(6.9,55.7,20.1)	0.013	0.012

(This table is available in machine-readable form.)

criteria for the MWTD is  $-0.8 < \langle [Fe/H] \rangle < -2.5, +0.25 <$  $\langle [\alpha/\text{Fe}] \rangle < +0.45$ , and  $\langle J_{\phi} \rangle > 0.5$  (Naidu et al. 2020). The relative lack of RPE stars in the MWTD agrees with simulations performed by Hirai et al. (2022), which show that the in situ component does not possess large numbers of highly enhanced r-II stars ( $\langle [Eu/Fe] \rangle \sim +0.6$ ). The nonexistent radial and vertical velocity components, as well as the large positive azimuthal velocity component of the MWTD are all consistent with the velocity distribution for the MWTD from Carollo et al. (2019), even though the [Fe/H] cut in our dynamical analysis included more metal-rich stars than in their sample. The mean eccentricity distribution found within this substructure is also similar to that reported by Carollo et al. (2019), showing that the MWTD is a distinct component from the canonical thick disk (TD). Recently, both An & Beers (2020) and Dietz et al. (2021) presented evidence that the MWTD is a structure that is independent of the TD.

The distribution in  $\langle [Fe/H] \rangle$  ( $\sim$ -1.9) and mean velocity space represents a stellar population consistent with the high-Mg population (Hayes et al. 2018) ( $[Fe/H] \sim -1.3$ ), with the mean Mg abundance ( $\langle [Mg/Fe] \rangle \sim +0.4$ ) being similar within errors ( $[Mg/Fe] \sim +0.3$ ). The  $\langle [C/Fe]_c \rangle$  ( $\sim$ +0.5) abundance for the MWTD exhibits an enhancement in carbon, possibly pointing to a relation with the strongly prograde CEMP structure found in Dietz et al. (2021), which was attributed to the MWTD population. While this population is not explicitly recovered, there could be an overlap, and future studies will shed more light on this as new abundance information is explored.

Interestingly, the MWTD does not have many identified RPE stars compared to detections of this substructure in previous works that did not focus solely on RPE stars (Shank et al. 2022a, 2022b). This could be due to the primordial MW disk not being enhanced in *r*-process elements, as shown for the *r*-II star simulations in Hirai et al. (2022), or a selection effect, with more stars with Mg abundances needing to be identified in the disk of the MW (note there are only 395 stars with Mg abundances detected, which are needed to determine the MWTD substructure based on the procedure in Naidu et al. 2020). If future abundance measurements show that relatively few RPE stars are identified for the MWTD, then the formation scenarios of the primordial disk can be further constrained.

Notice in Figure 10 how the MWTD occupies a lower energy component of the disk (the gray dots are mostly positioned with prograde orbits) in the Lindblad diagram, along with being in a more extended disk position as well, a selection that is seen in Naidu et al. (2020).

#### 4.1.4. The Helmi Stream

The third-least populated substructure identified here is the Helmi stream (HS), which contains 10 member stars. The HS is one of the first detected dynamical substructures in the MW using integrals of motions (Chiba & Yoshii 1998; Helmi & White 1999; Chiba & Beers 2000). The selection criteria for the HS is  $0.75 \times 10^3 < \langle J_{\phi} \rangle < 1.7 \times 10^3$  and  $1.6 \times 10^3 < \langle L_{\perp} \rangle < 3.2 \times 10^3$ , with  $L_{\perp} = \sqrt{L_x^2 + L_y^2}$  (Naidu et al. 2020). The HS has a characteristically high vertical velocity, which separates it from other stars that lie in the disk, and can be seen in the sample here. The large uncertainty on the vertical velocity of the HS members corresponds to the positive and negative vertical velocity components of the stream, with the negative vertical velocity population dominating, consistent with the members determined here (Helmi 2020).

The  $\langle {\rm [Fe/H]} \rangle$  of the HS is more metal-poor in this sample  $(\langle {\rm [Fe/H]} \rangle \sim -2.0),$  compared to the known HS members ([Fe/H]  $\sim -1.5;$  Koppelman et al. 2019a). However, Limberg et al. (2021a) recently noted that the metallicity range of HS is more metal-poor than previously expected, with stars reaching [Fe/H]  $\sim -2.5,$  which is consistent with both the study performed by Roederer et al. (2010) and the results presented here within errors. Limberg et al. (2021a) also considered *r*-process abundances for the HS, showing that [Eu/Fe] (>+0.3) is larger over the wide range of metallicities (-2.5  $\lesssim$  [Fe/H]  $\lesssim -1.0$ ), as also found for the stars reported in this work ( $\langle {\rm [Eu/Fe]} \rangle \sim +0.5$ ). Notice in Figure 10 how the HS occupies a relatively isolated space in the Lindblad diagram, thanks to the large vertical velocity of the stars providing the extra energy compared to the other disk stars.

# 4.1.5. LMS-1 (Wukong)

The second-least populated substructure identified here is LMS-1, which contains eight member stars. LMS-1 was first identified by Yuan et al. (2020a), and also detected by

Table 5
Associations with Previously Known MW Substructures

												T
MW Substructure	N Stars	⟨(Fe/H)⟩	$\langle ({ m C/Fe})_c  angle$	$\langle ({ m Mg/Fe})  angle$	((Sr/Fe))	((Y/Fe))	⟨(Ba/Fe)⟩	$\langle (Eu/Fe)  angle$	$(\langle v_r \rangle, \langle v_\phi \rangle, \langle v_z \rangle) \ (\sigma_{(v_r)}, \sigma_{(v_\phi)}, \sigma_{(v_z)}) \ (\operatorname{Km} \operatorname{s}^{-1})$	$(\langle J_r  angle, \langle J_\phi  angle, \langle J_z  angle) \ (\sigma_{\langle J_r  angle}, \sigma_{\langle d_\phi  angle}, \sigma_{\langle d_\phi  angle}) \ ( ext{kpc km s}^{-1})$	$\langle E \rangle$ $\langle 10^5 \text{ km}^2 \text{ s}^{-2} \rangle$	(ecc) σ(ecc)
GSE	155	-1.53 0.61	+0.38 0.24	+0.31	+0.23	+0.12 0.24	+0.27 0.31	+0.60	(-16.9,9.9,-5.9) $(149.1,35.0,78.4)$	(693.3,55.8,159.2) (327.7,192.6,160.3)	-1.718 0.177	0.090
Splashed disk	36	-1.12 0.46	+0.45	+0.46	+0.60	+0.11	+0.17	+0.54	(-20.0,163.2,4.4) (67.9,41.6,39.7)	(149.3,1234.6,39.7) (107.7,256.0,26.0)	-1.682 0.028	0.361
MWTD	16	-1.93 0.72	+0.54 0.19	+0.43 0.12		+0.03	+0.16 0.26	+0.59	(11.4,83.9, -37.8) (102.0,40.4,89.9)	(288.2,492.1,282.5) (75.6,145.4,30.9)	-1.751 0.039	0.632
Helmi stream	10	-1.99 0.55	+0.17	+0.34	+0.09	-0.17 0.17	+0.05 0.29	+0.49	(-30.8,169.9, -153.6) (106.9,47.6,118.3)	(286.0,1269.0,1063.8) (126.3,160.2,75.6)	-1.348 0.054	0.380
LMS-1	∞	-2.18 0.51	+0.39	+0.43	+0.15	-0.24 0.06	+0.06	+0.49	(-14.9,51.1, -80.5) (121.4,47.0,250.3)	(597.9,409.8,2003.9) (229.6,368.3,105.0)	-1.252 0.060	0.497
Thamnos	∞	-2.06 0.58	+0.39	+0.54 0.16	+0.05	-0.02 0.21	+0.09 0.22	+0.54 0.21	(11.9, -120.6, -33.3) (95.4,51.3,102.0)	(248.2, -704.3,331.0) (48.1,94.1,21.7)	-1.679 0.024	0.536

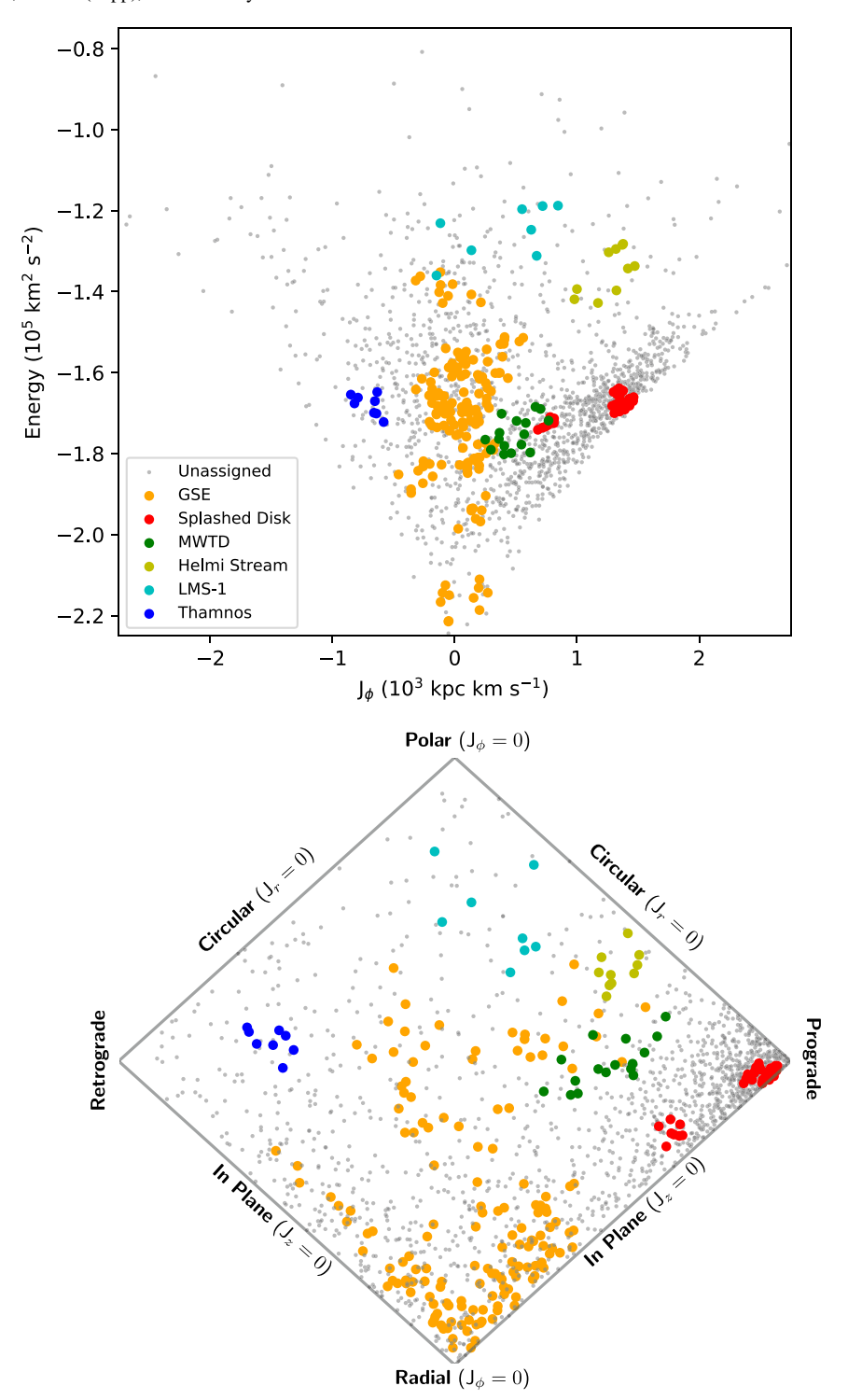


**Figure 10.** Top panel: Lindblad diagram of the identified MW substructures. The different structures are associated with the colors outlined in the legend. Bottom panel: the projected-action plot of the same substructures. This space is represented by  $J_{\phi}/J_{\text{Tot}}$  for the horizontal axis and  $(J_z - J_r)/J_{\text{Tot}}$  for the vertical axis with  $J_{\text{Tot}} = J_r + |J_{\phi}| + J_z$ . For more details on the projected-action space, see Figure 3.25 in Binney & Tremaine (2008).

Naidu et al. (2020), who called it Wukong. The selection for LMS-1 is  $0.2 \times 10^3 < \langle J_\phi \rangle < 1.0 \times 10^3$ ,  $-1.65 \times 10^5 < \langle E \rangle < -1.2 \times 10^5$ , and  $\langle [\text{Fe/H}] \rangle < -1.45$  (Naidu et al. 2020). This structure is similar to GSE in terms of the velocity component, but is characterized by a higher energy along with a more metal-poor population (Naidu et al. 2020), also found for the small number of stars representing LMS-1 in our sample

 $(\langle [Fe/H] \rangle \sim -2.2)$ . The carbon and magnesium abundances are also high, which indicates an old population  $(\langle [C/Fe]_c \rangle \sim +0.4)$  and  $\langle [Mg/Fe] \rangle \sim +0.4$ ). LMS-1 exhibits low first-peak r-process elements for both strontium and yttrium  $(\langle [Sr/Fe] \rangle \sim +0.2)$  and  $\langle [Y/Fe] \rangle \sim -0.2$ ). In Figure 10 LMS-1 has a higher energy compared to GSE in the Lindblad diagram. However, these stars exhibit a lower eccentricity  $(\langle ecc} \rangle \sim 0.5)$ 

compared to the GSE stars ( $\langle ecc \rangle > 0.7$ ), forming their own distinct substructure, with a more clear division in the projected-action plot.

#### 4.1.6. Thamnos

The Thamnos substructure also contains eight member stars. Thamnos was proposed by Koppelman et al. (2019b) as a merger event that populated stars in a retrograde orbit similar to TD stars. The selection criteria for Thamnos is  $-1.5 \times$  $10^3 < \langle J_{\phi} \rangle < -0.2 \times 10^3, -1.8 \times 10^5 < \langle E \rangle < -1.6 \times 10^5,$  and  $\langle [Fe/H] \rangle < -1.6$  (Naidu et al. 2020). The low energy and strong retrograde rotation suggest that Thamnos merged with the MW long ago (Koppelman et al. 2019b). Here we find a similar low mean orbital energy and strong mean retrograde motion, and we recover as strong a retrograde motion as in Koppelman et al. (2019b), within errors. The low mean metallicity ( $\langle [Fe/H] \rangle \sim -2.1$ ), consistent with the value reported by Limberg et al. (2021b) ( $\langle [Fe/H] \rangle \sim -2.2$ ), and the elevated  $\langle [C/Fe]_c \rangle$  ( $\sim +0.4$ ) of these stars also supports the merger being ancient. The  $\langle [Mg/Fe] \rangle$  ( $\sim +0.5$ ) is high, also suggesting an old population, consistent with Kordopatis et al. (2020) ([Mg/Fe]  $\sim +0.3$ ). As far as we are aware, this study presents the first known r-process-element abundances detected in Thamnos, with  $\langle [Eu/Fe] \rangle \sim +0.5$  and  $\langle [Ba/Fe] \rangle \sim +0.1$ , and shows that this old system was once subjected to multiple r-process events, probably before being accreted into the Galaxy. Notice in Figure 10 how Thamnos occupies a space that could be described as a retrograde version of disk stars.

# 4.2. Associations with Previously Identified Groups and MW Substructures

Separately, we can compare the newly identified CDTGs in this work with other dynamical groups identified by previous authors in order to find structures in common. We take the mean group dynamical properties from the previously identified groups and compare them to the mean and dispersion for the dynamical parameters of our identified CDTGs. Stellar associations of  $\hat{5}''$  are also considered, allowing the identification of stars in our sample that belong to previously identified groups. For details on the previous work used in this process, see Shank et al. (2022b). The resulting dynamical associations between our identified CDTGs and previously identified groups (along with substructure and globular cluster associations, see Section 4.3) are listed in Table 6. The previous groups that are associated with the identified CDTGs in this work are listed in Table 7. Table 3 lists the individual stellar associations for each of our CDTGs. The works that we use for previous groups are AH17: Helmi et al. (2017), GM17: Myeong et al. (2017), HK18: Koppelman et al. (2018), GM18a: Myeong et al. (2018a), GM18b: Myeong et al. (2018b), IR18: Roederer et al. (2018), HL19: Li et al. (2019), SF19: Sestito et al. (2019), ZY19: Yuan et al. (2019), NB20: Borsato et al. (2020), HL20: Li et al. (2020), SM20: Monty et al. (2020), ZY20a: Yuan et al. (2020a), ZY20b: Yuan et al. (2020b), GC21: Cordoni et al. (2021), DG21: Gudin et al. (2021), CK21: Kielty et al. (2021), GL21: Limberg et al. (2021b), KH22: Hattori et al. (2022), KM22: Malhan et al. (2022), DS22a: Shank et al. (2022a), DS22b: Shank et al. (2022b), and SL22: Lövdal et al. (2022). This work is distinguished from previous papers, thanks to the increase in RPE stars compared to Gudin et al. (2021), and preliminary abundance results for other elements such as Mg

**Table 6**Associations of Identified CDTGs

	11000014410110 01		
Structure	Reference	Associations	Identified CDTGs
MW substructure	Naidu et al. (2020)	GSE	2, 4, 5, 8, 11, 12, 15, 19, 20, 21, 24, 32, 33, 34
		Splashed disk	6, 9, 23
		Helmi stream	17
		LMS-1	25
		MWTD	7
		Thamnos	22
Globular clusters	Vasiliev & Baumgardt (2021)	Ryu 879 (RLGC 2)	8, 20
		IC 1257	15
		NGC 362	28
		NGC 4833	2
		NGC 5986	11
		NGC 6293	11
		NGC 6397	36
		NGC 6402 (M14)	11

and Y. Select identified CDTGs related to each of the large-scale substructures described in Section 4.1 (along with one that is not associated with large-scale substructure) are examined in detail below.

# 4.2.1. CDTG-6

CDTG-6 is associated with the SD (Naidu et al. 2020), and has interesting associations with previously identified groups. There are three stellar associations made between previously identified groups and CDTG-6, with two coming from DG21: CDTG-5,<sup>22</sup> and one coming from DS22a:DTG-62 (Gudin et al. 2021; Shank et al. 2022a). DG21:CDTG-5 is associated with the MWTD by the authors (Gudin et al. 2021). DS22a:DTG-62 is not associated with any MW substructure by the authors, though it is noted that there were no measured  $\alpha$ -element abundances for the stars belonging to DS22a:DTG-62 (Shank et al. 2022a). CDTG-6 has three dynamical associations with previously identified groups-DG21:CDTG-5, DS22a:DTG-62, and DS22b:DTG-19 (Gudin et al. 2021; Shank et al. 2022a, 2022b). DS22b:DTG-19 is associated with the MWTD by the authors (Shank et al. 2022b). CDTG-6 seems to point toward an association with either the MWTD or the SD, but clearly more Mg abundances are needed before definitive claims can be made. While there were three studies (Gudin et al. 2021; Shank et al. 2022a, 2022b) that had associations

<sup>&</sup>lt;sup>22</sup> We adopt the nomenclature for previously identified DTGs and CDTGs from Yuan et al. (2020a). For example, DG21:CDTG-5 is represented by the first initial and last initial of the first author (DG) (Gudin et al. 2021), followed by the year the paper was published (21), and after the colon is the group obtained by the authors of the paper (CDTG-5).

corresponding to the MWTD, Shank et al. (2022a) had limited  $\alpha$ -element abundance information.

#### 4.2.2. CDTG-7

CDTG-7 is the only group associated with the MWTD following the procedure in Naidu et al. (2020). Three stellar associations are made to DG21:CDTG-7, two to KH22:DTC-4, and one each to DG21:CDTG-6, DS22a:DTG-14, and DS22a: DTG-99. DG21:CDTG-7 is associated with GSE by the authors, while DG21:CDTG-6 is not associated with an MW substructure (Gudin et al. 2021). KH22:DTC-4 is not associated with any MW substructure, and is associated with IR18:C by the authors (Hattori et al. 2022). DS22a:DTG-14 is associated with the MWTD, with other associations to HL19: GL-1, DS22b:DTG-2, and DG21:CDTG-6 (Shank et al. 2022a). HL19:GL-1 is not associated with an MW substructure by the authors, and is also associated with AH17:VelHel-7 (Li et al. 2019). DS22b:DTG-2 is associated with the MWTD, and also associated with HL19:GL-1, DG21:CDTG-6, and DG21: CDTG-8, with DG21:CDTG-8 associated with the MWTD by the authors (Gudin et al. 2021; Shank et al. 2022b). DS22a: DTG-99 is not associated with any MW substructure, and is also associated with HL19:GL-1 by the authors (Shank et al. 2022a). CDTG-7 is also dynamically associated with KM22:C-3 and DS22a:DTG-97 (Shank et al. 2022a; Malhan et al. 2022). KM22:C-3 is not associated with an MW substructure by the authors, while DS22a:DTG-97 is associated with GSE and also HL20:GR-1 (Shank et al. 2022a; Malhan et al. 2022). HL20: GR-1 is associated with AH17:VelHel-7, HL19:GL-1, and HL19:GL-2 by the authors, none of which are recovered here (Li et al. 2020). Interestingly, CDTG-7 has a few associations with GSE, but does not have a strong enough eccentricity  $(\langle ecc \rangle \sim 0.64)$  to be determined as GSE according to the procedure by Naidu et al. (2020) ( $\langle ecc \rangle > 0.7$ ). The chemical information relates this more to the MWTD compared to GSE, with both  $\langle [C/Fe]_c \rangle$  (~+0.5) and  $\langle [Mg/Fe] \rangle$  (~+0.4) being more abundant in CDTG-7 compared to the detected abundances in GSE presented here ( $\sim+0.4$  and  $\sim+0.3$ , respectively). In total, there are seven associations between CDTG-7 and previous works, with two associations being related to the MWTD and two to GSE by the previous authors, the rest were not associated with large-scale substructure.

#### 4.2.3. CDTG-8

CDTG-8 is associated with GSE (Naidu et al. 2020), and has interesting associations with previously identified groups. Taking a closer look at CDTG-8, we have six stellar associations for CDTG-8 with two in KH22:DTC-15, and a star in each of GL21:DTG-18, DG21:CDTG-18, DS22a:DTG-57, and DS22a:DTG-58 (Limberg et al. 2021b; Gudin et al. 2021; Shank et al. 2022a). KH22:DTC-15 is associated with Pontus (Malhan et al. 2022), not discussed in this work, by the authors (Hattori et al. 2022). KH22:DTC-15 is associated with IR18:E, IR18:F, IR18:H, and ZY20a:DTG-38 by the authors as well (Hattori et al. 2022). ZY20a:DTG-38 is related to GSE by the authors (Yuan et al. 2020a). GL21:DTG-18 was not associated with GSE by the authors, or any MW substructure; however, it was associated with ZY20a:DTG-33, which was also not associated with any MW substructure by the authors (Yuan et al. 2020b; Limberg et al. 2021b). DG21:CDTG-18 was also not assigned to an MW substructure by the authors,

while DS22a:DTG-57 and DS22a:DTG-58 were associated with GSE (Gudin et al. 2021; Shank et al. 2022a). CDTG-8 is dynamically associated with GC21:Sausage, DS22a:DTG-57, and DS22b:DTG-11, which are all associated with GSE by their authors (Cordoni et al. 2021; Shank et al. 2022a, 2022b). We also recover a globular cluster match with CDTG-8 to EV21:Ryu 879 (RLGC 2), which is typically associated with GSE dynamics (Shank et al. 2022a, 2022b; Callingham et al. 2022). There are eight associations between CDTG-8 and previous groups, with five being associated with GSE, one with Pontus, and the rest not associated with large-scale substructure by the previous authors.

#### 4.2.4. CDTG-17

Only one group is associated with the HS, CDTG-17. We can see that CDTG-17 has five stellar associations with DG21: CDTG-15, four with NB20:H99, four with SL22:60, three with HK18:Green, and one each with GL21:DTG-3 and DS22a: DTG-42 (Koppelman et al. 2018; Borsato et al. 2020; Limberg et al. 2021b; Gudin et al. 2021; Shank et al. 2022a; Lövdal et al. 2022). All of these groups were associated with the HS by their respective authors, with DG21:CDTG-15 also being associated with GL21:DTG-3 and ZY20a:DTG-3, of which we recover the GL21:DTG-3 association, and with ZY20a:DTG-3 being associated as HS members by the authors (Yuan et al. 2020b; Limberg et al. 2021b; Gudin et al. 2021). CDTG-17 is also dynamically associated with GM18a:S2, GM18b:S2, DG21:CDTG-15, GL21:DTG-3, and DS22a:DTG-42 which are all associated with the HS by their authors (Myeong et al. 2018a, 2018b; Limberg et al. 2021b; Gudin et al. 2021; Shank et al. 2022a). There are eight associations between CDTG-17 and previous groups, with all eight being assigned to the HS by the previous authors.

#### 4.2.5. CDTG-22

CDTG-22 is associated with Thamnos. CDTG-22 has three stellar associations with two belonging in DG21:CDTG-27, which is identified as belonging to Thamnos by the authors (Gudin et al. 2021), and one belonging in KH22:DTC-16, which is associated with IR18:B by the authors (Hattori et al. 2022). On the other hand, CDTG-22 has a dynamical association with GC21:Sequoia, belonging to Sequoia according to the authors (Cordoni et al. 2021). However, Sequoia is a higher energy structure compared to Thamnos (Koppelman et al. 2019a). CDTG-22 also has a dynamical association with KM22:C-3, which is not associated by the authors (Malhan et al. 2022). This is a case where CDTG-22 could be between the two substructures of Thamnos and Sequoia in terms of energy, and more information is required before a definitive conclusion can be made. There are four associations between CDTG-22 and previous groups, with one of those being associated with Thamnos, one being associated with Sequoia, and the other two not associated with large-scale substructure by the previous authors.

#### 4.2.6. CDTG-25

CDTG-25 is associated with LMS-1 (Wukong) through the procedure outlined in Naidu et al. (2020). There were six stars from previously identified groups matched with CDTG-25 through a 5" radius search of the CDTG-25 member stars. Three of the stars are in DG21:CDTG-4, and the other three are

Table 7
Associations of Identified CDTGs with Previous Groups

Table 7 (Continued)

DTG-4 DTG-1 DTG-5 DTG-7	18, 27 3	-	CDTG-14	12
DTG-5				
			CDTG-15	17
D1G-7	2		CDTG-21	34
DTC 0			CDTG-23	30
DTG-8	32		CDTG-25	9
DTG-11	30		CDTG-27	22
			CDTG-28	4
-			CDTG-29	11
		Hattori et al. (2022)	DTC-2	4, 19, 33
			DTC-13	12, 18, 27
			DTC-4	7, 36
			DTC-15	2, 8
			DTC-16	12, 22
DTG-42	17	Hattori et al. (2022)	DTC-17	27, 28
DTG-43	3		DTC-24	9, 30
DTG-55	36		DTC-3	34
DTG-57	8		DTC-5	33
DTG-58	8		DTC-9	28
DTG-62	6		DTC-10	12
DTG-67	25		DTC-19	11
DTG-78	12	Shank et al. (2022b)	DTG-3	5
DTG-95	32		DTG-9	36
DTG-97	7		DTG-10	33
DTG-99	7		DTG-11	8
DTG-114	24		DTG-15	1
DTG-115	19		DTG-16	1
DTG-121	26		DTG-18	4
DTG-158	13		DTG-19	6
CDTG-13	4 20 33		DTG-22	2
			DTG-32	29
		Limberg et al. (2021b)	DTG-2	25
			DTG-3	17
			DTG-11	15
	-		DTG-14	20
				8
			-	33
				19
			-	32
			-	2
_	DTG-43 DTG-55 DTG-57 DTG-58 DTG-62 DTG-67 DTG-78 DTG-95 DTG-97 DTG-97 DTG-99 DTG-114 DTG-115 DTG-121	DTG-14         7           DTG-16         10           DTG-18         21           DTG-27         2           DTG-29         23           DTG-30         4           DTG-42         17           DTG-43         3           DTG-55         36           DTG-57         8           DTG-58         8           DTG-62         6           DTG-78         12           DTG-95         32           DTG-97         7           DTG-99         7           DTG-114         24           DTG-115         19           DTG-121         26           DTG-158         13           CDTG-13         4, 20, 33           CDTG-14         25           CDTG-1         2           CDTG-1         2           CDTG-5         6           CDTG-7         7           CDTG-9         5           CDTG-10         19           CDTG-11         23	DTG-14         7           DTG-16         10           DTG-18         21           DTG-27         2           DTG-29         23           DTG-30         4           DTG-42         17           DTG-43         3           DTG-55         36           DTG-57         8           DTG-58         8           DTG-62         6           DTG-78         12           DTG-95         32           DTG-97         7           DTG-114         24           DTG-115         19           DTG-121         26           DTG-13         4, 20, 33           CDTG-18         8, 27           CDTG-1         2           CDTG-4         25           CDTG-5         6           CDTG-5         6           CDTG-7         7           CDTG-9         5           CDTG-10         19           CDTG-11         23	DTG-12         20           DTG-14         7           DTG-16         10           DTG-18         21           DTG-27         2           DTG-29         23           DTG-30         4           DTG-42         17           DTG-43         3           DTG-55         36           DTG-57         8           DTG-58         8           DTG-60         DTC-10           DTG-78         12           DTG-99         7           DTG-114         24           DTG-155         19           DTG-160         DTG-10           DTG-17         DTG-10           DTG-18         12           Shank et al. (2022b)         DTG-3           DTG-19         DTG-10           DTG-115         19         DTG-11           DTG-115         19         DTG-16           DTG-15         DTG-16         DTG-18           DTG-15         DTG-18         DTG-19           DTG-18         8, 27         DTG-18           CDTG-1         2         Limberg et al. (2021b)         DTG-2           DTG-11         DTG-1

Table 7 (Continued)

	(Continued)	
Reference	Associations	Identified CDTGs
Myeong et al. (2018b)	Cand10	25
	Cand11	25
	S2	17
Lövdal et al. (2022)	3	2, 5, 32
	6	19
	60	17
Cordoni et al. (2021)	Sausage Sequoia	4, 8, 15, 19, 20, 32, 33 22
Malhan et al. (2022)	C-3 Ophiuchus	7, 12, 14, 18, 22, 27, 28 27
Borsato et al. (2020)	H99	17
Helmi et al. (2017)	VelHel-6	5, 23
Koppelman et al. (2018)	Green	17
Monty et al. (2020)	Sausage	15
Myeong et al. (2017)	Comoving	12, 20, 27, 28, 33
Myeong et al. (2018a)	S2	17
Roederer et al. (2018)	Е	2

(This table is available in machine-readable form.)

in DS22a:DTG-67. DG21:CDTG-4 is not assigned (Gudin et al. 2021; Shank et al. 2022a), while DS22a:DTG-67 is associated with LMS-1 (Yuan et al. 2020a). DG21:CDTG-4 was associated with GL21:DTG-2 by the authors, where Limberg et al. (2021b) made a tentative association with LMS-1. These associations seem to strengthen their argument for GL21:DTG-2. CDTG-25 is also dynamically associated with GM18b:Cand10, GM18b:Cand11, DG21:CDTG-4, GL21: DTG-2, and DS22a:DTG-67 (Myeong et al. 2018b; Limberg et al. 2021b; Gudin et al. 2021; Shank et al. 2022a). Both GM18b:Cand10 and GM18b:Cand11 were new groups identified by Myeong et al. (2018b), though we note that LMS-1 was not discovered until 2 yr later by Yuan et al. (2020a), meaning that LMS-1 was possibly detected through a dynamical search for groups. There are five associations between CDTG-25 and previous groups, with two being associated with LMS-1 and the other three not associated with large-scale substructure by the previous authors.

#### 4.2.7. CDTG-36

CDTG-36 is not assigned to any MW substructure, and has two stellar associations with DS22a:DTG-55, and one each with DS22b:DTG-9, KH22:DTC-4, and EV21:NGC 6397 (Vasiliev & Baumgardt 2021; Shank et al. 2022a, 2022b; Hattori et al. 2022). All of the past groups are not assigned by their authors to any large-scale MW substructure, with EV21: NGC 6397 being a globular cluster. KH22:DTC-4 is associated with IR18:C by the authors (Hattori et al. 2022). Both DS22a: DTG-55 and DS22b:DTG-9 are also associated with NGC 6397 as well. Although we have presented a stellar association,

CDTG-36 has  $\langle {\rm [Fe/H]} \rangle \sim -0.9,$  as opposed to the metallicity of NGC 6397 of  ${\rm [Fe/H]} \sim -2.0$  (Jain et al. 2020). It is interesting to see stellar associations with NGC 6397 when the average metallicity of CDTG-36 does not compare to the metallicity of NGC 6397, and when both DS22a:DTG-55 and DS22b:DTG-9 are very metal-poor ( $\langle {\rm [Fe/H]} \rangle \sim -2.5$  and  $\langle {\rm [Fe/H]} \rangle \sim -2.5$ , respectively) (Shank et al. 2022a, 2022b). There are four associations between CDTG-36 and previous groups, with all four not being assigned to large-scale substructure by the previous authors, though two are associated with the globular cluster NGC 6397. CDTG-36 has two member stars that are very metal-poor, while the other three are just metal-poor, which may explain the discrepancy in the metallicity observed between CDTG-36 and NGC 6397.

#### 4.3. Globular Clusters and Dwarf Galaxies

Both globular clusters and dwarf galaxies have been shown to play an important role in the formation of stars that deviate from the usual chemical-abundance trends in the MW (Ji et al. 2016; Myeong et al. 2018c). Globular clusters can also be a good indicator of galaxy-formation history based on their metallicities and orbits (Woody & Schlaufman 2021). From the work of Vasiliev & Baumgardt (2021), we can compare the dynamical properties of 170 globular clusters to those of the CDTGs we identify. The procedure that is employed is the same one used for previously identified groups and stellar associations introduced in Section 4.2. The dynamics for 45 dwarf galaxies of the MW (excluding the Large Magellanic Cloud, Small Magellanic Cloud, and Sagittarius) are also explored (McConnachie & Venn 2020; Li et al. 2021). Shank et al. (2022b) provide details of the orbits of the globular clusters and dwarf galaxies. The same procedure used for previously identified groups was then applied to determine whether a CDTG was dynamically associated with the dwarf galaxy. Stellar associations were also determined for both globular clusters and dwarf galaxies in the same manner as used for previously identified groups.

The above comparison exercise led to seven of our identified CDTGs being associated with globular clusters. Table 6 provides a breakdown of which globular clusters are associated with our CDTGs. The CDTGs associated with globular clusters are expected to have formed in chemically similar birth environments; this is mostly supported through the similar chemical properties of the CDTGs. Associations of globular clusters with Galactic substructure have also been made by Massari et al. (2019) and Callingham et al. (2022).

Ryu 879 (RLGC 2) (CDTG-8 and CDTG-20), IC 1257 (CDTG-15), NGC 6293 (CDTG-11), and NGC 6402 (M14) (CDTG-11) are dynamically associated with their respective groups. On the other hand, NGC 362 (CDTG-28), NGC 4833 (CDTG-2), NGC 5986 (CDTG-11), and NGC 6397 (CDTG-36) have stellar associations with their respective groups. Even though the matched stars in these globular clusters would have individually been associated with the globular cluster orbital parameters, the overall CDTG did not possess sufficiently similar orbital characteristics to be associated.

1. Ryu 879 (RLGC 2) has two dynamical CDTG associations that agree with each other in mean metallicity within errors ( $\langle [Fe/H] \rangle \sim -1.97 \pm 0.8$  for CDTG-9 versus  $\langle [Fe/H] \rangle \sim -1.05 \pm 0.16$  for CDTG-20), compared to the metallicity of Ryu 879 (RLGC 2) of [Fe/H]  $-2.1 \pm 0.3$ 

(Ryu & Lee 2018). Both CDTG-9 and CDTG-20 are associated with GSE in this work, agreeing with the association to the Galactic substructure of Ryu 879 (RLGC 2) by Callingham et al. (2022), while Massari et al. (2019) did not analyze Ryu 879 (RLGC 2), since the globular cluster was only recently discovered at the time of the publication.

- 2. IC 1257 is associated with GSE in this work, and Massari et al. (2019); Callingham et al. (2022), and Limberg et al. (2022) associate IC 1257 with GSE as well.
- 3. NGC 6293 is associated with the bulge by both Massari et al. (2019) and Callingham et al. (2022), though this globular cluster is associated with GSE in this work. CDTG-11, which is associated with NGC 6293, interestingly has the lowest bound orbital energy ( $\langle E \rangle \sim -2.2$ ), which actually overlaps with the potential energy of the defined bulge region in Callingham et al. (2022), but here CDTG-11 is assigned to GSE due to the large eccentricity ( $\langle ecc \rangle \sim 0.75$ ). It is possible that this group formed in the bulge with intrinsically large eccentricity.
- NGC 6402 (M14) is associated with GSE in this work, but is not associated in Massari et al. (2019). Callingham et al. (2022) associate NGC 6402 (M14) with the Kraken substructure, not explored in this work.
- 5. NGC 362 is not associated with an MW substructure in this work, but was associated with GSE by Massari et al. (2019); Callingham et al. (2022), and Limberg et al. (2022). CDTG-28, which was associated with NGC 362, does not have a sufficiently high eccentricity ( $\langle ecc \rangle \sim 0.5$ ) in this work to be associated with GSE.
- 6. NGC 4833 is associated with GSE by both the identification in this work and Massari et al. (2019), but related to the Kraken substructure, not explored in this work, by Callingham et al. (2022).
- NGC 5986 is associated with the Kraken substructure by Callingham et al. (2022), while not being assigned by Massari et al. (2019) and associated with GSE in this work.
- 8. NGC 6397 is not associated with any substructure in this work, but Massari et al. 2019 find an association with the disk, which is not a part of the substructure routine in this work, while Callingham et al. (2022) associate this globular cluster to the Kraken substructure, not explored in this work.

We did not identify any associations of CDTGs to the sample of (surviving) MW dwarf galaxies, either through stellar associations, or through the dynamical association procedure described above. Note that we excluded known RPE stars that are members of recognized dwarf galaxies during the assembly of our field-star sample. As dwarf galaxy astrometric parameters themselves continue to improve, evidence may arise that shows some stripped stars after the dwarf has made a pass near the inner MW, but that is currently not seen in this sample. Nevertheless, some of the CDTGs identified by our analysis may well be associated with dwarf galaxies that have previously merged with the MW, and are now disrupted.

## 5. Chemical Structure of Identified CDTGs

#### 5.1. Statistical Framework

Since the CDTGs we have obtained are expected to contain stars that (within each given CDTG) have been formed in similar primordial environments, the same processes may be responsible for their chemical enrichment. In this section, we explore whether the elemental abundances of stars within the found CDTGs are more similar to each other than when the stars are randomly selected from the RPE final sample.

We follow the same statistical framework as outlined in Gudin et al. (2021). First, we use Monte Carlo sampling to select  $2.5 \times 10^6$  random groups of N stars with a given measured elemental abundance (with  $5 \le N \le 22$ ) from the sample and measure the biweight scale (Beers et al. 1990). This allows us to obtain empirical estimates of the cumulative distribution functions (CDFs) for the elemental-abundance dispersions within CDTGs of a given size. A low CDF value for a given elemental-abundance dispersion in a given CDTG indicates increased similarity for this species between the cluster member stars.

For the elemental-abundance dispersions selected at random for CDTGs of a given size, the probability of the number of clusters lying below a given CDF value (from 0–1) is described by the binomial distribution. Using three different CDF thresholds ( $\alpha \in \{0.25, 0.33, 0.5\}$ ) and multiple different abundances ( $X \in \{[Fe/H], [C/Fe]_{c,...}\}$ ), we obtain overall statistical significances from multinomial distributions obtained by either grouping the cumulative probabilities across all  $\alpha$  values, or across all X abundances. The overall statistical significance of the results is obtained by grouping the probabilities across both all  $\alpha$  values and all X abundances. We denote these probabilities according to the following classifications:

- 1. Individual elemental-abundance dispersion (IEAD) probability: Individual binomial probability for specific values of  $\alpha$  and X.
- 2. Full elemental-abundance distribution (FEAD) probability: Multinomial probability for specific values of  $\alpha$ , grouped over all abundances X.
- 3. Global elemental-abundance dispersion (GEAD) probability: Multinomial probability for specific abundances X, grouped over all values of  $\alpha$ . This is the overall statistical significance for the particular abundance.
- 4. Overall elemental-abundance dispersion (OEAD) probability: Multinomial probability grouped over all values of  $\alpha$  and all abundances X. This is the overall statistical significance of our clustering results.

For a more detailed discussion of the above probabilities, and their use, the interested reader is referred to Gudin et al. (2021).

#### 5.2. Important Caveats

Note that there are several caveats to the interpretation of this scheme that should be mentioned. Most importantly, a meaningful understanding of the derived probabilities (described below) depends on the contrast of the *typical* CDTG elemental-abundance dispersion to the abundance dispersion of the parent population to which it is compared, from which random draws are made. If the typical CDTG elemental-abundance dispersion is roughly commensurate with the dispersion of the parent sample, then by definition the dispersions will always be consistent with what are expected from the random draws, and one cannot expect the CDTG elemental-abundance dispersions to be significantly smaller. This requires that, in particular for a given element, prior to

assessing the significance of its dispersion for a given set of CDTGs, we should compare its value to the expected value from the appropriate parent sample. We carry out this exercise, as described below, by inspection of the interquartile range (IQR) for each element for a given set of CDTGs compared to the IQR of CDTGs drawn at random from the parent sample. As a rule of thumb, we demand that the IQR of the mean for each element of a set of CDTGs is on the order of one-half of the IQR of the parent-population CDTGs. Otherwise, there is insufficient *dynamical range* for the statistical inferences to be made with confidence, at least for individual elements.

Furthermore, as is perhaps obvious, the statistical power of our comparisons increases with the number of CDTGs in a given parent population. Thus, when we consider dynamical clusters formed exclusively from r-II stars, as discussed below, it becomes more difficult to place confidence in the statistical inferences. For that reason, in the case of the clustering of r-II stars, we have relaxed the criterion for the minimum number of stars per cluster to three, rather than five, more than doubling the number of identified r-II CDTGs.

It should also be kept in mind that the observed CDTG elemental-abundance dispersions depend on a number of different parameters, including not only on the total mass of a given parent dwarf galaxy, but on its available gas mass for conversion into stars, the history of star formation in that environment, and the nature of the progenitor population(s) involved in the production of a given element. These are complex and interacting sets of conditions, and certainly are best considered in the context of simulations (such as in Hirai et al. 2022). Consequently, the expected result for a given element in a given set of CDTGs is not always clear. However, we have designed our statistical tests to consider a broad set of questions of interest, the most pertinent of which for the current application are the FEAD and OEAD probabilities, which we employ for making our primary inferences.

#### 5.3. Results

# 5.3.1. Full Sample of RPE CDTGs

Table 8 lists the means and dispersions of the elemental abundances explored in this study for each of the CDTGs identified in this work. The second part of the table lists the global CDTG properties, with the mean and standard error of the mean (using biweight location and scale) of both the CDTG means and dispersions being listed. The second part of the table also includes the IQR of the CDTG means and dispersions. The third part of the table lists the biweight location and scale of the elemental abundances in the final sample, along with the IQR of the elemental abundances in the final sample. As can be seen by comparing the two IQRs for each of the CDTG results and the final sample, the IQRs for the CDTG results for four of the seven elements considered are at least twice smaller, the exceptions being for [Fe/H] (which only slightly misses our rule of thumb), [Sr/Fe], and [Y/Fe]. The elements that meet the criteria, [C/Fe]<sub>c</sub>, [Mg/Fe], [Ba/Fe], and [Eu/Fe], provide stronger constraints compared to the ones that have large IQR ranges.

Table 9 lists the number of CDTGs with available estimates of the listed abundance ratios, and the number of CDTGs falling below the 0.50, 0.33, and 0.25 levels of the CDFs, along with our calculated values for the various probabilities. The full and overall probabilities (captured by the FEAD and OEAD

probability values) are very low, implying that the measured abundance spreads are highly statistically significant within our CDTGs across the entire sample; this is similar to the results found in Gudin et al. (2021) (see their Table 7). However, some of the individual abundance spreads (the GEAD probabilities) are not statistically significant, namely, the [Mg/Fe] and [Sr/Fe] spreads. Keep in mind, as noted above, that the lack of contrast in the mean IQRs of [Fe/H], [Sr/Fe], and [Y/Fe] for our CDTGs with their corresponding mean IQRs for the full sample may impact the interpretation of their probabilities.

By comparison, in Gudin et al. (2021), the [Fe/H], [C/Fe]<sub>c</sub>, [Sr/Fe], and [Ba/Fe] spreads were statistically significant, as inferred from their GEAD probabilities; the same is recovered in this study, with the exception of [Sr/Fe]. It should also be recalled that the sample of RPE stars considered by Gudin et al. is dominated by stars with lower [Fe/H] than our present sample, since the generally more metal-rich stars from GALAH were not available at that time.

Below we explore whether *r*-I and *r*-II stars exhibit different elemental-abundance patterns. For this purpose, we repeat the clustering procedure described in Section 3, separately for subsets of *r*-I and *r*-II stars. The result of this procedure is 28 (*r*-I) CDTGs ranging in size from five to 18 members and 20 (*r*-II) CDTGs ranging in size from three to 23 members, respectively. We then perform the same statistical analysis on each as described above.

# 5.3.2. The r-I Sample

The binomial statistics for the 28 *r*-I CDTGs are listed in Table 10. We observe a lack of statistical significance for the reduction of [Sr/Fe] and [Eu/Fe] abundance spreads, but other abundances (including [Mg/Fe], which exhibited a statistically insignificant spread reduction in the case of the full sample) exhibit statistically significant reductions in their spreads (all elements except for [Sr/Fe] and [Eu/Fe] have GEAD probabilities of less than 10%).

From the inspection of Table 17 in the Appendix, it can be seen that only three of the seven elements considered ([Y/Fe], [Ba/Fe], and [Eu/Fe]) have contrasts in their mean CDTG IQRs relative to the mean IQRs of the full sample of r-I stars that pass our factor of 2 rule of thumb (although [Fe/H] and  $[C/Fe]_c$  only narrowly miss), so interpretation of the GEAD probabilities for several of these elements should be regarded with caution.

The FEAD probabilities for the r-I CDTGs are low, and are statistically significant for all three of the v = 0.5, v = 0.33, and v = 0.25 levels. The OEAD probability is highly statistically significant.

## 5.3.3. The r-II Sample

If we adopt the minimum number of stars per r-II CDTG for the clustering exercise as we have for the full sample (five) and the r-I sample (five), we are left with only a total of seven r-II CDTGs for the statistical analysis. We judge this to be too small, as experience suggests that a minimum of 10 CDTGs provide the most stable results. Thus, we chose to reduce the minimum number of stars in order to form an r-II CDTG from five to three. This increases the number of r-II CDTGs from seven to 20, comparable to that in the full and the r-I samples (36 and 28, respectively).

Table 8
CDTG Abundance Means, Dispersions, and IQRs

Cluster	N Stars	(Fe/H)	(C/Fe) <sub>c</sub>	(Mg/Fe)	(Sr/Fe)	(Y/Fe)	(Ba/Fe)	(Eu/Fe)
CDTG-1	22	$-1.00 \pm 0.20$	$+0.52 \pm 0.06$		+0.64 ±	$+0.24 \pm 0.20$	$+0.32 \pm 0.20$	$+0.51 \pm 0.10$
CDTG-2	21	$-1.33 \pm 0.75$	$+0.30 \pm 0.23$	$+0.35 \pm 0.20$	$+0.15 \pm 0.35$	$+0.11 \pm 0.25$	$+0.26 \pm 0.15$	$+0.57 \pm 0.17$
CDTG-3	18	$-0.87 \pm 0.07$	$+0.47 \pm 0.06$		$+0.95\pm$	$+0.11 \pm 0.14$	$+0.13 \pm 0.19$	$+0.49 \pm 0.09$
CDTG-4	18	$-1.52 \pm 0.57$	$+0.29 \pm 0.20$	$+0.24 \pm 0.21$	$+0.13 \pm 0.07$	$+0.06 \pm 0.18$	$+0.26 \pm 0.27$	$+0.51 \pm 0.15$
CDTG-5	17	$-1.28 \pm 0.47$	$+0.38 \pm 0.17$	$+0.32\pm$	$+0.24 \pm 0.07$	$+0.22 \pm 0.20$	$+0.37 \pm 0.26$	$+0.62 \pm 0.16$
CDTG-6	16	$-0.86\pm0.05$	$+0.49 \pm 0.13$	$+0.45\pm$	$+0.28 \pm 0.63$	$+0.08 \pm 0.17$	$+0.11 \pm 0.11$	$+0.44 \pm 0.09$
CDTG-7	16	$-1.89 \pm 0.76$	$+0.53 \pm 0.19$	$+0.44 \pm 0.13$	$+0.31 \pm 0.79$	$+0.03 \pm 0.19$	$+0.14 \pm 0.28$	$+0.55 \pm 0.18$
CDTG-8	14	$-1.62 \pm 0.78$	$+0.47 \pm 0.22$	$+0.37 \pm 0.03$	$+0.30 \pm 0.27$	$+0.26 \pm 0.18$	$+0.33 \pm 0.41$	$+0.71 \pm 0.29$
CDTG-9	12	$-0.88 \pm 0.09$	$+0.50 \pm 0.06$	$+0.44\pm$	$+1.44 \pm 0.00$	$+0.18 \pm 0.15$	$+0.17 \pm 0.21$	$+0.57 \pm 0.26$
CDTG-10	12	$-0.85 \pm 0.02$	$+0.46 \pm 0.08$	•••	$+1.59 \pm$	$+0.14 \pm 0.16$	$+0.18 \pm 0.20$	$+0.51 \pm 0.10$
CDTG-11	11	$-1.49 \pm 0.19$	$+0.54 \pm 0.10$	$+0.42 \pm 0.04$	$-0.29\pm$	$+0.24 \pm 0.09$	$+0.29 \pm 0.22$	$+0.49 \pm 0.13$
CDTG-12	11	$-2.16\pm0.81$	$+0.53 \pm 0.35$	$+0.38 \pm 0.16$	$+0.12 \pm 0.12$	$-0.02 \pm 0.31$	$+0.02 \pm 0.41$	$+0.58 \pm 0.16$
CDTG-13	11	$-0.86 \pm 0.04$	$+0.49 \pm 0.07$	•••	$+1.13 \pm$	$+0.15 \pm 0.20$	$+0.15 \pm 0.10$	$+0.52 \pm 0.10$
CDTG-14	11	$-0.91 \pm 0.14$	$+0.51 \pm 0.09$	•••	$+1.42\pm$	$+0.22 \pm 0.17$	$+0.25 \pm 0.20$	$+0.49 \pm 0.08$
CDTG-15	10	$-1.29 \pm 0.22$	$+0.41 \pm 0.11$	$+0.31 \pm$	$+1.68\pm$	$+0.09 \pm 0.07$	$+0.39 \pm 0.23$	$+0.64 \pm 0.14$
CDTG-16	10	$-0.91 \pm 0.14$	$+0.45 \pm 0.10$		$+0.35\pm$	$+0.15 \pm 0.13$	$+0.25 \pm 0.22$	$+0.55 \pm 0.08$
CDTG-17	10	$-1.99 \pm 0.54$	$+0.20 \pm 0.37$	$+0.33 \pm 0.08$	$+0.08 \pm 0.33$	$-0.18 \pm 0.17$	$-0.01 \pm 0.25$	$+0.47 \pm 0.15$
CDTG-18	9	$-2.31 \pm 0.70$	$+0.39 \pm 0.22$	$+0.35 \pm 0.20$	$+0.06 \pm 0.32$	$+0.15 \pm 0.12$	$+0.25 \pm 0.27$	$+0.73 \pm 0.29$
CDTG-19	9	$-1.40 \pm 0.36$	$+0.37 \pm 0.26$	$+0.37 \pm$	$+0.30 \pm 0.05$	$-0.02 \pm 0.36$	$+0.38 \pm 0.21$	$+0.68 \pm 0.26$
CDTG-20	9	$-1.16 \pm 0.44$	$+0.37 \pm 0.09$		$+0.08 \pm$	$+0.19 \pm 0.20$	$+0.41 \pm 0.25$	$+0.64 \pm 0.13$
CDTG-21	9	$-0.98 \pm 0.31$	$+0.41 \pm 0.10$		$+0.90 \pm$	$+0.11 \pm 0.16$	$+0.25 \pm 0.26$	$+0.55 \pm 0.13$
CDTG-22	8	$-2.06 \pm 0.60$	$+0.40 \pm 0.33$	$+0.54 \pm 0.17$	$-0.05 \pm 0.23$	$-0.02 \pm 0.22$	$+0.11 \pm 0.24$	$+0.48 \pm 0.22$
CDTG-23	8	$-0.89 \pm 0.09$	$+0.47 \pm 0.19$	$+0.48\pm$	$+0.31 \pm 0.84$	$-0.05 \pm 0.17$	$+0.08 \pm 0.32$	$+0.48 \pm 0.13$
CDTG-24	8	$-0.97 \pm 0.28$	$+0.52 \pm 0.09$	$+0.35 \pm$	$+0.37 \pm$	$+0.26 \pm 0.18$	$+0.26 \pm 0.28$	$+0.51 \pm 0.11$
CDTG-25	8	$-2.20 \pm 0.52$	$+0.18 \pm 0.38$	$+0.30 \pm 0.40$	$+0.03 \pm 0.14$	$-0.25 \pm 0.07$	$+0.06 \pm 0.30$	$+0.49 \pm 0.10$
CDTG-26	7	$-0.84 \pm 0.10$	$+0.41 \pm 0.02$	•••		$+0.21 \pm 0.12$	$+0.33 \pm 0.16$	$+0.48 \pm 0.05$
CDTG-27	7	$-2.03 \pm 0.65$	$+0.55 \pm 0.26$	$+0.49 \pm$	$+0.15\pm$	$+0.11 \pm 0.30$	$+0.25 \pm 0.33$	$+0.38 \pm 0.05$
CDTG-28	7	$-1.31 \pm 0.52$	$+0.47 \pm 0.20$	$+0.52 \pm 0.15$	$+0.15 \pm 0.41$	$+0.02 \pm 0.23$	$+0.22 \pm 0.18$	$+0.58 \pm 0.17$
CDTG-29	6	$-0.90 \pm 0.09$	$+0.42 \pm 0.08$			$+0.06 \pm 0.17$	$+0.11 \pm 0.10$	$+0.56 \pm 0.12$
CDTG-30	6	$-0.89 \pm 0.07$	$+0.43 \pm 0.04$	$+0.11\pm$	$+0.32\pm$	$-0.02 \pm 0.17$	$+0.10 \pm 0.16$	$+0.53 \pm 0.16$
CDTG-31	6	$-0.92 \pm 0.06$	$+0.47 \pm 0.04$		•••	$-0.03 \pm 0.11$	$+0.13 \pm 0.08$	$+0.48 \pm 0.09$
CDTG-32	6	$-0.86 \pm 0.03$	$+0.44 \pm 0.22$	$+0.32 \pm$	$-0.32 \pm 0.35$	$+0.24 \pm 0.16$	$+0.11 \pm 0.17$	$+0.43 \pm 0.06$
CDTG-33	6	$-1.87 \pm 0.61$	$+0.34 \pm 0.23$	$+0.31 \pm 0.13$	$+0.19 \pm 0.04$	$+0.01 \pm 0.32$	$+0.18 \pm 0.41$	$+0.63 \pm 0.15$
CDTG-34	6	$-1.25 \pm 0.60$	$+0.36 \pm 0.17$	$+0.40 \pm$	$-0.03 \pm$	$-0.02 \pm 0.21$	$+0.49 \pm 0.04$	$+0.62 \pm 0.06$
CDTG-35	5	$-0.91 \pm 0.15$	$+0.47 \pm 0.11$			$+0.16 \pm 0.29$	$+0.08 \pm 0.30$	$+0.56 \pm 0.08$
CDTG-36	5	$-0.91\pm0.09$	$+0.53 \pm 0.05$	•••	$+0.13\pm$	$-0.01 \pm 0.12$	$+0.08 \pm 0.12$	$+0.53 \pm 0.13$
Biweight (CDTG mean)		$-1.11 \pm 0.08$	$+0.45 \pm 0.01$	$+0.38 \pm 0.02$	$+0.20 \pm 0.06$	$+0.10 \pm 0.02$	$+0.20 \pm 0.02$	$+0.53 \pm 0.01$
Biweight (CDTG std)		$+0.31 \pm 0.05$	$+0.14 \pm 0.02$	$+0.14 \pm 0.02$	$+0.26\pm0.06$	$+0.17 \pm 0.01$	$+0.22\pm0.01$	$+0.13 \pm 0.01$
IQR (CDTG mean)		0.65	0.11	0.12	0.33	0.20	0.16	0.09
IQR (CDTG std)		0.49	0.14	0.08	0.28	0.06	0.11	0.07
Biweight (final)		$-1.27 \pm 0.68$	$+0.45 \pm 0.19$	$+0.37 \pm 0.20$	$+0.14 \pm 0.38$	$+0.10 \pm 0.21$	$+0.23 \pm 0.28$	$+0.55 \pm 0.16$
IQR (final)		1.08	0.22	0.24	0.40	0.28	0.36	0.21

Note. The first section of the table lists the biweight location and scale of the abundances for each of the CDTGs. The second section of the table lists the mean and the standard error of the mean (using biweight estimates) for both the location and scale of the abundances of the CDTGs, along with the IQR of the abundances of the CDTGs. The third section of the table lists the biweight location and scale of the final sample for each of the abundances, along with the IQR for each of the abundances in the final sample. The IQR lines are bolded to draw attention to the CDTG elemental-abundance mean IQRs to compare to the final sample abundance IQRs.

(This table is available in machine-readable form.)

Table 11 shows the binomial statistics for our 20 *r*-II CDTGs. From inspection, the GEAD probabilities for the elements considered are statistically significant in the same manner as the final sample, with [Mg/Fe] and [Sr/Fe] both lacking statistical significance.

From an inspection of Table 20 in the Appendix, it can be seen that only two of the seven elements considered ([Y/Fe] and [Ba/Fe]) have mean IQRs for the r-II CDTGs that are at least twice smaller than the mean IQR of the final sample, although  $[C/Fe]_c$  only narrowly misses our rule of thumb. Thus, we can assume that, for many of the individual elements,

there is not a useful dynamical range for confident interpretation for most of the GEADs.

The FEAD probabilities for the *r*-II CDTGs are statistically significant for all three v = 0.50, v = 0.33, and v = 0.25 levels. The OEAD probability is highly statistically significant.

#### 6. Summary

We have assembled an RPE initial sample of 1776 stars (1393 *r*-I stars, 381 *r*-II stars, and two *r*-III stars) from both a literature search and GALAH DR3 (Buder et al. 2021) survey data, with stars that met the *r*-process-enhancement

 Table 9

 CDTG Elemental-abundance Statistics: Final Sample

Abundance	# CDTGs	N < 0.5, 0.33, 0.25	IEAD Probabilities	GEAD Probabilities	OEAD Probability
[Fe/H]	36	24, 20, 18	3.3%, 0.4%, 0.1%,	0.1%	
$[C/Fe]_c$	36	21, 16, 15	20.3%, 10.1%, 2.1%,	1.6%	
[Mg/Fe]	12	5, 3, 2	80.6%, 81.2%, 84.2%,	69.1%	
[Sr/Fe]	17	9, 6, 6	50.0%, 51.1%, 23.5%,	19.7%	≪0.01%
[Y/Fe]	36	23, 13, 10	6.6%, 40.6%, 41.2%,	5.3%	
[Ba/Fe]	36	21, 17, 16	20.3%, 5.3%, 0.9%,	0.7%	
[Eu/Fe]	36	22, 16, 14	12.1%, 10.1%, 4.6%,	2.3%	
FEAD probabiliti	ies		0.09%, 0.01%, «0.01%		

**Note.** The IEAD probabilities represent the binomial probabilities for each element for the 0.5, 0.33, and 0.25 levels, respectively. The FEAD probabilities represent the probabilities (across *all* elements) for the 0.5, 0.33, and 0.25 levels, respectively. The GEAD probabilities represent the probabilities for the triplet of CDF levels for each element. The OEAD probability represents the probability (across *all* elements) resulting from random draws from the full CDF. See the text for details.

 Table 10

 CDTG Elemental-abundance Statistics: r-I Sample

Abundance	# CDTGs	<i>N</i> < 0.5, 0.33, 0.25	IEAD Probabilities	GEAD Probabilities	OEAD Probability
[Fe/H]	28	16, 14, 13	28.6%, 4.6%, 1.1%,	1.0%	
$[C/Fe]_c$	28	15, 14, 14	42.5%, 4.6%, 0.4%,	0.4%	
[Mg/Fe]	8	6, 5, 4	14.5%, 8.5%, 11.4%,	4.1%	
[Sr/Fe]	12	5, 5, 5	80.6%, 35.9%, 15.8%,	15.8%	≪0.01%
[Y/Fe]	27	19, 12, 9	2.6%, 14.5%, 21.4%,	1.6%	
[Ba/Fe]	28	19, 14, 12	4.4%, 4.6%, 2.9%,	0.8%	
[Eu/Fe]	28	15, 12, 9	42.5%, 18.1%, 25.0%,	12.6%	
FEAD probabilit	ies		$0.14\%, \ll 0.01\%, \ll 0.01\%$		

**Note.** The IEAD probabilities represent the binomial probabilities for each element for 0.5, 0.33, and 0.25 levels, respectively. The FEAD probabilities represent the probabilities (across *all* elements) for the 0.5, 0.33, and 0.25 levels, respectively. The GEAD probabilities represent the probabilities for the triplet of CDF levels for each element. The OEAD probability represents the probability (across *all* elements) resulting from random draws from the full CDF. See text for details.

 Table 11

 CDTG Elemental-abundance Statistics: r-II Sample

Abundance	# CDTGs	<i>N</i> < 0.5, 0.33, 0.25	IEAD Probabilities	GEAD Probabilities	OEAD Probability
[Fe/H]	20	16, 14, 11	0.6%, 0.1%, 0.4%,	0.0%	
$[C/Fe]_c$	19	13, 11, 9	8.4%, 2.2%, 2.9%,	0.9%	
[Mg/Fe]	5	2, 1, 1	81.2%, 86.5%, 76.3%,	68.5%	
[Sr/Fe]	10	5, 3, 3	62.3%, 69.3%, 47.4%,	39.6%	≪0.01%
[Y/Fe]	17	11, 7, 6	16.6%, 31.5%, 23.5%,	9.0%	
[Ba/Fe]	20	12, 10, 5	25.2%, 8.7%, 58.5%,	7.2%	
[Eu/Fe]	20	12, 9, 8	25.2%, 18.2%, 10.2%,	6.5%	
FEAD probabiliti	ies		$0.06\%, \ll 0.01\%, 0.03\%$		

**Note.** The IEAD probabilities represent the binomial probabilities for each element for the 0.5, 0.33, and 0.25 levels, respectively. The FEAD probabilities represent the probabilities (across *all* elements) for the 0.5, 0.33, and 0.25 levels, respectively. The GEAD probabilities represent the probabilities for the triplet of CDF levels for each element. The OEAD probability represents the probability (across *all* elements) resulting from random draws from the full CDF. See the text for details.

requirements listed in Table 1. A total of 105 of these stars are identified as CEMP-*r* stars; these are listed in Table 14 in the Appendix. These stars are of interest due to their enhanced carbon abundance and association with the morphological groups described in Yoon et al. (2016). Based on their classification scheme, there are 58 Group I CEMP-*r* stars, 41 Group II CEMP-*r* stars, and two Group III CEMP-*r* stars, with a number of stars that have ambiguous classifications. This list provides a useful reference for high-resolution follow-up targets, some of which have already begun (e.g., Rasmussen et al. 2020; Zepeda et al. 2022).

The RPE final sample of 1720 stars (1346 *r*-I stars, 372 *r*-II stars, and two *r*-III stars) had RV and astrometric information from which orbits were constructed, in order to identify CDTGs in orbital energy and cylindrical action space with the HDBSCAN algorithm. We chose HDBSCAN as the clustering algorithm due to precedence within the literature (Koppelman et al. 2019b; Limberg et al. 2021b; Gudin et al. 2021; Shank et al. 2022b), and its ability to extract clusters of stars over the energy and action space.

We recover 36 CDTGs that include between five and 22 members, with 17 CDTGs containing at least 10 member stars.

These CDTGs were associated with MW substructures, resulting in the reidentification of the GSE, SD, MWTD, HS, LMS-1 (Wukong), and Thamnos. A total of seven CDTGs were associated with globular clusters, while no surviving dwarf galaxies were determined to be associated with the identified CDTGs. Previously identified groups were found to be associated with the CDTGs as well, with past work mostly confirming our substructure identification, and showing some limitations in the procedure, which we discussed. Each of these associations allows insights into the dynamical and chemical properties of the parent substructures.

The implications of past group and stellar associations were explored, with emphasis placed on the structure associations. Stellar associations to stars with abnormal MW abundances were addressed as being good candidates for high-resolution follow-up spectroscopy targets, due to the statistical likelihood of the other members being chemically peculiar as well, mostly focused on RPE and CEMP stars.

We have considered the statistical significance of the elemental-abundance dispersions across the identified RPE CDTGs for a set of seven abundance ratios ([Fe/H]], [C/Fe]<sub>c</sub>, [Mg/Fe], [Sr/Fe], [Y/Fe], [Ba/Fe], and [Eu/Fe]). CDTGs are statistically examined, in order to assess the similarity (or not) of the chemical-evolution histories in their presumed dwarfgalaxy birth environments, following the approach developed by Gudin et al. (2021). We point out that, for a number of elements considered, the mean IQRs of the dispersions in the CDTGs do not provide a sufficient dynamical range compared to the mean IQR of the parent samples with which they are compared (we suggest they must be a factor of 2 smaller) in order to enable meaningful interpretations of the GEAD probabilities.

However, the probabilities that consider the distributions of *all* of the elements across the CDFs for the set of CDTGs (the FEAD probabilities, and the OEAD probabilities), strongly support the assertion that the stars associated with individual RPE CDTGs indeed share similar chemical-enrichment histories, as previously claimed by Gudin et al. (2021). We have also divided the full sample into RPE stars classified as moderately *r*-process enhanced (*r*-I) and highly *r*-process enhanced (*r*-II), and find similar results.

The methods presented here will be used in future samples that contain many more RPE stars, especially with planned data releases from the RPA increasing their total number, and other ongoing or planned surveys allowing for a systematic search for RPE stars. The next steps in advancing our understanding of the birth environments and the nature of the astrophysical site(s) of the *r*-process require detailed comparisons with modern high-resolution (spatial and temporal) simulations of the formation of MW-like galaxies, along the lines explored by Hirai et al. (2022).

The authors are thankful to an anonymous referee, who provided comments and suggestions that substantially improved the presentation in this paper. We are grateful for data provided by Rohan Naidu that is included in this work. D.S., T.C.B., and I.U.R. acknowledge partial support for this work from grant PHY 14-30152; Physics Frontier Center/JINA Center for the Evolution of the Elements (JINA-CEE), awarded by the US National Science Foundation. The work of V.M.P. is supported by NOIRLab, which is managed by the Association of Universities for Research in Astronomy (AURA) under a cooperative agreement with the US National Science Foundation. I.U.R. acknowledges support from the NASA Astrophysics Data Analysis Program, grant 80NSSC21K0627, and the US National Science Foundation, through grant AST 1815403/1815767.

# **Appendix**

Here we present a table for the RPE initial sample (Table 12) and the RPE final sample (Table 13). In the print edition, only the table descriptions are provided; the full tables are available only in electronic form.

We also present Table 14, which describes the identified CEMP-r stars and their associated morphological groups, according to the regions defined by Yoon et al. (2016). Tables 15 and 16 show the CDTGs identified by HDBSCAN and the CDTG dynamical parameters as determined by AGAMA for the r-I sample, respectively. Table 17 lists the means and dispersions of the CDTGs identified in the r-I sample, along with the statistics on all the CDTGs and the r-I sample. Tables 18 and 19 show the CDTGs identified by HDBSCAN and the CDTG dynamical parameters as determined by AGAMA for the r-II sample, respectively. Table 20 lists the means and dispersions of the CDTGs identified in the r-II sample, along with the statistics on all the CDTGs and the r-II sample.

Table 12
Description of the Initial Sample from the RPE Sample

	Column	Field	Unit	Description
	1	Name	:	Name of the star as given by the reference
	2	Source ID	:	
	3	R.A.	(J2000)	R.A. of the star given in hours:minutes:second
	4	Decl.	(J2000)	Decl. of the star given in degrees:minutes:seconds
	5	$V_{ m mag}$	:	$V$ magnitude of the star as given by the $V_{ m mag}$ reference
	9	$G_{ m mag}$	:	Gaia G mean magnitude of the star as given by the Gaia source ID
	7	$G_{ m BP}-G_{ m RP}$	:	Gaia BP – RP color mean magnitude of the star as given by the Gaia source ID
	∞	$V_{ m mag}$ (Gaia)		V magnitude of the star as determined by the transformations from G mag to V mag using $V = G + 0.02704 - 0.01424^*$ (BP-RP) $+ 0.2156^*$ (BP-RP) <sup>2</sup> $-0.01426$ (BP-RP)
		i.	Í	EB-NRY given by Kielio et al. (2021)
	6	RV	$(\text{km s}^{-1})$	Radial velocity as given by the RV reference
	10	Error	$(\text{km s}^{-1})$	nce
	Ξ:	${ m RV}_{ m Gaia}$	$(\text{km s}^{-1})$	
	12	Error	$(km s^{-1})$	ia source ID
	13	Parallax	(mas)	aia source ID
	14	Error	(mas)	ource ID
	15	Distance	(kpc)	Inverse parallax distance (1/parallax)
	16	Error	(kpc)	Inverse parallax distance error (parallax <sub>error</sub> /(parallax <sup>2</sup> ))
	17	Distancecorrected	(kpc)	Corrected inverse parallax distance $(1/(parallax + 0.026))$ based on Huang et al. (2021)
	18	Error	(kpc)	Corrected inverse parallax distance error (parallax $\frac{1}{2}$ (parallax + 0.026) <sup>2</sup> )) based on Huang et al. (2021)
	19	Relative error	:	Relative error of the corrected distance as given by Gaia
	20	Distance BJ21	(kpc)	50th percentile distance as given by Bailer-Jones et al. (2021) based on the Gaia source ID
25	21	Error	(kpc)	50th percentile error estimated by the 84th percentile distance and the 16th percentile distance as given by Bailer-Jones et al. (2021) based on the Gaia source ID
τ .				$((\operatorname{dist84-dist16})/2)$
	22	Relative error	:	Relative error of the 50th percentile distance as given by Bailer-Jones et al. (2021) based on the Gaia source ID
	23	Distance StarHorse	(kpc)	50th percentile distance as given by Anders et al. (2022) based on the Gaia source ID
	24	Error	(kpc)	50th percentile error estimated by the 84th percentile distance and the 16th percentile distance as given by Anders et al. (2022) based on the Gaia source ID ((dist84-
				dist16)/2)
	25	Relative error	:	
	26	${ m PM_{RA}}$	$(\text{mas yr}^{-1})$	proper motion in the R.A. as given by the Gaia source ID
	27	Error	$(\text{mas yr}^{-1})$	Proper motion error in the R.A. as given by the Gaia source ID
	28	$PM_{DEC}$	$(\text{mas yr}^{-1})$	Proper motion in the decl. as given by the Gaia source ID
	29	Error	$(\text{mas yr}^{-1})$	Proper motion error in the decl. as given by the Gaia source ID
	30	Correlation	:	Correlation coefficient between the proper motion in R.A. and the proper motion in decl. as given by the Gaia source ID
		coefficient		
	31	$T_{ m eff}$	(K)	Effective temperature of the star as given by the reference
	32	$\log g$	(cgs)	Surface gravity of the star as given by the reference
	33	[Fe/H]	:	Metallicity of the star as given by (log ∉(Fe) – log ∉(Fe) <sub>☉</sub> ) (solar value of 7.50 taken from Asplund et al. 2009)
	34	$\log \epsilon(\text{Fe})$	:	Logarithmic iron abundance of the star as given by the reference
	35	[C/Fe]	:	Carbon abundance ratio of the star as given by ( $\log \epsilon(C) - \log \epsilon(C)_{\odot} - [Fe/H]$ ) (solar value of 8.43 taken from Asplund et al. 2009)
	36	log ∈(C)	:	Logarithmic carbon abundance of the star as given by the reference
	37	$[C/Fe]_c$	:	Carbon abundance ratio corrected for evolutionary effects from Placco et al. (2014b)
	38	$AC_c$	:	Absolute carbon corrected for evolutionary effects from Placco et al. $(2014b)$ ( $[C/Fe]_c + [Fe/H] + \log \epsilon(C)_\odot)$ (solar value of 8.43 taken from Asplund et al. 2009)
	39	CARDET	:	Flag with "D" if the carbon abundance ratio ([C/Fe]) is detected by reference and "U" if an upper limit by the reference and "L" if a lower limit by the reference and
	40	CFMP	:	"X" if none is detected by the reference  Flav as "C" for CFMP if $IC/Fe1 > + 0.7$ and "I" for CFMP-intermediate if $+0.5c < +0.7$ and "N" for carbon-normal if $IC/Fe1 < +0.5$ and "X" if there is no
	P	CEAN		
	41	$[{ m Mg/Fe}]$	:	Magnesium abundance ratio of the star as given by (log ε(Mg) – log ε(Mg) <sub>☉</sub> – [Fe/H]) (solar value of 7.60 taken from Asplund et al. 2009)

Table 12 (Continued)

Column	Field	Unit	Description
42	log ∈(Mg)	:	Logarithmic magnesium abundance of the star as given by the reference
43	MAGDET	:	Flag with "D" if the magnesium abundance ratio ([Mg/Fe]) is detected by the reference and "U" if an upper limit by the reference and "L" if a lower limit by the reference and "X" if none is detected by the reference
-	. G. (E.)		Conversion of a month of a conversion of a month of a conversion of a conversi
4	[Sr/ Fe]	:	Strontium abundance ratio of the star as given by ( $\log \epsilon(Sr) - \log \epsilon(Sr) = 1 + \epsilon/H$ )) (solar value of 2.8/ taken from Asplund et al. 2009)
45	$\log \epsilon(Sr)$	:	Logarithmic strontium abundance of the star as given by the reference
46	STRDET	:	Flag with "D" if the strontium abundance ratio ([Sr/Fe]) is detected by the reference and "U" if an upper limit by the reference and "L" if a lower limit by the reference
			and "X" if none is detected by the reference
47	[Y/Fe]	:	Yttrium abundance ratio of the star as given by $(\log \epsilon(Y) - \log \epsilon(Y)) - (Fe/H)$ (solar value of 2.21 taken from Asplund et al. 2009)
48	$\log \epsilon(Y)$	:	Logarithmic yttrium abundance of the star as given by the reference
49	YTTDET	:	Flag with "D" if the yttrium abundance ratio ([Y/Fe]) is detected by the reference and "U" if an upper limit by the reference and "L" if a lower limit by the reference
			and "X" if none is detected by the reference
50	[Ba/Fe]	:	Barium abundance ratio of the star as given by (log ε(Ba) – log ε(Ba) <sub>o</sub> –– [Fe/H]) (solar value of 2.18 taken from Asplund et al. 2009)
51	$\log \epsilon(Ba)$	:	Logarithmic barium abundance of the star as given by the reference
52	BARDET	:	Flag with "D" if the barium abundance ratio ([Ba/Fe]) is detected by the reference and "U" if an upper limit is detected by the reference and "L" if a lower limit is
			detected by the reference and "X" if none is detected by the reference
53	[Eu/Fe]	:	Europium abundance ratio of the star as given by (log ε(Eu) – log ε(Eu) <sub>☉</sub> – [Fe/H]) (solar value of 0.52 taken from Asplund et al. 2009)
54	log ϵ(Eu)	:	Logarithmic europium abundance of the star as given by the reference
55	EURDET	:	Flag with "D" if the europium abundance ratio ([Eu/Fe]) is detected by the reference and "U" if an upper limit by the reference and "L" if a lower limit by the
			reference and "X" if none is detected by the reference
99	Class	:	Class for the star, as given in Table 1
57	S/N	:	Average signal-to-noise ratio of the spectrum as given by the reference
58	Reference	:	Reference for the star
59	$V_{ m mag}$ reference	:	Reference for the $V$ magnitude of the star
09	Distance AGAMA	:	Reference for the distance used in AGAMA (StarHorse prioritized over BJ21 unless the StarHorse distance has a relative error greater than 0.3, and if both have a
			relative error greater than 0.3 we adopt no distance estimate)
61	RV reference	:	Reference for the RV

(This table is available in its entirety in machine-readable form.)

Table 13
Description of the Final Sample from the RPE Sample

[ე	Column Field	IInit	Description
3			
-	Name	:	reference
7	Source ID	:	Gaia EDR3 Source ID of the star
3	R.A.	(J2000)	R.A. of the star given in hours:minutes:seconds
4	Decl.	(J2000)	Decl. of the star given in degrees:minutes:seconds
5	$V_{ m mag}$	:	ence
9	$G_{ m mag}$	:	ia Source ID
7	$G_{ m BP}-G_{ m RP}$	:	
∞	$V_{ m mag}$ (Gaia)	:	$V$ magnitude of the star as determined by the transformations from G mag to V mag using $V = G + 0.02704 - 0.01424^*(BP-RP) + 0.2156^*(BP-RP)^2 - 0.01426$
6	RV	$(\text{km s}^{-1})$	Radial velocity as given by the RV reference
10	Error	$({\rm km}\ {\rm s}^{-1})$	Radial velocity error as given by the RV reference
11	$RV_{Gaia}$	$({\rm km}\ {\rm s}^{-1})$	Radial velocity as given by the Gaia Source ID
12	Error	$({\rm km}\ {\rm s}^{-1})$	Radial velocity error as given by the Gaia Source ID
13	Parallax	(mas)	
14	Error	(mas)	Q s
15	Distance	(kpc)	Inverse parallax distance (1/parallax)
16	Error	(kpc)	$ax_{error}/(parallax^2)$
17	Distancecorrected	(kpc)	Corrected inverse parallax distance (1/(parallax +0.026)) based on Huang et al. (2021)
18		(kpc)	Corrected inverse parallax distance error (parallax error/((parallax +0.026) <sup>2</sup> )) based on Huang et al. (2021)
19	Relative error	:	Relative error of the corrected distance as given by Gaia
20		(kpc)	50th percentile distance as given by Bailer-Jones et al. (2021) based on the Gaia source ID
21		(kpc)	50th percentile error estimated by the 84th percentile distance and the 16th percentile distance as given by Bailer-Jones et al. (2021) based on the Gaia source ID
,			(dist84-dist16)/2)
22	Relative error	:	Relative error of the 50th percentile distance as given by Bailer-Jones et al. (2021) based on the Gaia source ID
23	Distance StarHorse	(kpc)	50th percentile distance as given by Anders et al. (2022) based on the Gaia source ID
24		(kpc)	50th percentile error estimated by the 84th percentile distance and the 16th percentile distance as given by Anders et al. (2022) based on the Gaia source ID ((dist84-
			$\operatorname{dist}(6/2)$
25	Relative error	:	Relative error of the 50th percentile distance as given by Anders et al. (2022) based on the Gaia source ID
26	PM <sub>B</sub>	$(\text{mas yr}^{-1})$	Proper motion in the R.A. as given by the Gaia source ID
27		$(\text{mas vr}^{-1})$	
28		$(\text{mas yr}^{-1})$	Proper motion in the decl. as given by the Gaia source ID
29		$(\text{mas yr}^{-1})$	
30		· :	Correlation coefficient between the proper motion in R.A. and the proper motion in decl. as given by the Gaia source ID
31	$T_{ m eff}$	(K)	Effective temperature of the star as given by the reference
32		(cgs)	Surface gravity of the star as given by the reference
33	[Fe/H]	:	Metallicity of the star as given by (log ϵ(Fe) – log ϵ(Fe) <sub>☉</sub> ) (solar value of 7.50 taken from Asplund et al. 2009)
34	log ∈(Fe)	:	Logarithmic iron abundance of the star as given by the reference
35	[C/Fe]	:	Carbon abundance ratio of the star as given by ( $\log \epsilon(C) - \log \epsilon(C)_{\odot} - [Fe/H]$ ) (solar value of 8.43 taken from Asplund et al. 2009)
36	$\log \epsilon(C)$	:	Logarithmic carbon abundance of the star as given by the reference
37	$[{ m C/Fe}]_c$	:	Carbon abundance ratio corrected for evolutionary effects from Placco et al. (2014b)
38	$AC_c$	:	Absolute carbon corrected for evolutionary effects from Placco et al. (2014b) ([C/Fe] <sub>c</sub> + [Fe/H] + log $\epsilon$ (C) <sub>o</sub> ) (solar value of 8.43 taken from Asplund et al. 2009)
39	CARDET	:	Flag with "D" if the carbon abundance ratio ([C/Fe]) is detected by the reference and "U" if an upper limit by the reference and "L" if a lower limit by the reference
0			and "X" if none is detected by the reference
04	CEMP	:	riag as C 10f CeMP II $[C/Fe]_C > + 0.7$ and 1 10f CeMP-internetiate II $+0.3C > +0.7$ and N 10f caroon-normal II $[C/Fe]_C > +0.3$ and A 11 there is no by
41	$[\mathrm{Mg/Fe}]$	:	ratio of the star as given by (log e(Mg) – log e(Mg) <sub>☉</sub> – [Fe/H]) (solar value of 7.60 taken from Asplund et al. 2009)

Table 13 (Continued)

Column	Field	Unit	Description
42	log e(Mg)	:	Logarithmic magnesium abundance of the star as given by the reference
43	MAGDET	:	by the reference and "U" if an upper limit by the reference and "L" if a lower limit by the
44	[Sr/Fe]	:	The strontium abundance ratio of the star as given by (log $\epsilon(Sr) - \log \epsilon(Sr) - [Fe/H]$ ) (solar value of 2.87 taken from Asplund et al. 2009)
45	log e(Sr)	:	Logarithmic strontium abundance of the star as given by the reference
46	STRDET	:	the reference and "U" if an upper limit by the reference and "L" if a lower limit by the reference
			and "X" if none is detected by the reference
47	[Y/Fe]	:	(log $\epsilon(Y)$ – log $\epsilon(Y)_{\odot}$ – [Fe/H]) (solar value of 2.21 taken from Asplund et al. 2009)
48	$\log \epsilon(Y)$	:	
49	YTTDET	:	Flag with "D" if the yttrium abundance ratio ([Y/Fe]) is detected by the reference and "U" if an upper limit by the reference and "L" if a lower limit by the reference
			ed by the reference
50	[Ba/Fe]	:	Barium abundance ratio of the star as given by ( $\log \epsilon(Ba) - \log \epsilon(Ba)_{\odot} - [Fe/H]$ ) (solar value of 2.18 taken from Asplund et al. 2009)
51	log ∈(Ba)	:	
52	BARDET	:	a/Fe]) is detected by the reference and "U" if an upper limit by the reference and "L" if a lower limit by the reference
			and "X" if none is detected by the reference
53	[Eu/Fe]	:	Europium abundance ratio of the star as given by ( $\log \epsilon(\mathrm{Eu}) - \log$
			$\epsilon(\mathrm{Eu})_{\odot}$ – [Fe/H]) (solar value of 0.52 taken from Asplund et al. 2009)
54	log ϵ(Eu)	:	Logarithmic europium abundance of the star as given by the reference
55	EURDET	:	Flag with "D" if the europium abundance ratio ([Eu/Fe]) is detected by the reference and "U" if an upper limit by the reference and "L" if a lower limit by the
			reference and "X" if none is detected by the reference
56	Class	:	Class of the star as given in Table 1
57	S/N	:	Average signal-to-noise ratio of the spectrum as given by the reference
58	Reference	:	Reference for the star
59	$V_{ m mag}$ reference	:	Reference for the V magnitude of the star
09	Distance AGAMA	:	Reference for the distance used in AGAMA (StartHorse prioritized over BJ21 unless the StartHorse distance has a relative error greater than 0.3, if both have a relative
			error greater than 0.3 we adopt no distance estimate)
61	RV reference	:	Reference for the RV
62	$(\nu_r, \nu_\phi, \nu_z)$	$(\text{km s}^{-1})$	Cylindrical velocities of the star as given by AGAMA
63	Error	$(\text{km s}^{-1})$	Cylindrical velocity errors of the star as given by Monte Carlo sampling through AGAMA
64	$(J_r,J_\phi,J_{\mathbb{Z}})$	(kpc km	Cylindrical actions of the star as given by AGAMA
į	ţ	( ,	
65	Error	$(\text{kpc km} \text{s}^{-1})$	Cylindrical action errors of the star as given by Monte Carlo sampling through AGAMA
99	Energy	$(km^2 s^{-2})$	Orbital energy of the star as given by AGAMA
29	Error	$(\text{km}^2 \text{ s}^{-2})$	Orbital energy error of the star as given by Monte Carlo sampling through AGAMA
89	l'neri	(kpc)	Galactic pericentric distance of the star as given by AGAMA
69	Error	(kpc)	Galactic pericentric distance error of the star as given by Monte Carlo sampling through AGAMA
70	$r_{ m apo}$	(kpc)	Galactic apocentric distance of the star as given by AGAMA
71	Error	(kpc)	Galactic apocentric distance error of the star as given by Monte Carlo sampling through AGAMA.
72	$Z_{\text{max}}$	(kpc)	Maximum height above, or below, the Galactic plane of the star as given by AGAMA
73	Error	(kpc)	Maximum height above, or below, the Galactic plane error of the star as given by Monte Carlo sampling through AGAMA
74	Eccentricity	:	Eccentricity of the star given by $(r_{\rm apo} - r_{\rm pen})/(r_{\rm apo} + r_{\rm pen})$ through AGAMA
75	Error	:	Eccentricity error of the star as given by Monte Carlo sampling through AGAMA

(This table is available in its entirety in machine-readable form.)

Table 14
Identified CEMP Stars and Their Group Association

Name	Group	$T_{\rm eff}$ (K)	log g	(Fe/H)	(C/Fe)	$(C/Fe)_c$	$AC_c$	(Mg/Fe)	(Sr/Fe)	(Y/Fe)	(Ba/Fe)	(Eu/Fe)
HE 0010-3422	I	5400	3.100	-2.70	+1.84	+1.86	7.59	+0.26	+0.77	+0.93	+1.46	+1.64
J004539.30-745729.4	I	4947	2.010	-2.00	+0.93	+0.99	7.42	•••	+0.83	•••	+0.37	+0.55
J005327.84-025316.8	I	4370	0.560	-2.16	+0.40	+0.88	7.15	+0.48	-0.05	-0.31	-0.24	+0.39
J005419.65-061155.4	I	4707	1.030	-2.32	+0.50	+0.98	7.09	+0.52	+0.26	-0.25	-0.21	+0.59
J010839.60-285701.0*	II	4843	1.170	-2.87	+0.10	+0.76	6.32	+0.41	+0.41	•••	-0.52	+0.45
J014908.00-491143.0* J015656.33-140210.9	II I	4556 4622	0.720 1.090	$-3.08 \\ -2.08$	$+0.07 \\ +0.37$	$+0.81 \\ +0.83$	6.16 7.18	$+0.63 \\ +0.37$	-0.01 +0.10	-0.23	-0.39 $-0.11$	+0.35 +0.76
J022124.00-405648.0	II	4797	0.940	-2.52	+0.37 +0.20	+0.83	6.74	+0.5 <i>1</i>	-0.18	-0.23	-0.11 $-0.18$	+0.76
J022741.04-051922.8		4498	0.960	-2.38	+0.20	+0.73	6.78	+0.41	+0.72	-0.12	-0.18	+0.42
J023558.67-674552.0	I	4653	0.910	-1.55	+0.97	+1.11	7.99		+0.10		+0.49	+0.50
J024138.88-042736.0	I/II	4539	0.790	-2.48	+0.40	+0.97	6.92	+0.51	+0.24	-0.27	-0.26	+0.48
170910005101390	I	4463	1.193	-2.16	+0.27	+0.75	7.02	•••	•••	+0.01	+0.62	+0.84
J024858.41-684306.4	II	4977	1.600	-3.71	+0.66	+0.92	5.64	+0.57	-0.15	•••	+0.59	+1.00
J025007.19-514514.8	I	4707	1.400	-2.20	+1.04	+1.28	7.51	•••	-0.05	•••	+0.48	+0.62
J030639.10-692040.0	II	4644	1.040	-2.79	+0.10	+0.79	6.43	+0.47	-0.02	•••	+0.20	+0.32
J030714.88-053455.2	I	4568	1.200	-2.23	+0.44	+0.90	7.10	+0.53	+0.38	+0.11	+0.17	+0.50
HE 0420+0123	II	4800	1.450	-3.03	+0.33	+0.78	6.18	+0.44	+0.11	-0.10	+0.08	+0.79
HE 0448-4806	I	5900	3.600	-2.30	+2.28	+2.28	8.41	+0.48	+1.14	+0.97	+1.82	+1.91
161209002101393 J062208.92-675713.1	I II	4478 4650	1.101 1.040	-1.84 $-3.41$	$+0.43 \\ +0.04$	+0.78 +0.79	7.38 5.81	+0.19	-0.37	+0.07 	+0.07 $-0.03$	+0.49 +0.62
J063447.15-622355.0	II	4432	0.550	-3.41 $-3.41$	+0.04 +0.08	+0.79 $+0.82$	5.84	+0.19 +0.62	-0.57 -0.56		-0.03 + 0.41	+0.82 +0.89
J070520.28-334324.3	I	4757	1.270	-2.24	+0.27	+0.78	6.97	+0.28	+0.03	-0.26	-0.17	+0.62
J071142.53-343236.8	I	4767	1.330	-1.96	+0.47	+0.81	7.28	+0.31	+0.24	+0.07	+0.50	+1.30
J072500.21-702203.8	II	4837	1.400	-2.65	+0.30	+0.77	6.55	+0.30	-0.14		-0.30	+0.33
J091858.90-231151.2	I	4662	1.050	-2.05	+0.32	+0.79	7.17	+0.23	-0.51	-0.44	-0.06	+0.71
J100448.58-270650.0	I/II	4831	1.420	-2.40	+0.55	+0.96	6.99	+0.45	-0.00	+0.14	-0.38	+0.41
J100824.90-231412.0*	I	4719	1.180	-1.95	+0.40	+0.78	7.26	+0.31	•••	•••	+0.36	+0.55
150106004101102	I/II	4452	0.989	-2.46	+0.36	+0.93	6.90	•••	•••	+0.08	+0.61	+0.98
170510002301002	•••	5107	2.645	-0.90	+0.92	+0.94	8.47	•••	+2.23	•••	-0.20	+0.90
J103649.93+121219.8	III	6000	4.000	-3.20	+1.54	+1.54	6.77	-0.05	-0.52	+0.23	+1.17	+1.26
J105433.10+052812.7	II	5030	1.880	-3.30	+0.82	+0.86	5.99	+0.41	-0.30	+0.28	-0.52	+0.44
J105941.36-205225.4 J114440.80-040950.4	I I/II	4370 4614	0.560 1.030	-2.16 $-2.52$	+0.28 +0.33	$+0.79 \\ +0.90$	7.06 6.81	$+0.41 \\ +0.36$	+0.26 $-0.01$	-0.28 $-0.39$	-0.07 $-0.26$	+0.35 +0.58
J114730.00-052143.2	1/11 I	4707	1.260	-2.32 $-2.00$	+0.33	+0.75	7.18	+0.36	0.00	-0.39 $-0.32$	-0.20 $-0.22$	+0.31
J115337.30-020037.0*	I/II	5151	2.740	-2.43	+1.01	+1.03	7.13	+0.10	+0.33	-0.52	+0.54	+1.11
170507007201014		4474	1.636	-0.83	+0.75	+0.75	8.35			-0.31	+0.36	+0.43
J120456.16-075924.0	I/II	4530	0.830	-2.72	+0.50	+1.09	6.80	+0.62	-0.29	-0.12	-0.11	+0.33
190212003001078	Í	4344	1.039	-2.24	+0.39	+0.89	7.08			+0.29	+0.48	+0.82
J120913.22-141531.4	I	4370	0.560	-2.11	+0.20	+0.73	7.05	+0.36	-0.01	-0.29	+0.11	+0.81
160608002001237	I	4673	1.580	-1.87	+0.49	+0.74	7.30	•••	•••	+0.61	-0.01	+0.82
J122926.88-044232.4	I	4523	1.130	-2.23	+0.28	+0.79	6.99	+0.54	0.00	-0.12	-0.22	+0.46
J123550.10-313111.0*	II	4706	1.320	-2.59	+0.32	+0.84	6.68	+0.38	+0.11	•••	+0.06	+0.57
J132141.80-432006.0	I	4954	1.250	-2.03	+0.34	+0.76	7.16	+0.30	+0.67		+0.04	+0.66
140311008101218 190212003501241	I	4455	1.107	-1.92 $-1.17$	+0.35	+0.74	7.25 7.97	•••		-0.03 	+0.52	+0.75
J132545.54-174754.7	I I	4402 4588	1.718 0.830	-1.17 -2.32	+0.63 +0.18	+0.71 +0.78	6.89	+0.42	+1.89 $-0.02$	-0.33	+0.56 $-0.44$	+0.65 +0.40
J133308.90-465407.9	II	4591	0.790	-3.02	+0.16	+0.78	6.19		0.00	-0.55	-0.17	+0.49
J133513.92-011051.6	II	4568	1.070	-2.45	+0.21	+0.82	6.80	+0.38	-0.39	-0.38	-0.22	+0.53
J133748.96-082616.8	II	4265	0.250	-2.62	+0.34	+0.94	6.75	+0.56	+0.17	+0.02	+0.02	+0.93
J134254.00-071702.4	II	4568	0.900	-2.51	+0.14	+0.79	6.71	+0.39	+0.04	-0.25	-0.26	+0.44
160327005101029	I	4545	1.401	-2.26	+0.35	+0.79	6.96			+0.29	+0.36	+0.88
J140437.68+001113.2	I	4370	0.260	-1.87	+0.96	+1.17	7.73	+0.33	+0.43	-0.01	+0.38	+0.58
J141808.68-284207.7	I	4672	1.260	-2.32	+0.30	+0.81	6.92	+0.27	-0.41	-0.34	-0.11	+0.43
170602003701197	I	4345	0.777	-1.85	+0.31	+0.71	7.29	•••	•••	-0.10	+0.17	+0.43
J145437.92+083037.9		4891	1.550	-2.31	+0.30	+0.71	6.83	+0.30	-0.10		+0.25	+1.10
170410003901021	I	4510	1.268	-2.12	+0.34	+0.78	7.09			+0.37	+0.63	+0.93
J150024.96-061337.2	I I	4460 4300	0.730	-2.05	+0.33	+0.79	7.17	+0.41	+0.12	-0.22	-0.10	+0.39
J150757.12-065959.9 170128003901303	I	4300 4460	0.520 1.311	-2.07 $-1.17$	+0.44 +0.75	$+0.87 \\ +0.82$	7.23 8.07	+0.59 	+0.12 +1.74	-0.22 +0.26	-0.10 +0.51	+0.36 +0.54
J151335.49-124433.9	I	4855	1.600	-1.17 $-2.04$	+0.75 +0.45	+0.82 $+0.75$	7.14	-0.34	+1.74 $-2.87$	+0.20	+0.31 -0.10	+0.54 +0.55
J151558.30-203821.0	I/II	4743	1.100	-2.65	+0.43 +0.54	+0.73 $+1.08$	6.86	-0.54 + 0.52	-2.87 +0.27		-0.10 $-0.39$	+0.35 +0.36
J152110.32-060758.8	I	4707	1.330	-2.00	+0.34	+0.72	7.15	+0.30	-0.18	-0.07	+0.10	+0.93
J152306.75-793007.2	II	4737	1.070	-2.55	+0.28	+0.88	6.76		+0.71		-0.43	+0.36
140313005201048	I	4306	0.850	-2.00	+0.30	+0.76	7.19			+0.15	+0.34	+0.85
1 10313003201010							7.24					

Table 14 (Continued)

Name	Group	T <sub>eff</sub> (K)	log g	(Fe/H)	(C/Fe)	$(C/Fe)_c$	$AC_c$	(Mg/Fe)	(Sr/Fe)	(Y/Fe)	(Ba/Fe)	(Eu/Fe)
140609002101156	П	4394	1.290	-2.47	+0.35	+0.84	6.80			+0.25	+0.79	+1.08
160422005101104		4480	1.664	-0.93	+0.81	+0.84	8.34		+1.56		+0.42	+0.51
J160447.75-293146.7	II	4675	1.050	-2.66	+0.26	+0.89	6.66	+0.66	+0.26		+0.01	+0.31
150504002401029		4414	1.502	-0.85	+0.71	+0.72	8.31			+0.44	+0.23	+0.61
J160951.12-094116.8	II	4634	0.660	-2.66	+0.25	+0.89	6.66	+0.56	-0.06	-0.37	-0.30	+0.41
150429003601280	I	4450	1.208	-2.05	+0.27	+0.72	7.10		+2.22	+0.26	+0.57	+1.08
J161228.32-084807.2	I	4350	0.560	-2.11	+0.17	+0.72	7.04	+0.35	+0.29	-0.16	+0.04	+0.58
140711001301301		4335	1.654	-0.84	+0.69	+0.71	8.29			-0.34	-0.15	+0.38
J161635.52-040115.6	I	4370	0.630	-1.97	+0.25	+0.71	7.17	+0.51	+0.08	-0.17	-0.19	+0.52
150412005101252	I	4376	1.080	-1.89	+0.31	+0.72	7.25			-0.22	+0.43	+0.72
J164757.15-651940.6	II	4650	1.090	-3.05	+0.43	+1.08	6.46	+0.44	-0.02		-0.01	+0.58
J165244.66-271205.2	II	4675	1.130	-3.18	+0.34	+1.00	6.25	+0.56	-0.08		-0.17	+0.42
170409003801263		4505	2.053	-0.82	+0.82	+0.86	8.47		+1.09	-0.02	+0.03	+0.39
160418005101206		4265	1.478	-0.95	+0.76	+0.78	8.26		+1.16	+0.02	-0.30	+0.51
140810002701008		4672	2.378	-0.81	+0.71	+0.74	8.37		+1.39	+1.36	+0.05	+0.47
J174922.26-455103.8	II	4797	1.300	-2.77	+0.55	+1.04	6.70	+0.47	0.00		+0.06	+0.42
150408005901186	I	4502	2.083	-1.02	+0.74	+0.77	8.18			+0.59	+0.39	+0.72
J183013.50-455510.0	I	4765	1.200	-3.57	+2.34	+2.62	7.48	+0.57	-0.56	-0.28	+0.35	+0.69
J183108.20-491105.0	I	4545	1.150	-2.09	+0.31	+0.78	7.12				-0.05	+0.32
170724002601134	I	4464	1.065	-1.79	+0.39	+0.74	7.39			+0.04	+0.46	+0.52
J192632.80-584657.0	I/II	4590	1.000	-2.49	+0.51	+1.05	6.99	+0.27	+0.38		-0.35	+0.76
BD-185550	II	4790	1.150	-3.10	+0.32	+0.97	6.30	+0.61	-0.93	-0.33	-0.80	+0.35
J202029.20-270735.0*	II	4625	0.950	-3.01	+0.26	+0.95	6.37	+0.55	-0.25		-0.34	+0.81
J203622.56-071420.4	I	4283	0.070	-2.41	+0.88	+1.26	7.28	+0.26	+0.02	-0.56	-0.57	+0.48
J203843.20-002333.0	II	4630	1.200	-2.91	+0.23	+0.84	6.36	+0.36	+0.54	+0.21	+0.83	+1.64
J203859.04-025212.0	I	4280	0.060	-2.16	+0.22	+0.77	7.04	+0.40	+0.39	-0.39	-0.26	+0.59
BPS CS 22955-0174	II	5520	1.350	-3.10	+0.50	+1.01	6.34	+0.61	+0.40	-0.14	-0.23	+0.35
J205849.20-035432.4		4831	1.650	-2.36	+0.40	+0.73	6.80	+0.36	-0.24	-0.26	-0.09	+0.36
HE 2122-4707	I	5147	2.500	-2.42	+1.72	+1.74	7.75	+0.38		+0.76	+1.98	+2.00
BPS BS 17569-0049	II	4700	1.200	-3.00	+0.09	+0.73	6.16	+0.35	+0.53	+0.19	+0.27	+0.83
BPS CS 2289-0052	II/III	4850	1.600	-3.00	+0.95	+1.24	6.67	+0.17	+0.60	+0.33	+0.93	+1.45
J222203.44-802459.2	ĬI	4684	0.800	-2.50	+0.20	+0.83	6.76	+0.28	-0.80		-0.30	+0.37
BPS CS 22886-0043		6000	1.800	-2.40	+0.51	+0.71	6.74	+0.55	+1.01	+0.29	+0.54	+1.04
J222236.00-013827.0*	I/II	5118	2.330	-2.82	+1.16	+1.17	6.78	+0.12	-0.09		-1.22	+0.66
140814005401260		4446	1.782	-0.85	+0.74	+0.77	8.35		+1.16	+0.45	+0.13	+0.40
J225625.44-071955.2		4558	1.200	-2.26	+0.18	+0.71	6.88	+0.42	+0.08	-0.02	+0.26	+1.10
J231300.00-450707.0*	II	4804	1.450	-2.53	+0.40	+0.83	6.73	+0.11	-0.37		-0.52	+0.55
BPS CS 22945-0017	I	6080	3.700	-2.73	+1.78	+1.78	7.48	+0.26	+0.38	+0.07	+0.48	+1.13
HE 2323-6549	II	5215	2.600	-3.35	+0.72	+0.73	5.81	+0.55	+0.03	-0.46	-0.58	+0.58
BPS CS 29517-0025	II	5300	1.200	-2.57	+0.72	+0.73	6.59	+0.42			-0.21	+0.55
DI 5 C5 27517-0025	11	5500	1.200	2.31	1 0.17	10.13	0.57	10.72			0.41	10.55

**Note.** The CEMP groups are given in Yoon et al. (2016). Stars with a "\*" at the end of their name denote that they did not make the RPE final sample. (This table is available in machine-readable form.)

Name	[Fe/H]	$(C/Fe)_c$	(Mg/Fe)	(Sr/Fe)	(Y/Fe)	(Ba/Fe)	(Eu/Fe)
			CDTG-1-	-rI			
			Structure: M	WTD			
		Group	association: C-3: N	Ialhan et al. (2022)			
	Stel	lar association: 2MA	ASS J00452379-211	2161 (CDTG-16: G	dudin et al. 2021)		
		Stellar association: J	223454.50-660517.0	0 (DTG-132: Shank	et al. 2022a)		
		Globul	ar association: no g	lobular associations			
		Dwarf galax	xy association: no d	warf galaxy associa	tions		
161116002201265	-0.90	+0.50	•••		+0.10	-0.09	+0.54
J004523.79-211216.1	-2.63	+0.48	+0.35	-0.10		-0.25	+0.40
140814006001030	-0.94	+0.47			+0.06	+0.02	+0.49
170911004701352	-1.12	+0.47			+0.60	+0.36	+0.48
150829005701125	-1.24	+0.48			+0.29	+0.21	+0.43
150205005001158	-0.85	+0.48			+0.07	+0.12	+0.48
170205005401195	-0.88	+0.57		+1.42	+0.01	+0.16	+0.41
150210004701143	-1.37	+0.46			+0.05	+0.09	+0.45

Table 15 (Continued)

Name	[Fe/H]	$(C/Fe)_c$	(Mg/Fe)	(Sr/Fe)	(Y/Fe)	(Ba/Fe)	(Eu/Fe)
150206004301060	-1.63	+0.65		•••	+0.08	+0.47	+0.48
170407004101026	-0.83	+0.44			+0.06	+0.10	+0.44
140807004501246	-0.88	+0.47			+0.25	+0.36	+0.50
161109003101144	-1.05	+0.56			+0.27	+0.56	+0.56
150828003701120	-0.81	+0.46			+0.70	+0.15	+0.41
160817003601092	-0.82	+0.43			+0.42	+0.31	+0.56
170908002801072	-1.14	+0.42			+0.36	+0.21	+0.55
J223454.47-660517.2	-2.49	+0.31	+0.25	-0.03		-0.20	+0.40
140814005401260	-0.85	+0.77			+0.45	+0.13	+0.40
150830004601369	-0.96	+0.54		•••	+0.34	+0.46	+0.50
$\mu \pm \sigma([{ m X/Y}])$	$-\textbf{0.96} \pm \textbf{0.21}$	$\mathbf{+0.47} \pm 0.06$	$+$ 0.30 $\pm$	$-0.06\pm0.06$	$\mathbf{+0.25} \pm 0.21$	$\mathbf{+0.18} \pm 0.23$	$+0.47\pm0.06$

**Note.**  $\mu$  and  $\sigma$ , bolded for clarity, represent the biweight estimates of the location and scale for the abundances in the CDTG. (This table is available in its entirety in machine-readable form.)

Cluster	N Stars	$(\langle v_r \rangle,  \langle v_\phi \rangle,  \langle v_z \rangle)$	$(\langle J_r  angle, \ \langle J_\phi  angle, \ \langle J_z  angle)$	$\langle E  angle$	$\langle ecc \rangle$
		$(\sigma_{\langle \nu_r \rangle}, \sigma_{\langle \nu_\phi \rangle}, \sigma_{\langle \nu_z \rangle}) \ (\text{km s}^{-1})$	$(\sigma_{\langle J_r \rangle}, \sigma_{\langle J_\phi \rangle}, \sigma_{\langle J_z \rangle}) \ (\mathrm{kpc} \ \mathrm{km} \ \mathrm{s}^{-1})$	$(10^5 \text{ km}^2 \text{ s}^{-2})$	$\sigma_{ m \langle ecc  angle}$
CDTG-1-rI	18	(-17.4,91.9, -25.5)	(239.7,648.7,162.3)	-1.768	0.573
		(74.9,25.4,59.9)	(52.3,216.6,13.1)	0.054	0.096
CDTG-2-rI	18	(33.9,21.8, -3.6)	(580.1,157.5,55.9)	-1.808	0.898
		(104.1,12.1,51.1)	(59.6,83.1,25.3)	0.027	0.047
CDTG-3-rI	17	(1.4,181.2,21.4)	(89.5,1446.0,136.0)	-1.596	0.267
		(65.9,25.8,69.6)	(57.7,83.9,31.9)	0.032	0.093
CDTG-4-rI	15	(-27.0,72.3,5.2)	(164.6,295.6,243.3)	-1.936	0.625
		(59.9,50.3,101.3)	(75.4,199.8,32.5)	0.027	0.201
CDTG-5-rI	15	(-51.3,135.5, -6.0)	(149.2,845.2,36.8)	-1.835	0.434
		(55.0,25.8,41.1)	(46.8,96.6,5.8)	0.016	0.078
CDTG-6-rI	14	(15.3,69.6, -66.2)	(319.4,437.3,259.6)	-1.772	0.678
		(109.0,15.3,86.6)	(68.3,147.6,27.3)	0.040	0.090
CDTG-7-rI	13	(-23.8, -9.4, 1.0)	(799.2, -81.0, 78.6)	-1.683	0.941
		(156.7,13.7,49.7)	(30.6,104.3,33.1)	0.031	0.035
CDTG-8-rI	12	(50.9, -27.6, -6.0)	(439.6, -204.3, 576.7)	-1.641	0.719
		(123.8,48.1,140.1)	(89.7,288.6,52.2)	0.060	0.063
CDTG-9-rI	12	(-25.0,205.6,3.9)	(18.0,1408.8,108.1)	-1.650	0.129
		(27.7,20.7,62.4)	(17.3,40.5,14.1)	0.014	0.058
CDTG-10-rI	11	(-15.7,168.5, -108.5)	(311.9,1318.2,1076.9)	-1.346	0.409
		(121.3,56.9,175.0)	(187.3,176.4,100.3)	0.067	0.112
CDTG-11-rI	11	(24.4, -35.6, -15.1)	(497.5, -263.2, 79.8)	-1.810	0.861
		(102.4,13.0,63.6)	(67.3,77.0,14.0)	0.049	0.023
CDTG-12-rI	10	(39.5,162.2,13.8)	(132.1,1345.5,55.9)	-1.644	0.349
		(75.2,10.4,46.3)	(17.5,39.2,5.8)	0.012	0.023
CDTG-13-rI	9	(16.0,187.4, -24.2)	(76.4,1610.4,27.9)	-1.603	0.240
		(57.2,15.9,35.4)	(46.4,87.5,7.8)	0.008	0.085
CDTG-14-rI	9	(-60.3,73.7, -17.7)	(320.7,471.9,37.1)	-1.874	0.687
		(68.6,11.0,32.2)	(30.7,57.0,16.6)	0.028	0.023
CDTG-15-rI	8	(-26.6, -18.7, 12.7)	(141.7, -38.7, 156.3)	-2.144	0.783
		(88.0,58.5,58.0)	(22.1,147.6,26.7)	0.045	0.104
CDTG-16-rI	8	(-25.6,185.3,9.1)	(60.1,1461.2,32.3)	-1.651	0.229
		(50.0,5.3,18.9)	(18.4,27.1,9.8)	0.007	0.033
CDTG-17-rI	8	(-63.0,102.0,28.0)	(222.2,639.5,85.6)	-1.840	0.569
		(53.5,8.2,48.3)	(43.2,78.1,9.7)	0.018	0.060
CDTG-18-rI	8	(-219.0, 8.7, -27.3)	(1157.9,66.4,58.1)	-1.535	0.955
		(104.9,9.7,52.2)	(57.5,75.2,35.8)	0.045	0.021
CDTG-19-rI	8	(-58.7,56.3, -93.9)	(639.6,520.7,2011.1)	-1.248	0.525
		(66.8,51.6,267.1)	(238.6,426.3,62.5)	0.063	0.084
CDTG-20-rI	7	(185.0, -4.5, -22.6)	(1572.2, -20.6, 76.4)	-1.380	0.973
		(438.7,24.4,81.8)	(94.1,152.4,35.6)	0.022	0.014
CDTG-21-rI	6	(44.0, -98.8, -0.4)	(231.0, -645.8, 347.6)	-1.694	0.530
		(116.5,8.0,105.5)	(52.3,34.5,23.5)	0.032	0.060
CDTG-22-rI	6	(-28.9,174.0,8.3)	(95.7,1383.0,9.2)	-1.674	0.296

Table 16 (Continued)

Cluster	N Stars	$(\langle v_r \rangle,  \langle v_\phi \rangle,  \langle v_z \rangle)$	$(\langle J_r  angle, \ \langle J_\phi  angle, \ \langle J_z  angle)$	$\langle E  angle$	$\langle ecc \rangle$
		$(\sigma_{\langle \nu_r \rangle}, \sigma_{\langle \nu_\phi \rangle}, \sigma_{\langle \nu_z \rangle}) \ (\mathrm{km \ s}^{-1})$	$(\sigma_{\langle J_r \rangle}, \sigma_{\langle J_\phi \rangle}, \sigma_{\langle J_z \rangle}) \ ( ext{kpc km s}^{-1})$	$(10^5 \text{ km}^2 \text{ s}^{-2})$	$\sigma_{ m \langle ecc  angle}$
		(53.7,16.3,25.0)	(15.8,60.5,4.8)	0.015	0.026
CDTG-23-rI	6	(-13.5,95.8,37.1)	(348.6,794.4,59.0)	-1.721	0.603
		(106.8,10.5,33.4)	(15.6,34.8,11.1)	0.010	0.014
CDTG-24-rI	5	(-230.2,67.3, -72.2)	(838.4,407.3,195.0)	-1.523	0.839
		(32.1,24.2,117.9)	(50.4,9.4,17.6)	0.016	0.023
CDTG-25-rI	5	(-35.5,139.9,18.3)	(148.2,1183.9,116.0)	-1.657	0.381
		(57.4,19.7,65.0)	(14.9,28.1,5.3)	0.003	0.021
CDTG-26-rI	5	(-75.9,159.1, -19.5)	(85.4,809.7,38.2)	-1.892	0.349
		(26.2,10.7,20.8)	(19.1,43.7,10.3)	0.008	0.040
CDTG-27-rI	5	(-44.5,104.3,26.7)	(182.0,612.4,35.6)	-1.920	0.532
		(26.8,10.0,49.9)	(22.6,83.3,6.2)	0.021	0.049
CDTG-28-rI	5	(55.1,35.2, -90.9)	(443.8,289.2,1483.1)	-1.350	0.520
		(129.6,38.9,187.3)	(169.4,373.9,67.1)	0.065	0.080

(This table is available in machine-readable form.)

 Table 17

 CDTG Abundance Means, Dispersions, and IQRs for the r-I Sample

Cluster	N Stars	(Fe/H)	(C/Fe) <sub>c</sub>	(Mg/Fe)	(Sr/Fe)	(Y/Fe)	(Ba/Fe)	(Eu/Fe)
CDTG-1-rI	18	$-0.96 \pm 0.21$	$+0.47 \pm 0.06$	+0.30 ±	$-0.06 \pm 0.06$	$+0.25 \pm 0.21$	$+0.18 \pm 0.23$	$+0.47 \pm 0.06$
CDTG-2-rI	18	$-1.17 \pm 0.54$	$+0.36 \pm 0.17$	$+0.61 \pm 0.00$	$+0.08 \pm 0.64$	$+0.15 \pm 0.25$	$+0.23 \pm 0.15$	$+0.52 \pm 0.12$
CDTG-3-rI	17	$-0.88 \pm 0.10$	$+0.48 \pm 0.10$		$+1.08 \pm 0.48$	$+0.14 \pm 0.14$	$+0.21 \pm 0.19$	$+0.53 \pm 0.10$
CDTG-4-rI	15	$-0.97 \pm 0.22$	$+0.53 \pm 0.07$	$+0.35\pm$	$+0.37\pm$	$+0.14 \pm 0.19$	$+0.19 \pm 0.28$	$+0.52 \pm 0.10$
CDTG-5-rI	15	$-0.85\pm0.06$	$+0.48 \pm 0.06$		$+0.95\pm$	$+0.07 \pm 0.15$	$+0.12 \pm 0.20$	$+0.50\pm0.08$
CDTG-6-rI	14	$-1.63 \pm 0.78$	$+0.54 \pm 0.13$	$+0.41 \pm 0.08$	$+0.05 \pm 0.99$	$+0.03 \pm 0.18$	$+0.21 \pm 0.24$	$+0.49 \pm 0.10$
CDTG-7-rI	13	$-1.53 \pm 0.57$	$+0.25 \pm 0.18$	$+0.37 \pm 0.14$	$+0.07 \pm 0.12$	$+0.16 \pm 0.19$	$+0.22 \pm 0.20$	$+0.46 \pm 0.09$
CDTG-8-rI	12	$-1.97 \pm 0.79$	$+0.57 \pm 0.35$	$+0.51 \pm 0.05$	$+0.13 \pm 0.18$	$+0.13 \pm 0.34$	$+0.02 \pm 0.36$	$+0.53 \pm 0.09$
CDTG-9-rI	12	$-0.84\pm0.02$	$+0.47 \pm 0.07$		$+1.59 \pm$	$+0.08 \pm 0.17$	$+0.13 \pm 0.18$	$+0.51 \pm 0.06$
CDTG-10-rI	11	$-2.11 \pm 0.59$	$+0.17 \pm 0.35$	$+0.33 \pm 0.09$	$+0.06 \pm 0.31$	$-0.23 \pm 0.15$	$-0.08 \pm 0.24$	$+0.44 \pm 0.11$
CDTG-11-rI	11	$-1.48 \pm 0.59$	$+0.35 \pm 0.25$	$+0.37\pm$	$+0.17 \pm 0.11$	$+0.11 \pm 0.11$	$+0.15 \pm 0.20$	$+0.48 \pm 0.11$
CDTG-12-rI	10	$-0.90 \pm 0.10$	$+0.49 \pm 0.06$	$+0.53 \pm$	$+0.70 \pm 0.75$	$+0.12 \pm 0.19$	$+0.15 \pm 0.10$	$+0.50 \pm 0.14$
CDTG-13-rI	9	$-0.86 \pm 0.04$	$+0.49 \pm 0.05$			$+0.16 \pm 0.14$	$+0.15 \pm 0.07$	$+0.49 \pm 0.08$
CDTG-14-rI	9	$-1.32 \pm 0.65$	$+0.52 \pm 0.04$		$+0.17\pm$	$+0.31 \pm 0.18$	$+0.30 \pm 0.29$	$+0.47\pm0.08$
CDTG-15-rI	8	$-1.43 \pm 0.13$	$+0.53 \pm 0.07$	$+0.44 \pm 0.03$	$+0.62\pm$	$+0.26\pm0.06$	$+0.23 \pm 0.19$	$+0.48 \pm 0.07$
CDTG-16-rI	8	$-0.83 \pm 0.09$	$+0.42 \pm 0.04$			$+0.18 \pm 0.16$	$+0.28 \pm 0.19$	$+0.49 \pm 0.05$
CDTG-17-rI	8	$-0.89 \pm 0.09$	$+0.53 \pm 0.06$		$+1.14 \pm$	$+0.15 \pm 0.12$	$+0.28 \pm 0.12$	$+0.54 \pm 0.08$
CDTG-18-rI	8	$-1.45 \pm 0.42$	$+0.44 \pm 0.11$	$+0.27\pm$	$+0.23\pm$	$-0.02 \pm 0.12$	$+0.27 \pm 0.14$	$+0.58 \pm 0.11$
CDTG-19-rI	8	$-2.20\pm0.52$	$+0.18 \pm 0.38$	$+0.30 \pm 0.40$	$+0.03 \pm 0.14$	$-0.25 \pm 0.07$	$+0.06 \pm 0.30$	$+0.49 \pm 0.10$
CDTG-20-rI	7	$-1.28 \pm 0.19$	$+0.44 \pm 0.10$	$+0.59\pm$	$+0.35\pm$	$+0.11 \pm 0.08$	$+0.43 \pm 0.15$	$+0.56 \pm 0.15$
CDTG-21-rI	6	$-2.59 \pm 0.43$	$+0.39 \pm 0.41$	$+0.58 \pm 0.11$	$-0.06\pm0.02$	$-0.34\pm$	$-0.09 \pm 0.24$	$+0.38\pm0.06$
CDTG-22-rI	6	$-0.88\pm0.08$	$+0.48 \pm 0.23$	$+0.45\pm$	$-0.05\pm$	$+0.03 \pm 0.19$	$-0.01 \pm 0.04$	$+0.49 \pm 0.11$
CDTG-23-rI	6	$-1.40 \pm 0.65$	$+0.56 \pm 0.15$	$+0.48 \pm$	$+0.31 \pm 0.84$	$-0.13 \pm 0.12$	$-0.08\pm0.21$	$+0.46\pm0.10$
CDTG-24-rI	5	$-1.23 \pm 0.26$	$+0.37 \pm 0.12$	$+0.43 \pm$	$+0.70\pm$	$+0.13 \pm 0.14$	$+0.48 \pm 0.11$	$+0.57 \pm 0.17$
CDTG-25-rI	5	$-0.85\pm0.02$	$+0.55 \pm 0.25$	$+0.31 \pm$	$+0.16\pm$	$+0.01 \pm 0.13$	$+0.10 \pm 0.03$	$+0.44 \pm 0.05$
CDTG-26-rI	5	$-0.90\pm0.18$	$+0.48 \pm 0.11$	•••	•••	$+0.12 \pm 0.28$	$+0.05 \pm 0.29$	$+0.48 \pm 0.10$
CDTG-27-rI	5	$-0.91 \pm 0.10$	$+0.55 \pm 0.05$	•••	•••	$+0.02 \pm 0.12$	$+0.08 \pm 0.14$	$+0.47\pm0.01$
CDTG-28-rI	5	$-1.32 \pm 0.48$	$+0.49\pm0.07$	$+0.47\pm$	$+0.59 \pm$	$+0.06 \pm 0.23$	$+0.25 \pm 0.17$	$+0.53 \pm 0.08$
Biweight (CDTG mean)		$-1.20 \pm 0.08$	$+0.48 \pm 0.02$	$+0.42 \pm 0.02$	$+0.22 \pm 0.08$	$+0.11 \pm 0.02$	$+0.16 \pm 0.03$	$+0.49 \pm 0.01$
Biweight (CDTG std)		$+0.29\pm0.05$	$+0.10\pm0.02$	$+0.07\pm0.02$	$+0.32\pm0.10$	$+0.15\pm0.01$	$+0.19\pm0.02$	$+0.09\pm0.01$
IQR (CDTG mean)		0.57	0.12	0.16	0.57	0.12	0.16	0.05
IQR (CDTG std)		0.45	0.13	0.07	0.55	0.07	0.10	0.03
Biweight (final)		$-1.27 \pm 0.68$	$+0.45 \pm 0.19$	$+0.37 \pm 0.20$	$+0.14 \pm 0.38$	$+0.10 \pm 0.21$	$+0.23 \pm 0.28$	$+0.55 \pm 0.16$
IQR (final)		1.08	0.22	0.24	0.40	0.28	0.36	0.21

Note. The first section of the table lists the biweight location and scale of the abundances for each of the CDTGs. The second section of the table lists the mean and the standard error of the mean (using biweight estimates) for both the location and scale of the abundances of the CDTGs, along with the IQR of the abundances of the CDTGs. The third section of the table lists the biweight location and scale of the final sample for each of the abundances, along with the IQR for each of the abundances in the final sample. The IQR lines are bolded to draw attention to the CDTG elemental-abundance mean IQRs to compare to the final sample abundance IQRs.

(This table is available in machine-readable form.)

NAME	(Fe/H)	$(C/Fe)_c$	(Mg/Fe)	(Sr/Fe)	(Y/Fe)	(Ba/Fe)	(Eu/Fe)		
			CDTG-1-1						
			Structure: M						
		Group as	ssociation: CDTG-3:	Gudin et al. (2021	)				
Group association: CDTG-25: Gudin et al. (2021)									
		Group a	ssociation: DTG-3:	Shank et al. (2022a)	)				
		Group as	ssociation: DTG-36:	Shank et al. (2022a	)				
		Group as	ssociation: DTG-62:	Shank et al. (2022a	)				
		-	ssociation: DTG-82:						
			ssociation: DTG-85:	,	*				
			sociation: DTG-104:	,	*				
		•	sociation: DTG-105:	,	1				
	Ste	llar association: 2MA		,	*				
			J01425445-090416	,	,				
			BPS CS 31078-001	*					
	Ste	ellar association: 2M		`	,				
	510		J10191573-1924464	,					
		Stellar association:		•					
	Ste	llar association: 2MA							
	Sic		J22190836-2333467	,					
			iation: HD 221170 (						
			tion: HD 221170 (D						
			`		2022)				
			ar association: no gl		iono				
140823002702093	-0.97	+0.70	xy association: no dv			+0.49	+0.79		
	-0.97 -1.73	+0.70 -0.16		+1.16	+0.32				
J014254.45-090416.2				+0.30		+0.35	+0.83		
150827004601347	-0.86	+0.33			+0.15	+0.33	+0.75		
BPS CS 31078-0018	-2.85	+0.48	+0.41	+0.28	+0.21	+0.61	+1.16		
170417002601371	-0.88	+0.44	•••	•••	+0.27	+0.41	+0.75		
151225003301245	-1.26	+0.52	•••	•••	+0.31	+0.53	+0.71		
160415002101208	-1.06	+0.45	•••	•••	+0.30	+0.36	+0.83		
140309003101229	-0.90	+0.20	•••	•••	+0.95	+0.09	+0.87		
170414002601288	-0.89	+0.39	•••		+0.10	+0.58	+0.71		
J101915.73-192446.4	-1.11	-0.23	•••	+0.63	•••	+0.73	+0.75		
170510002301002	-0.90	+0.94	•••	+2.23		-0.20	+0.90		
140316003301030	-1.07	+0.53	•••	•••	+0.18	+0.44	+0.91		
150211004201352	-0.83	+0.44	•••		+0.33	+0.16	+0.87		
170413003101109	-0.88	+0.46		+1.44	+0.78	+1.14	+1.37		
J120638.24-291441.1	-3.05	+0.64	+0.09	+0.08	•••	+0.17	+1.06		
190225004201085	-1.19	+0.45	•••	•••	+0.23	+0.48	+1.00		
160424004201111	-0.85	+0.43	•••	•••	+0.36	+0.59	+0.74		
170601003101220	-0.84	+0.47	•••	+1.34	+0.37	+0.44	+0.79		
170615003401240	-1.51	+0.60	•••	•••	+0.12	+0.68	+0.73		
160426007401041	-0.89	+0.42	•••	•••	+0.18	+0.06	+0.72		
J221908.36-233346.7	-2.54	+0.39	•••	+0.27	•••	+0.24	+0.87		
150831005001017	-0.94	+0.37	•••	•••	+0.40	+0.25	+0.71		
HD 221170	-2.19	+0.17	+0.40	+0.17	-0.10	+0.22	+0.81		
$\mu \pm \sigma([{ m X/Y}])$	$-0.96\pm0.20$	$\mathbf{+0.45} \pm 0.14$	$+0.30\pm0.15$	$\mathbf{+0.57} \pm 0.72$	$+0.26\pm0.17$	$+0.39\pm0.26$	$+0.81\pm0.11$		

**Note.**  $\mu$  and  $\sigma$ , bolded for clarity, represent the biweight estimates of the location and scale for the abundances in the CDTG. (This table is available in its entirety in machine-readable form.)

Cluster	N Stars	$(\langle v_r \rangle,  \langle v_\phi \rangle,  \langle v_z \rangle)$	$(\langle J_r  angle, \ \langle J_\phi  angle, \ \langle J_z  angle)$	$\langle E  angle$	$\langle ecc \rangle$
		$(\sigma_{\langle \nu_r \rangle}, \sigma_{\langle \nu_\phi \rangle}, \sigma_{\langle \nu_z \rangle}) \ (\mathrm{km \ s}^{-1})$	$(\sigma_{\langle J_r \rangle}, \sigma_{\langle J_\phi \rangle}, \sigma_{\langle J_z \rangle}) \ ( ext{kpc km s}^{-1})$	$(10^5 \text{ km}^2 \text{ s}^{-2})$	$\sigma_{\langle  m ecc  angle}$
CDTG-1-rII	23	(-28.6,163.0, -6.9)	(117.8,1241.4,51.4)	-1.671	0.338
		(67.2,25.6,47.9)	(94.5,150.1,34.4)	0.030	0.120
CDTG-2-rII	18	(-3.6,17.6,-17.9)	(929.9,146.9,59.3)	-1.612	0.929
		(198.8,11.0,37.3)	(104.4,108.8,31.9)	0.050	0.038
CDTG-3-rII	15	(-73.5,15.4,29.7)	(694.7,128.6,158.2)	-1.682	0.923
		(117.3,26.2,97.6)	(53.5,202.8,42.1)	0.023	0.059
CDTG-4-rII	12	(-312.0,19.7,0.5)	(1460.5,159.9,78.6)	-1.383	0.933
		(166.5,46.2,80.3)	(159.9,343.4,30.3)	0.034	0.044
CDTG-5-rII	9	(36.7, -24.6, 129.7)	(444.1, -193.9, 778.1)	-1.601	0.681
		(99.7,26.9,47.2)	(114.3,185.4,102.9)	0.045	0.087
CDTG-6-rII	8	(-36.0, -9.8, -47.5)	(572.9, -22.7, 316.7)	-1.706	0.925
		(186.6,26.7,112.8)	(86.9,96.2,26.3)	0.033	0.032
CDTG-7-rII	8	(-26.7, -9.9, 37.2)	(581.8, -78.3, 38.1)	-1.797	0.877
		(87.3,34.9,33.6)	(30.0,286.3,13.1)	0.047	0.064
CDTG-8-rII	8	(-37.0, -51.1, 2.5)	(394.5, -248.5, 94.6)	-1.876	0.815
		(112.0,35.2,57.5)	(61.2,231.9,39.1)	0.041	0.105
CDTG-9-rII	4	(50.1,111.7, -73.2)	(220.2,686.4,299.7)	-1.720	0.521
		(52.2,15.0,90.9)	(74.6,170.4,27.2)	0.004	0.097
CDTG-10-rII	4	(-117.6,85.1,18.7)	(133.4,248.7,362.3)	-1.909	0.589
		(76.6,10.6,126.5)	(76.5,150.4,34.2)	0.026	0.205
CDTG-11-rII	4	(-43.6,90.5, -15.5)	(73.0,264.9,130.7)	-2.144	0.524
		(32.3,6.5,49.0)	(17.7,6.7,34.1)	0.025	0.111
CDTG-12-rII	4	(9.2, -146.5, -132.6)	(210.2, -1365.3, 428.3)	-1.467	0.400
		(158.4,12.2,24.1)	(210.6,148.7,58.0)	0.046	0.172
CDTG-13-rII	4	(-67.7,92.1,10.6)	(351.3,745.5,11.9)	-1.770	0.628
		(28.9,7.7,15.3)	(28.2,80.9,5.8)	0.018	0.036
CDTG-14-rII	4	(175.2, -47.3, -28.2)	(877.2, -494.7, 131.6)	-1.527	0.841
		(36.8,12.1,74.5)	(41.6,32.4,13.6)	0.010	0.016
CDTG-15-rII	4	(-117.3,105.8,41.8)	(593.4,1514.8,432.8)	-1.314	0.572
		(33.9,7.0,64.6)	(141.9,154.9,78.5)	0.019	0.062
CDTG-16-rII	3	(118.9, -77.8, -38.6)	(400.3, -596.8, 232.0)	-1.677	0.673
		(25.6,7.0,9.3)	(9.0,91.7,33.7)	0.037	0.019
CDTG-17-rII	3	(90.2,28.1, -83.4)	(1637.0,214.5,393.0)	-1.272	0.952
		(290.5,18.6,52.5)	(93.4,140.4,49.6)	0.024	0.024
CDTG-18-rII	3	(-16.0,65.4,8.5)	(393.1,503.7,39.2)	-1.815	0.704
		(30.4,0.3,12.8)	(8.9,4.8,19.3)	0.009	0.024
CDTG-19-rII	3	(164.4, -36.0, -25.7)	(873.7, -311.2, 42.3)	-1.612	0.895
		(60.7,8.9,22.9)	(34.0,43.0,25.2)	0.028	0.007
CDTG-20-rII	3	(-131.8, -167.6, -222.0)	(309.8, -1291.5, 895.4)	-1.367	0.409
		(4.9,18.0,23.9)	(121.4,40.9,79.1)	0.013	0.075

(This table is available in machine-readable form.)

 Table 20

 CDTG Abundance Means, Dispersions, and IQRs for the r-II Sample

Cluster	N Stars	(Fe/H)	(C/Fe) <sub>c</sub>	(Mg/Fe)	(Sr/Fe)	(Y/Fe)	(Ba/Fe)	(Eu/Fe)
CDTG-1-rII	23	$-0.96 \pm 0.20$	$+0.45 \pm 0.14$	$+0.30 \pm 0.15$	$+0.57 \pm 0.72$	$+0.26 \pm 0.17$	$+0.39 \pm 0.26$	$+0.81 \pm 0.11$
CDTG-2-rII	18	$-1.35 \pm 0.43$	$+0.35 \pm 0.19$	$+0.52\pm$	$+0.21 \pm 0.03$	$+0.21 \pm 0.34$	$+0.43 \pm 0.26$	$+0.79 \pm 0.07$
CDTG-3-rII	15	$-1.23 \pm 0.49$	$+0.42 \pm 0.18$	$+0.29 \pm 0.12$	$+0.28 \pm 0.14$	$+0.14 \pm 0.16$	$+0.50 \pm 0.20$	$+0.75 \pm 0.08$
CDTG-4-rII	12	$-1.25 \pm 0.29$	$+0.37 \pm 0.15$	$+0.55\pm$	$+0.20\pm$	$+0.19 \pm 0.13$	$+0.55 \pm 0.21$	$+0.83 \pm 0.18$
CDTG-5-rII	9	$-2.13 \pm 0.83$	$+0.35 \pm 0.18$	$+0.25 \pm 0.21$	$+0.25 \pm 0.26$	$+0.11 \pm 0.05$	$+0.45 \pm 0.22$	$+1.01 \pm 0.18$
CDTG-6-rII	8	$-1.25 \pm 0.14$	$+0.51 \pm 0.15$	$+0.35\pm$	$+0.63 \pm$	$+0.26 \pm 0.13$	$+0.51 \pm 0.29$	$+0.86 \pm 0.10$
CDTG-7-rII	8	$-1.68\pm0.58$	$+0.19\pm0.24$	$+0.32\pm$	$+0.04 \pm 0.24$	$+0.08\pm0.22$	$+0.44 \pm 0.29$	$+0.88\pm0.08$
CDTG-8-rII	8	$-1.45 \pm 0.54$	$+0.43 \pm 0.17$	•••	$+0.55 \pm 0.40$	$+0.20 \pm 0.19$	$+0.49 \pm 0.23$	$+0.84 \pm 0.21$
CDTG-9-rII	4	$-2.50\pm0.26$	$+0.79 \pm 0.11$	$+0.56\pm$	$+0.78 \pm 0.43$	$+0.03 \pm 0.21$	$+0.47 \pm 0.29$	$+0.99 \pm 0.21$
CDTG-10-rII	4	$-1.40 \pm 0.31$	$+0.54 \pm 0.15$	•••	•••	$+0.33 \pm 0.14$	$+0.66 \pm 0.15$	$+0.91 \pm 0.03$
CDTG-11-rII	4	$-1.37 \pm 0.34$	$+0.58 \pm 0.04$	$-0.35\pm$	$+0.73\pm$	$+0.17 \pm 0.12$	$+0.48 \pm 0.20$	$+0.75 \pm 0.04$
CDTG-12-rII	4	$-2.95 \pm 0.11$	$+0.23 \pm 0.23$	$+0.46\pm$	$+0.31 \pm 0.33$	$+0.11\pm$	$+0.25 \pm 0.42$	$+1.14\pm0.36$
CDTG-13-rII	4	$-1.58 \pm 0.77$	$+0.46 \pm 0.17$	$+0.44\pm$	$+0.76\pm$	$+0.74\pm$	$+0.74 \pm 0.74$	$+1.43 \pm 0.69$
CDTG-14-rII	4	$-1.10\pm0.27$	$+0.48\pm0.10$	•••	•••	$+0.24 \pm 0.05$	$+0.68 \pm 0.09$	$+0.83 \pm 0.07$
CDTG-15-rII	4	$-2.69\pm0.38$	$+0.16 \pm 0.17$	$+0.38\pm0.08$	$+0.45 \pm 0.53$	$+0.24\pm$	$+0.19 \pm 0.08$	$+1.21\pm0.18$
CDTG-16- <i>r</i> II	3	$-2.14 \pm 0.70$	$+0.39 \pm 0.19$	$+0.20\pm$	$-0.68\pm$	$-0.14 \pm 0.30$	$+0.26 \pm 0.32$	$+0.85 \pm 0.12$
CDTG-17-rII	3	$-1.28\pm0.03$	$+0.43 \pm 0.09$	•••	•••	$+0.18 \pm 0.15$	$+0.35 \pm 0.24$	$+0.72 \pm 0.01$
CDTG-18-rII	3	$-1.49 \pm 0.78$	$+0.31 \pm 0.05$	$+0.30\pm$	$+0.98\pm$	$+0.18\pm0.08$	$+0.37 \pm 0.14$	$+0.84 \pm 0.15$
CDTG-19-rII	3	$-0.93 \pm 0.09$	$+0.23\pm0.06$	•••		$+0.04 \pm 0.17$	$+0.45 \pm 0.20$	$+0.85 \pm 0.12$
CDTG-20-rII	3	$-3.20 \pm 0.29$	$+0.38\pm$	$+0.31 \pm 0.23$	$+0.69 \pm 0.13$	$+0.55 \pm 0.12$	$+1.10 \pm 0.09$	$+1.78\pm0.07$
Biweight (CDTG mean)		$-1.39 \pm 0.12$	$+0.40 \pm 0.03$	$+0.35 \pm 0.03$	$+0.49 \pm 0.08$	$+0.17 \pm 0.03$	$+0.45 \pm 0.03$	$+0.84 \pm 0.02$
Biweight (CDTG std)		$+0.37 \pm 0.06$	$+0.15 \pm 0.01$	$+0.16 \pm 0.03$	$+0.31 \pm 0.06$	$+0.15 \pm 0.02$	$+0.22 \pm 0.02$	$+0.11 \pm 0.02$
IQR (CDTG mean)		0.88	0.13	0.16	0.46	0.14	0.14	0.17
IQR (CDTG std)		0.31	0.07	0.09	0.26	0.07	0.10	0.11
Biweight (final) IQR (final)		$-1.27 \pm 0.68$ <b>1.08</b>	$+0.45 \pm 0.19$ <b>0.22</b>	$+0.37 \pm 0.20$ <b>0.24</b>	$+0.14 \pm 0.38$ <b>0.40</b>	$+0.10 \pm 0.21$ <b>0.28</b>	$+0.23 \pm 0.28$ <b>0.36</b>	$+0.55 \pm 0.16$ <b>0.21</b>

Note. The first section of the table lists the biweight location and scale of the abundances for each of the CDTGs. The second section of the table lists the mean and the standard error of the mean (using biweight estimates) for both the location and scale of the abundances of the CDTGs, along with the IQR of the abundances of the CDTGs. The third section of the table lists the biweight location and scale of the final sample for each of the abundances, along with the IQR for each of the abundances in the final sample. The IQR lines are bolded to draw attention to the CDTG elemental-abundance mean IQRs to compare to the final sample abundance IQRs. The IQR lines are bolded to draw attention to the CDTG elemental-abundance mean IQRs to compare to the final sample abundance IQRs.

(This table is available in machine-readable form.)

# **ORCID** iDs

#### References

Abbott, B. P., Abbott, R., Abbott, T. D., et al. 2017a, ApJL, 848, L12
Abbott, B. P., Abbott, R., Abbott, T. D., et al. 2017b, PhRvL, 119, 161101
Abohalima, A., & Frebel, A. 2018, ApJS, 238, 36
An, D., & Beers, T. C. 2020, ApJ, 897, 39
Anders, F., Khalatyan, A., Queiroz, A. B. A., et al. 2022, A&A, 658, A91
Aoki, W., Beers, T. C., Christlieb, N., et al. 2007, ApJ, 655, 492
Aoki, W., Beers, T. C., Lee, Y. S., et al. 2013, AJ, 145, 13
Aoki, W., Honda, S., Beers, T. C., et al. 2005, ApJ, 632, 611
Aoki, W., Matsuno, T., Honda, S., et al. 2017, PASJ, 69, 21
Asplund, M., Grevesse, N., Sauval, A. J., & Scott, P. 2009, ARA&A, 47, 481
Bailer-Jones, C. A. L., Rybizki, J., Fouesneau, M., Demleitner, M., & Andrae, R. 2021, AJ, 161, 147
Bandyopadhyay, A., Sivarani, T., & Beers, T. C. 2020, ApJ, 899, 22

```
Beers, T. C., Flynn, K., & Gebhardt, K. 1990, AJ, 100, 32
Behara, N. T., Bonifacio, P., Ludwig, H.-G., et al. 2010, A&A, 513, A72
Belokurov, V., Erkal, D., Evans, N. W., Koposov, S. E., & Deason, A. J. 2018,
     NRAS, 478, 611
Belokurov, V., Sanders, J. L, Fattahi, A., et al. 2020, MNRAS, 494, 3880
Binney, J., & Tremaine, S. 2008, Galactic Dynamics (2nd ed.; Princeton, NJ:
  Princeton Univ. Press)
Borsato, N. W, Martell, S. L, & Simpson, J. D. 2020, MNRAS, 492, 1370
Buder, S., Sharma, S., Kos, J., et al. 2021, MNRAS, 506, 150
Burbidge, E. M., Burbidge, G. R., Fowler, W. A., & Hoyle, F. 1957, RvMP,
Burris, D. L., Pilachowski, C. A., Armandroff, T. E., et al. 2000, ApJ, 544, 302
Cain, M., Frebel, A., Gull, M., et al. 2018, ApJ, 864, 43
Cain, M., Frebel, A., Ji, A. P., et al. 2020, ApJ, 898, 40
Callingham, T. M, Cautun, M., Deason, A. J., et al. 2022, MNRAS, 513, 4107
Cameron, A. G. W. 1957, PASP, 69, 201
Campello, R. J. G. B., Moulavi, D., & Sander, J. 2013, in Advances in
   Knowledge Discovery and Data Mining, ed. J. Pei et al. (Berlin:
   Springer), 160
Carollo, D., Chiba, M., Ishigaki, M., et al. 2019, ApJ, 887, 22
Casey, A. R., Keller, S. C., Da Costa, G., Frebel, A., & Maunder, E. 2014, ApJ,
Chiba, M., & Beers, T. C. 2000, AJ, 119, 2843
Chiba, M., & Yoshii, Y. 1998, AJ, 115, 168
Christlieb, N., Beers, T. C., Barklem, P. S., et al. 2004, A&A, 428, 1027
Cohen, J. G., Christlieb, N., McWilliam, A., et al. 2004, ApJ, 612, 1107
Cordoni, G., Da Costa, G. S., Yong, D., et al. 2021, MNRAS, 503, 2539
Cowan, J. J., Sneden, C., Lawler, J. E., et al. 2021, RvMP, 93, 015002
Di Matteo, P., Haywood, M., Lehnert, M. D., et al. 2019, A&A, 632, A4
Dietz, S. E., Yoon, J., Beers, T. C., Placco, V. M., & Sun Lee, Y. 2021, ApJ,
  914, 100
```

Barklem, P. S., Christlieb, N., Beers, T. C., et al. 2005, A&A, 439, 129

```
Drout, M. R., Piro, A. L., Shappee, B. J., et al. 2017, Sci, 358, 1570
Ezzeddine, R., Rasmussen, K., Frebel, A., et al. 2020, ApJ, 898, 150
For, B.-Q., & Sneden, C. 2010, AJ, 140, 1694
Francois, P., Depagne, E., Hill, V., et al. 2007, A&A, 476, 935
Fulbright, J. P. 2000, AJ, 120, 1841
Gaia Collaboration, Brown, A. G. A., Vallenari, A., Prusti, T., et al. 2021,
       A, 649, A1
Gaia Collaboration, Prusti, T., de Bruijne, J. H. J., et al. 2016, A&A, 595, A1
GRAVITY Collaboration, Abuter, R., Amorim, A., et al. 2020, A&A, 636, L5
Gudin, D., Shank, D., Beers, T. C., et al. 2021, ApJ, 908, 79
Hanke, M., Hansen, C. J., Ludwig, H.-G., et al. 2020, A&A, 635, A104
Hansen, C. J., Primas, F., Hartman, H., et al. 2012, A&A, 545, A31
Hansen, T. T., Andersen, J., Nordstrom, B., et al. 2015, A&A, 583, A49
Hansen, T. T., Holmbeck, E. M., Beers, T. C., et al. 2018, ApJ, 858, 92
Hasselquist, S., Hayes, C. R., Lian, J., et al. 2021, ApJ, 923, 172
Hattori, K., Okuno, A., & Roederer, I. U. 2022, arXiv:2207.04110
Hawkins, Keith, & Wyse, R. F. G. 2018, MNRAS, 481, 1028
Hayek, W., Wiesendahl, U., Christlieb, N., et al. 2009, A&A, 504, 511
Hayes, C. R., Majewski, S. R., Shetrone, M., et al. 2018, ApJ, 852, 49
Helmi, A. 2020, ARA&A, 58, 205
Helmi, A., Babusiaux, C., Koppelman, H. H., et al. 2018, Natur, 563, 85
Helmi, A., & de Zeeuw, P. T. 2000, MNRAS, 319, 657
Helmi, A., Veljanoski, J., Breddels, M. A., Tian, H., & Sales, L. V. 2017,
    &A, 598, A58
Helmi, A., & White, S. D. M. 1999, MNRAS, 307, 495
Hill, V., Christlieb, N., Beers, T. C., et al. 2017, A&A, 607, A91
Hirai, Y., Beers, T. C., Chiba, M., et al. 2022, MNRAS, 517, 4856
Hollek, J. K., Frebel, A., Roederer, I. U., et al. 2011, ApJ, 742, 54
Holmbeck, E. M., Beers, T. C., Roederer, I. U., et al. 2018, ApJL, 859, L24
Holmbeck, E. M., Hansen, T. T., Beers, T. C., et al. 2020, ApJS, 249, 30
Honda, S., Aoki, W., Kajino, T., et al. 2004, ApJ, 607, 474
Howes, L. M., Asplund, M., Keller, S. C., et al. 2016, MNRAS, 460, 884
Howes, L. M., Casey, A. R., Asplund, M., et al. 2015, Natur, 527, 484
Huang, Y., Yuan, H., Beers, T. C., & Zhang, H. 2021, ApJL, 910, L5
Ishigaki, M. N., Aoki, W., & Chiba, M. 2013, ApJ, 771, 67
Ivans, I. I., Simmerer, J., Sneden, C., et al. 2006, ApJ, 645, 613
Jacobson, H. R., Keller, S., Frebel, A., et al. 2015, ApJ, 807, 171
Jain, R., Prugniel, P., Martins, L., & Lançon, A. 2020, A&A, 635, A161
Ji, A. P., Frebel, A., Simon, J. D., & Chiti, A. 2016, ApJ, 830, 93
Johnson, J. A. 2002, ApJS, 139, 219
Kielty, C. L, Venn, K. A, Sestito, F., et al. 2021, MNRAS, 506, 1438
Kobayashi, C., Umeda, H., Nomoto, K., Tominaga, N., & Ohkubo, T. 2006,
   ApJ, 653, 1145
Koppelman, H., Helmi, A., & Veljanoski, J. 2018, ApJL, 860, L11
Koppelman, H. H., Helmi, A., Massari, D., Price-Whelan, A. M., &
   Starkenburg, T. K. 2019a, A&A, 631, L9
Koppelman, H. H., Helmi, A., Massari, D., Roelenga, S., & Bastian, U. 2019b,
     &A, 625, A5
Kordopatis, G., Recio-Blanco, A., Schultheis, M., & Hill, V. 2020, A&A, 643, A69
Lai, D. K., Bolte, M., Johnson, J. A., et al. 2008, ApJ, 681, 1524
Lattimer, J. M., & Schramm, D. N. 1974, ApJL, 192, L145
Li, H., Du, C., Liu, S., Donlon, T., & Newberg, H. J. 2019, ApJ, 874, 74
Li, H., Du, C., Yang, Y., et al. 2020, ApJ, 895, 23
Li, H., Hammer, F., Babusiaux, C., et al. 2021, ApJ, 916, 8
Limberg, G., Rossi, S., Beers, T. C., et al. 2021b, ApJ, 907, 10
Limberg, G., Santucci, R. M., Rossi, S., et al. 2021a, ApJ, 913, 11
Limberg, G., Souza, S. O., Pérez-Villegas, A., et al. 2022, ApJ, 935, 109
Lövdal, S. S., Ruiz-Lara, T., Koppelman, H. H., et al. 2022, A&A, 665, A57
Mackereth, J. T., Schiavon, R. P, Pfeffer, J., et al. 2019, MNRAS, 482, 3426
Malhan, K., Ibata, R. A., Sharma, S., et al. 2022, ApJ, 926, 107
Mardini, M. K., Placco, V. M., Meiron, Y., et al. 2020, ApJ, 903, 88
Mardini, M. K., Placco, V. M., Taani, A., Li, H., & Zhao, G. 2019, ApJ,
  882, 27
Massari, D., Koppelman, H. H., & Helmi, A. 2019, A&A, 630, L4
Masseron, T., Johnson, J. A., Lucatello, S., et al. 2012, ApJ, 751, 14
Matsuno, T., Hirai, Y., Tarumi, Y., et al. 2021, A&A, 650, A110
McConnachie, A. W., & Venn, K. A. 2020, RNAAS, 4, 229
McMillan, P. J. 2017, MNRAS, 465, 76
McMillan, P. J., & Binney, J. J. 2008, MNRAS, 390, 429
McWilliam, A., Preston, G. W., Sneden, C., & Searle, L. 1995a, AJ, 109, 2757
McWilliam, A., Preston, G. W., Sneden, C., & Shectman, S. 1995b, AJ,
   109, 2736
```

```
Monty, S., Venn, K. A, Lane, J. M. M., Lokhorst, D., & Yong, D. 2020,
  MNRAS, 497, 1236
Mosta, P., Roberts, L. F., Halevi, G., et al. 2018, ApJ, 864, 171
Myeong, G. C., Evans, N. W., Belokurov, V., Amorisco, N. C., &
  Koposov, S. E. 2018a, MNRAS, 475, 1537
Myeong, G. C., Evans, N. W., Belokurov, V., Koposov, S. E., & Sanders, J. L.
  2017, MNRAS, 469, L78
Myeong, G. C., Evans, N. W., Belokurov, V., Sanders, J. L., & Koposov, S. E.
  2018b, MNRAS, 478, 5449
Myeong, G. C., Evans, N. W., Belokurov, V., Sanders, J. L., & Koposov, S. E.
  2018c, ApJL, 856, L26
Naidu, R. P., Conroy, C., Bonaca, A., et al. 2020, ApJ, 901, 48
Naidu, R. P., Conroy, C., Bonaca, A., et al. 2021, ApJ, 923, 92
Naidu, R. P., Ji, A. P., Conroy, C., et al. 2022, ApJL, 926, L36
Nishimura, N., Takiwaki, T., & Thielemann, F.-K. 2015, ApJ, 810, 109
Placco, V. M., Frebel, A., Beers, T. C., et al. 2014a, ApJ, 781, 40
Placco, V. M., Frebel, A., Beers, T. C., & Stancliffe, R. J. 2014b, ApJ, 797, 21
Placco, V. M., Holmbeck, E. M., Frebel, A., et al. 2017, ApJ, 844, 18
Placco, V. M., Santucci, R. M., Beers, T. C., et al. 2019, ApJ, 870, 122
Placco, V. M., Santucci, R. M., Yuan, Z., et al. 2020, ApJ, 897, 78
Preston, G. W., Sneden, C., Thompson, I. B., Shectman, S. A., & Burley, G. S.
  2006, AJ, 132, 85
Rasmussen, K. C., Zepeda, J., Beers, T. C., et al. 2020, ApJ, 905, 20
Reid, M. J., & Brunthaler, A. 2020, ApJ, 892, 39
Riello, M., De Angeli, F., Evans, D. W., et al. 2021, A&A, 649, A3
Roederer, I. U., Cowan, J.J., Preston, G. W., et al. 2014, MNRAS, 445, 2970
Roederer, I. U., Hattori, K., & Valluri, M. 2018, AJ, 156, 179
Roederer, I. U., & Lawler, J. E. 2012, ApJ, 750, 76
Roederer, I. U., Lawler, J. E., Den Hartog, E. A., et al. 2022, ApJS, 260, 27
Roederer, I. U., Lawler, J. E., Sobeck, J. S., et al. 2012, ApJS, 203, 27
Roederer, I. U., Sneden, C., Thompson, I. B., Preston, G. W., &
Shectman, S. A. 2010, ApJ, 711, 573
Ryan, S. G., Norris, J. E., & Beers, T. C. 1996, ApJ, 471, 254
Ryu, J., & Lee, M. G. 2018, ApJL, 863, L38
Sakari, C. M., Placco, V. M., Farrell, E. M., et al. 2018, ApJ, 868, 110
Sakari, C. M., Roederer, I. U., Placco, V. M., et al. 2019, ApJ, 874, 148
Schlafly, E. F., & Finkbeiner, D. P. 2011, ApJ, 737, 103
Schlaufman, K. C., & Casey, A. R. 2014, ApJ, 797, 13
Schlegel, D. J., Finkbeiner, D. P., & Davis, M. 1998, ApJ, 500, 525
Schönrich, R., Binney, J., & Dehnen, W. 2010, MNRAS, 403, 1829
Sestito, F., Longeard, N., Martin, N. F, et al. 2019, MNRAS, 484, 2166
Shank, D., Beers, T. C., Placco, V. M., et al. 2022b, ApJ, 926, 26
Shank, D., Komater, D., Beers, T. C., Placco, V. M., & Huang, Y. 2022a, ApJS,
Shappee, B. J., Simon, J. D., Drout, M. R., et al. 2017, Sci, 358, 1574
Siqueira Mello, C., Hill, V., Barbuy, B., et al. 2014, A&A, 565, A93
Sneden, C., Preston, G. W., McWilliam, A., & Searle, L. 1994, ApJL, 431,
Tanaka, M., Utsumi, Y., Mazzali, P. A., et al. 2017, PASJ, 69, 102
Thielemann, F.-K., Eichler, M., Panov, I. V., & Wehmeyer, B. 2017, ARNPS,
Truran, J. W., & Cameron, A. G. W. 1971, Ap&SS, 14, 179
Truran, J. W., Cowan, J. J., Pilachowski, C. A., & Sneden, C. 2002, PASP,
   114, 1293
Valentini, M., Chiappini, C., Bossini, D., et al. 2019, A&A, 627, A173
Vasiliev, E. 2019, MNRAS, 482, 1525
Vasiliev, E., & Baumgardt, H. 2021, MNRAS, 505, 5978
Wanajo, S., Sekiguchi, Y., Nishimura, N., et al. 2014, ApJL, 789, L39
Watson, D., Hansen, C. J., Selsing, J., et al. 2019, Natur, 574, 497
Winteler, C., Kappeli, R., Perego, A., et al. 2012, ApJL, 750, L22
Woody, T., & Schlaufman, K. C. 2021, AJ, 162, 42
Woosley, S. E., & Weaver, Thomas A. 1995, ApJS, 101, 181
Woosley, S. E., Wilson, J. R., Mathews, G. J., Hoffman, R. D., & Meyer, B. S.
  1994, ApJ, 433, 229
Xing, Q.-F., Zhao, G., Aoki, W., et al. 2019, NatAs, 3, 631
Yong, D., Da Costa, G. S., Bessell, M. S., et al. 2021a, MNRAS, 507, 4102
Yong, D., Kobayashi, C., Da Costa, G. S., et al. 2021b, Natur, 595, 223
Yoon, J., Beers, T. C., Placco, V. M., et al. 2016, ApJ, 833, 20
Yuan, Z., Chang, J., Beers, T. C., & Huang, Y. 2020a, ApJL, 898, L37
Yuan, Z., Myeong, G. C., Beers, T. C., et al. 2020b, ApJ, 891, 39
Yuan, Z., Smith, M. C., Xue, X.-X., et al. 2019, ApJ, 881, 164
Zepeda, J., Rasmussen, K. C., Beers, T. C., et al. 2022, ApJ, 927, 13
```